Design of optical characteristics of ceria nanoparticles for applications including gas sensing and up-conversion

Nader Shehata

Dissertation Submitted to the Faculty of the
Virginia Polytechnic Institute and State University
in partial fulfillment of the requirements for the degree of
Doctor of Philosophy
In
Electrical Engineering

Kathleen Meehan (Chairman)
Jean Heremans
Mantu Hudait
Marius Orlowski
Yong Xu
Mohamed Elosairy

November 9, 2012
Blacksburg, Virginia

Keywords: Ceria nanoparticles, lanthanide dopants, oxygen vacancies, fluorescence quenching, oxygen sensing, up-conversion.

Design of optical characteristics of ceria nanoparticles for applications that include gas sensing and up-conversion

Nader Shehata

ABSTRACT

This thesis investigates the impact of doping on the optical and structural characteristics of cerium oxide (ceria) nanoparticles synthesized using chemical precipitation. The dopants selected are samarium and neodymium, which have positive association energy with oxygen vacancies in the ceria host, and negative association lanthanides, holmium and erbium, as well as two metal dopants, aluminum and iron. Characteristics measured are absorption and fluorescence spectra and the diameter and lattice parameter of ceria. Analysis of the characteristics indicates qualitatively that the dopant controls the O-vacancy concentration and the ratio of the two cerium ionization states: Ce^{+3} and Ce^{+4}. A novel conclusion is proposed that the negative association lanthanide dopants can act as O-vacancies scavengers in ceria while the O-vacancy concentration increases in ceria doped with positive association lanthanide elements. Doped ceria nanoparticles are evaluated in two applications: dissolved oxygen (DO) sensing and up-conversion. In the first application, ceria doped with either Sm or Nd and ceria doped with aluminum have a strong correlation between the fluorescence quenching with the DO concentration in the aqueous solution in which the ceria nanoparticles are suspended. Stern-Volmer constants (K_{SV}) of doped ceria are found to strongly depend upon the O-vacancy concentration and are larger than some of the fluorescent molecular probes currently used to measure DO. The K_{SV} measured between 25-50^{o}C is found to be significantly less temperature dependent as compared to the constants of commercially-available DO molecular probes. In the second application, up-conversion, ceria nanoparticles doped with erbium and an additional lanthanide, either Sm or Nd, are exposed to IR radiation at 780 nm. Visible emission is only observed after the nanoparticles are calcinated at high temperature, greatly diminishing the concentration of O-vacancies. It is concluded that O-vacancies do not play a dominant role in up-conversion, unlike that drawn for down-conversion, where the fluorescence intensity is strongly correlated with the O-vacancy concentration. Correlations between annealing temperatures, dopant, and dopant concentrations with the power dependence of up-conversion on the pump and the origin of the intensities of the visible emission are presented. These studies show the promise of doped ceria nanoparticles.

Acknowledgements

My thanks are wholly devoted to our Lord; Allah, who has helped me all the way to complete this work successfully. I owe a depth of gratitude to my family; mother, father, my wife, and my daughter, for support and encouragement all the time. They always stand beside me until I have completed this work.

I am honored that my work has been supervised by **Prof. Kathleen Meehan.** I wish to express my sincere thanks to her for giving me her time and effort for guidance, support and advice throughout this work. Also, her valuable support in writing papers, patents, and proposals are highly appreciated. Furthermore I would like to thank the other members of my committee: **Prof. Marius Orlowski**, **Prof. Yong Xu**, **Prof. Mantu Hudait**, and **Prof. Jean Heremans** for their support both on my committee and as my professors in the various classes I have taken with them. I can't forget to thank my Egyptian member in the committee; **Prof. Mohamed Elosairy**, for his support and advice. Also, I appreciate the fruitful support from **Mr. Donald Leber**; the manager of Micron lab in Electrical and Computer Engineering Department (ECE).

I would like to thank the support of VT-MENA program; especially I am expressing my gratitude to **Prof. Sedki Riad**, **Prof. Yasser Hanafy**, **Prof. Mohamed Rizk**, and **Dr. Mustafa Elneinaay**. My special thank is to **Prof. Ioannis Besieris** for his support and advices.

Finally, I would like to express my thanks to all the staff in the department of Engineering Mathematics and Physics in Faculty of Engineering, Alexandria University. Special thanks to **Prof. Ali Okaz**, **Dr. Yahya Mounir**, **Dr. Samir Ghanem**, and my best friends; **Ishak Kandas** and **Islam Ashry**. Also, I am very grateful to the support of my close friend; **Ibrahim Hassounah**, who is working as postdoctoral researcher in Institute for Critical Technology and Applied Science (ICTAS) in Virginia Tech.

This Dissertation is dedicated
to the great Egyptian youth
who were martyred during the Egyptian revolution of Jan. 25th

Table of Contents

Abstract…….…….. ii

Acknowledgements…….……...iii

Table of Contents ……..…….……v

Tables and Figures …..……..……...……...viii

Chapter 1: Introduction …….....……1

1.1 Importance of ceria nanoparticles ...……..1

1.2 Doped ceria nanoparticles: Defects and synthesis ...…….……..…..2

1.3 Motivation of the thesis …...…….3

1.4 Brief description of the work's procedure……6

1.5 Thesis structure……....10

Chapter 2: Theoretical Background: Doped Ceria Nanoparticles…….14

2.1 The structure and defects of undoped and doped ceria……14

2.2 Optical characteristics of ceria…….16

2.2.1 Absorption coefficient and direct bandgap calculations……...16

2.2.2 Theory of fluorescence ……19

2.3 Structural Characteristics of ceria……...….22

2.4 XPS analysis……23

Chapter 3: Synthesis and Characterization: Experimental Processes…….…...25

3.1 Experimental procedure of the synthesis process……....25

3.1.1 Synthesis of undoped and single doped ceria nanoparticles…….……25

3.1.2 Synthesis of mixed doped ceria ……...27

3.2 Experimental procedure of optical and structure characterization …….28

3.2.1 Experimental facilities for measuring the optical characteristics…….28

3.2.2 Measurement facilities for Structural properties…….……..29

Chapter 4: Optical and Structural Characterization: Results & Discussions……..31

4.1 Characterization of undoped ceria nanoparticles…….……31

4.1.1 Absorbance dispersion and optical direct bandgap……...31
4.1.2 PL intensity and fluorescence emission……32
4.1.3. TEM and XRD analysis……..34
4.2 Characterization of single lanthanide doped ceria……...34
4.2.1 Absorbance dispersion and direct allowed bandgap…….34
4.2.2 Fluorescence emission intensities…….36
4.2.3 Results of the structural parameters……..38
4.2.4 XPS analysis…….41
4.3 Mixed doped ceria (MDC) characterization……42
4.3.1 Absorbance dispersion and bandgap study……..42
4.3.2 Fluorescence emissions spectra ……...44
4.3.3 Results of structural analysis……....45
4.4 Doping ceria with some tri-valent metals…..……...48
4.4.1 Absorbance dispersion and direct allowed bandgap…….48
4.4.2 Fluorescence emissions results…….49
4.4.3 Analysis of structural parameters……..50
Chapter 5: Ceria Nanoparticles as Optical DO Sensing Material…..……52
5.1 Theory of DO sensing based on fluorescence quenching……52
5.2 Fluorescence quenching experimental setup……...54
5.3 Fluorescence quenching and K_{SV} results……..…56
5.3.1 Fluorescence quenching at room temperature……..….56
5.3.2 Thermal stability of K_{SV}……60
Chapter 6: Doped Ceria Nanoparticles as Up-conversion Media…….……65
6.1 Theory of up-conversion……65
6.2 Experimental procedure to measure up-converted emissions……70
6.3 Experimental results of up-conversion……70
6.3.1 Absorbance spectrum of ceria: Er…….70

6.3.2 Effect of calcination temperature and Er doping ratio……..…71
6.3.3 Power dependence……74
6.3.4 UC emission for ceria:Er with additional lanathanide dopants……75
6.4 Suggested up-conversion mechanisms……78
Chapter 7: Conclusions & Future Work……81
7.1 Summary of research contributions……..81
7.2 Suggested future work……..86
References…..……89

Tables and Figures

Tables

Table 3.1: Doping weight ratios of the initial precursors for single doped ceria……...27

Table 3.2: Doping weight ratios of the initial precursors in MDC nanoparticles……..27

Table 4.1: Optical and structural data of the whole ceria samples, pure and doped with rare earth elements ……40

Table 4.2: Chemical analysis of the atomic concentrations of synthesized nanoparticles ……...42

Table 4.3: The complete measured data for MDC nanoparticles……..……47

Table 4.4: The complete data measured for doped ceria within Al and Fe……..…….51

Table 5.1: Stern-Volmer constants of undoped and doped ceria nanoparticles…….....59

Table 5.2: K_{SV} values for undoped and doped ceria nanoparticles at different temperatures……62

Figures

Fig. 1.1: Flowchart of the thesis' work plan…….……..…9

Fig. 2.1: Crystalline structure of CeO_2 a) without defects, b) with intrinsic defects .....……14

Fig. 2.2: Band tails due to impurities (C.B: Conduction band, V.B: Valence band, E_g: Bandgap, E_g': Reduced bandgap, and DOS: Density of states) …...…….18

Fig. 2.3: Energy band for CeO_2, where cerium is in the Ce^{+4} state, and the trap level associated with cerium is in the Ce^{+3} state……..19

Fig. 2.4: Schematic diagrams of (a) absorption process and (b) excitation process ……...…..20

Fig. 2.5: Jablonski diagram showing processes involved in fluorescence, where "Abs." is the absorbed photon, "Fluo." is the fluorescence emission, "Phosph." is the phosphorescence emission, "S" is a singlet state, "S_0" is the ground state, T is a triplet state with long lifetime, IC is the internal conversion for excited vibrational states when the absorbed photon has more energy than the radiated photon, and ISC is the intersystem crossing……...21

Fig. 3.1: Flowchart of the synthesis procedure for undoped and doped ceria nanoparticles…….26

Fig. 3.2: Schematic diagram of the fluorescence spectroscopy setup……...…….29

Fig. 4.1: a) Absorbance dispersion and b) $(\alpha E)^2$ versus E used to determine direct allowed bandgap energy of undoped ceria nanoparticles……31

Fig. 4.2: PL intensity of undoped ceria, under 370 nm excitation…….32

Fig. 4.3: Fluorescence emission of undoped ceria nanoparticles under 430 nm excitation…..…33

Fig. 4.4: Structural characterizations of ceria nanoparticles a) TEM image with diffraction rings and b) XRD pattern…….……...……34

Fig. 4.5: Absorbance dispersion of doped ceria with (a) Nd and (b) Er, at different reagent weight ratios……...35

Fig. 4.6: Direct bandgap calculation of doped ceria with (a) Sm and (b) Ho, at different reagent weight ratios "dotted line is the bandgap of undoped ceria" …….……...36

Fig. 4.7: Emitted fluorescent intensity of doped ceria with a) Nd and b) Er "dotted line is the fluorescence peak of undoped ceria"…….....37

Fig. 4.8: TEM images and diffraction rings of ceria doped with 5% reagent weight of a) Ho, b) Er, c) Nd, and d) Sm……..39

Fig. 4.9: XRD patterns of ceria doped with 5% reagent weight of a) Sm and b) Nd…...…….39

Fig. 4.10: Photos of the wet powder for undoped ceria a) before, and b) after the process of XRD measurement……..41

Fig. 4.11: Absorbance dispersion of ceria, doped with a) Ho and Nd and b) Sm and Er…...…...43

Fig. 4.12: Direct allowed bandgap calculations of ceria, doped with a) Ho and Nd and b) Sm and Er……...43

Fig. 4.13: Fluorescence emission of ceria, doped with a) Er and Nd and b) Ho and Sm…….....45

Fig. 4.14: TEM images of ceria nanoparticles doped with equal concentrations of a) Nd and Er and b) Sm and Ho……..46

Fig. 4.15: XRD pattern of some ceria nanoparticles doped with equal concentrations of a) Nd and Ho, and b) Sm and Er……46

Fig. 4.16: Absorbance dispersion of ceria doped with a) Al and b) Fe……...…..…48

Fig. 4.17: Direct allowed bandgap calculations of ceria doped with a) Al and b) Fe "dotted line is the bandgap of undoped ceria"…….....…….49

Fig. 4.18: Fluorescence emission of ceria doped with a) Al and b) Fe "dotted line is the fluorescence peak of undoped ceria" ……..……...…….…..49

Fig. 4.19: TEM images of ceria nanoparticles doped with 5% reagent weight of a) Al and b) Fe ……...50

Fig. 4.20: XRD pattern of ceria doped with 5% reagent weight of a) Al and b) Fe……..…...50

Fig. 5.1: Schematic Diagram of the fluorescence quenching DO sensing setup……..……56

Fig. 5.2: A photo of the optical fluorescence quenching DO sensing setup……..……..…....56

Fig. 5.3: Fluorescence quenching spectra at room temperature with different DO concentrations for a) undoped ceria and b) doped ceria with 5% reagent weight of Sm as an example……...57

Fig. 5.4: Stern-Volmer relations at room temperature for ceria doped with 5% reagent weight ratio of a) Nd and b) Al……58

Fig. 5.5: Fluorescence spectra, demonstrating fluorescence quenching, at a constant dissolved oxygen concentration, DO = 10.3 mg/L, for ceria doped with a) Sm, and b) Nd at 25, 30, 40, and 50^{o}C……...…61

Fig. 5.6: The linear relationship between I_o/I versus DO concentration at 25, 30, 40, and 50^{o}C, for doped ceria with a) Sm and b) Al...……...……...61

Fig. 6.1: 4f free-ion degeneracy of the lanthanides……...…….....67

Fig. 6.2: Dieke diagram: energy levels of the $^{2S+1}L_J$ of some trivalent lanthanide ions...……..68

Fig. 6.3: Schematic diagrams of a) ESA and b) ET processes ($h\upsilon$ is the photon energy)…….69

Fig. 6.4: Absorbance spectrum of ceria:Er synthesized with a doping reagent weight ratio of 5% with a) no calcination and b) calcinated at 900^{o}C ……...……...…71

Fig. 6.5: Up-conversion emission of ceria: Er, 5% reagent weight ratio, at different calcinations temperatures…….…..72

Fig. 6.6: a) Absorbance dispersion and b) direct bandgap calculation of ceria: Er nanoparticles, with a 5% reagent weight ratio and calcinated at 900^{o}C……...73

Fig. 6.7: Up-conversion emission of ceria: Er, within 900^{o}C calcination, at different erbium reagent weight ratios……..74

Fig. 6.8: Up-conversion power dependence on the input power of the 780 nm pump source for ceria: Er 5% reagent weight ratio calcinated at 900^{o}C for a) green (~ 555 nm) and b) red (~ 680 nm) emission wavelengths…….75

Fig. 6.9: Up-conversion emission of 900^{o}C calcinated ceria: Er nanoparticles of 5% reagent weight of erbium with i) no added Nd, ii) added 5% reagent weight of Nd and iii) added 10% reagent weight of Nd (The insets show the slight improvement of red emissions within adding 5% reagent weight ratio of Nd)…….…… 76

Fig. 6.10: Up-conversion emission of 900^{o}C calcinated ceria: Er nanoparticles of 5% reagent weight of erbium with i) no added Sm, ii) added 5% reagent weight of Sm and iii) added 10% reagent weight of Sm……..…76

Fig. 6.11: Up-conversion mechanisms with suggested pathways for ceria: Er nanoparticles where the heavy black lines show the excitation of Er, the green and red lines are the transitions from the excited to ground state that produce green and red emission, respectively, and NR means that the transition is non-radiative……..…..…..79

Fig. 6.12: Up-conversion mechanisms with suggested pathways for ceria: Er nanoparticles doped with neodymium or samarium, where ET indicates an energy transfer mechanism and NR indicates a non-radiative transition…….……...80

CHAPTER ONE

Introduction

1.1 Importance of ceria nanoparticles

Various nanomaterials made from silver, gold, titanium oxide, zirconium oxide, vanadium oxide, cadmium selenide, and carbon-based nanoparticles have been widely used for industrial purposes [1]. However, cerium oxide (ceria) nanoparticles can be considered one of the most important nanomaterials with wide ranges of applications in solar cells, fuel cells, gas sensors, oxygen pumps, and glass ceramics [2]. In last few years, ceria nanoparticles, as well as other oxides with the cubic fluorite structure, have been extensively studied because of its high oxygen storage capabilities and the large diffusivity of oxygen vacancies [3]. Doping ceria nanoparticles with some tri-valent elements is a promising technique to improve the ionic conductivity of ceria [4].

In biomedical engineering, several studies have reported the ability of ceria nanoparticles to mitigate oxidative stresses and reactive oxygen species (ROS) at the biological level [5-6]. This material can act as a scavenger for excess free radicals such as superoxide (O_2^-) and hydroxyl radical ($OH^\bullet$), which are responsible for damaging the molecular structures in biological organisms and stripping electrons from cellular macromolecules [7]. In electronics, ceria has been used in applications that realizes on the fact that ceria is a wide bandgap material, which include UV absorbents [8], polishing media in microelectronics [9], and thin-film high-K gate dielectric [10]. Ceria, as nanoparticles or in the form of a thin film, is a common catalyst in the fuel cell technology [11]. In the communications field, ceria and cerium-based materials have been used to enhance the emission efficiency of Er-doped fibers and glass ceramics [12-13] due to phenomena such as resonance energy transfer. As the ionic conductivity of ceria is determined

by mobility and concentration of oxygen (O) vacancies, it can be used for oxygen sensing based on resistive techniques [14].

1.2 Doped ceria nanoparticles: Defects and synthesis

In undoped ceria, some changes in the structural properties, such as a decrease in the lattice parameter, are reported due to thermal disorders. This is caused by increasing the conversion process of Ce^{+4} ions to Ce^{+3} ions due to the increase of the formation rate of oxygen vacancies [15]. Generally, doping ceria with tri-valent atoms is reported to increase the concentration of O-vacancies [16-17]. However, this is not universally the case as scandium (Sc^{+3}) when used as a dopant in ceria acts as a scavenger for vacancies. The ability of Sc^{+3} to decrease the O-vacancy concentration is due to the negative association energy between the O vacancy and dopant ion [18], which provides evidence that perhaps not all trivalent doped elements increase the formation of oxygen vacancies in ceria.

Related to ceria synthesis processes, many methods have been used to produce pure and doped ceria nanoparticles such as chemical precipitation [19], hydro-thermal synthesis [20], and solid-state reaction method [21]. Compared to other methods, chemical precipitation, which is selected for this work, is more attractive due to the cheap salt precursors, simple operation, and ease of mass production [22]. The synthesis process and the techniques used to dope the nanoparticles are described in Chapter 3.

1.3 Motivation of the thesis

This research work studies the impact of the selection of tri-valent dopants on some of the optical and structural characteristics in ceria nanoparticles. As it is hypothesized that the association energy of the tri-valent dopant will determine the relative concentration of O-vacancies as compared to undoped ceria and that the O-vacancy concentration determines many of the characteristics of the ceria nanoparticles that are critical for many applications. The results of the studies on these characteristics, described in Chapter 4, are correlated to the concentration of oxygen vacancies defects formed in undoped and doped ceria nanoparticles to understand the observed changes to ceria nanoparticles as a result to the dopant atom and its concentration in the nanoparticles.

The impact of doping on the structural characteristics and its correlation to defects in the material has been recently studied, though not in great depth, in other previous research studies on doped ceria nanoparticles [17-22], studies on the relationship between dopant atom and concentration on the optical properties of ceria are lacking. This is one of the first studies to explore the use of dopants to improve the optical properties of ceria nanoparticles to obtain enhanced performance in applications such as solid state lighting, solar cells, and other systems that employ up- and down-conversion, energy transfer, and optical mixing processes. The optical characteristics studied are absorbance dispersion, direct allowed bandgap, and fluorescence emission. The structural characteristics measured during this research study are particle mean size, lattice parameter, inter-planar distance, and crystalline structure. The measured optical and structural characteristics are correlated to the O-vacancies defects formed in undoped and doped ceria. From this work, we have arrived at a novel conclusion on techniques to control these

defects in ceria and, as a result, several crucial material properties through the doping technique are summarized in Chapter 4.

Here, there is an important point to be mentioned. This work introduces the correlation between the optical and structural characteristics with the Ce^{+4}/Ce^{+3} conversion which is associated with the formation of O-vacancies. There are some reported techniques to inspect the O-vacancies formation associated to the incremental conversion rate from Ce^{+4} ionization states to Ce^{+3} states, such as X-ray photoelectron spectroscopy (XPS) and Raman spectroscopy [23-24]. However, both techniques have significant drawbacks. In XPS, there is some ambiguity over the accuracy of the calculated ionization state of cerium because of an increase in the O-vacancy concentration observed under vacuum. Hence, this technique is supposed not used to quantify the concentration of Ce^{+4} and Ce^{+3} in the nanoparticle samples [25]. Raman scattering is highly sensitive to laser instabilities, needs high resolution detection, and subject to saturation at the higher laser power density levels [26]. The experimental verifications used in this work to prove the increase or decrease of O-vacancies in ceria due to the selected lanthanide dopants compared to undoped ceria are the direct allowed bandgap, the amplitude of the fluorescence signal, grain size or average diameter, and lattice parameter. In our work, XPS is only used to analyze the chemical composition of the synthesized doped ceria nanoparticles to verify the molar fractions of the dopants. Raman spectroscopy was not performed as the measurements have to be performed on dry or slightly damp powders composed of the nanoparticles. In previous studies carried out in our lab, it was found that the Raman spectrum of the damp nanoparticles started to change after five minutes of exposure to air. The optical characterization techniques chosen for this work can be performed on colloidal nanoparticle suspensions – the same environment as is used during the studies on applications of the nanoparticles.

After the completion of the nanoparticle characterization stage of our research, doped ceria nanoparticles are used in two applications, which are sensing dissolved oxygen (DO) (Chapter 5) and up-conversion of near-infrared (NIR) light (Chapter 6), to demonstrate the value of doping technique in ceria and the correlation via defect engineering. In the first application, select ceria samples doped with samarium (Sm), neodymium (Nd) and aluminum (Al) are used as the molecular probe in a fluorescence quenching dissolved oxygen (DO) nanosensors. To our knowledge, this application of ceria nanoparticles as the optical sensing active material in such a sensor is novel. This optical sensor can open new windows of study on ceria nanoparticles as a multi-function material. For example, we expect that this nanomaterial can be used as bio-imaging material, free radical scavenger, and DO sensor in the same time.

In the second application presented in this work, doped ceria nanoparticles are used as up-conversion media to obtain visible emission from NIR excitation. The amplitude of the visible emission obtained from ceria nanoparticles containing various combinations and compositions of dopant atoms are correlated with the concentrations of the dopant atoms and energy levels as synthesized and as a function of the calcinated temperatures during post-growth thermal anneals. The impact of the O- vacancy concentration on this phenomenon is checked in terms of the molecular energy levels. The goal of this work is to identify the optimum set of dopant(s), doping ratio, dopant concentration, and annealing temperature to maximize the up-converted emission efficiency.

1.4 Brief description of the work's procedure

Now, we introduce some brief details about the thesis' procedure. In this work, undoped and doped ceria nanoparticles are synthesized using chemical precipitation, where the dopants have been chosen from tri-valent lanthanide elements. The specific tri-valent dopant lanthanides are selected from two categories, elements that have positive binding or association energies (E_{ass}) between dopant ion and O-vacancies, such as samarium (E_{ass}= +0.01 eV) and neodymium (E_{ass}= +0.04 eV), and elements have negative association energies, such as holmium (E_{ass}= -0.54 eV) and erbium (E_{ass}= -0.46 eV) [27-29]. Each sample of doped ceria is characterized to obtain the data of optical and structural properties and this data is used to correlate these properties with the concentration and association energy of the dopant. The measured characteristics of the doped ceria are compared to undoped ceria, which is used as a reference material, to determine the impact of the selected dopant on the characteristics and the associated O-vacancies in ceria nanoparticles. The goal is to control the concentration of O-vacancies formed in doped ceria nanoparticles.

X-ray photoelectron spectroscopy measurement is performed for ceria doped with a single lanthanide element. Through XPS measurement, quantitative analyses of the chemical elements and their chemical states found within the top few nanometers of a surface are performed. Molar concentrations of the dopant elements in the nanoparticles are determined from the XPS data.

Mixed doped ceria (MDC) is another doping technique to validate conclusions obtained from our earlier study on the characteristics of ceria nanoparticles doped with a single dopant material. The MDC nanoparticles studied are doped with two lanthanide elements; one with a

positive association energy and the other with a negative association energy. Then, the obtained optical and structural characteristics of MDC are compared with the same characteristics obtained for ceria nanoparticles doped with only single positive association lanthanide. From the analysis of the measured characteristics of the MDC nanoaprticles, the concept of controlling the concentration of O-vacancies in ceria nanoparticles through the selection of the appropriate lanthanide elements based on association energy of the dopant is verified.

There is another class of tri-valent dopants, metal ions, which are also part of the studies conducted during this thesis project. Aluminum and iron; both of which can be in a tri-valent ionized state, are selected as dopants, due to studies that have shown their promising potential to improve the catalytic activity of ceria [22-30]. However, published studies on the optical and structural characteristics of doped ceria nanoparticles with these tri-valent metals, and an analysis to correlate the O-vacancy concentrations to the presence of these metal ion dopants, are nonexistent. Ceria nanoparticles doped with either or both metals are analyzed through the previously mentioned optical and structural characteristics with comparing the results obtained on the lanthanide-doped ceria nanoparticles to determine which of the selected dopants is the best in generating a higher concentration of O-vacancies associated to more numerous concentration of Ce in the Ce^{+3} ionization state.

In this thesis, some of the doped ceria nanoparticles studied are applied as optical sensor for dissolved oxygen based on fluorescence quenching technique Since we have found that the fluorescence intensity of the ceria nanoparticles increases with increasing concentration of O-vacancies and that the fluorescence signal quenched following thermal anneals, which also were found to decrease the concentration of O-vacancies in the material, the question arose whether the O-vacancy concentration of the nanoparticles, and thus the fluorescence signal collected from

the nanoparticles, could be correlated to the concentration of dissolved oxygen in an aqueous colloidal solution. The fluorescence experiment is performed under UV excitation and the emitted visible fluorescence spectrum is detected at incremental values of DO concentration. The amplitudes of the fluorescence signal as a function of DO concentration are used to determine Stern-Volmer constants for both undoped and doped ceria nanoparticles. The Stern-Volmer constant is an indication to the sensitivity of the used medium for DO sensing [31]. The obtained Stern-Volmer constants (K_{SV}) and the average sizes of the nanoparticles are compared with the K_{SV} and sizes of some of the fluorescent dyes currently used to detect DO in water in order to demonstrate that the ceria nanoparticles have a higher sensitivity and are of much smaller size and, thus, are a promising molecular probe in a fluorescence quenching DO sensor. To further demonstrate the potential of the ceria-based molecular probes in this important industrial application, the temperature stability of the Stern-Volmer constants of ceria nanoparticles is studied and found to be significantly more thermally stable.

The second application of doped ceria nanoparticles is optical up-conversion (UC). The goal in this portion of my thesis research is to demonstrate the significance of the doping technique on the efficiency of the up-conversion process where visible emission is obtained when the nanoparticles are under IR excitation. Due to the importance of up-conversion process in many optical applications [32], the radiated emission of the up-conversion process in doped ceria nanoparticles as a function of dopant atom and concentration will be presented. The samples studied are ceria doped with erbium (ceria:Er), due to the metastable levels of erbium suitable for the up-conversion process [33]. In addition, some selected lanthanide dopants are added to ceria:Er nanoparticles to determine if defect engineering using tri-valent dopant atoms can be used to improve the efficiency of the UC process. There are different measurements

performed in this part of the thesis project to the effect of doping ratios on the amplitudes of the emitted spectrum, the power dependence relation, and the effect of the synthesis temperature and of the lanthanide dopants selected on the O-vacancy concentration and the UC efficiency. The analysis of the UC measurements includes an evaluation of the alignment of the energy levels of Er^{+3}, and the other lanthanide dopants, and the concentration of the O-vacancies defects as determined from the optical and structural characteristics of doped ceria nanoparticles. The flowchart of the complete plan of work in the present thesis is shown in Fig. 1.1.

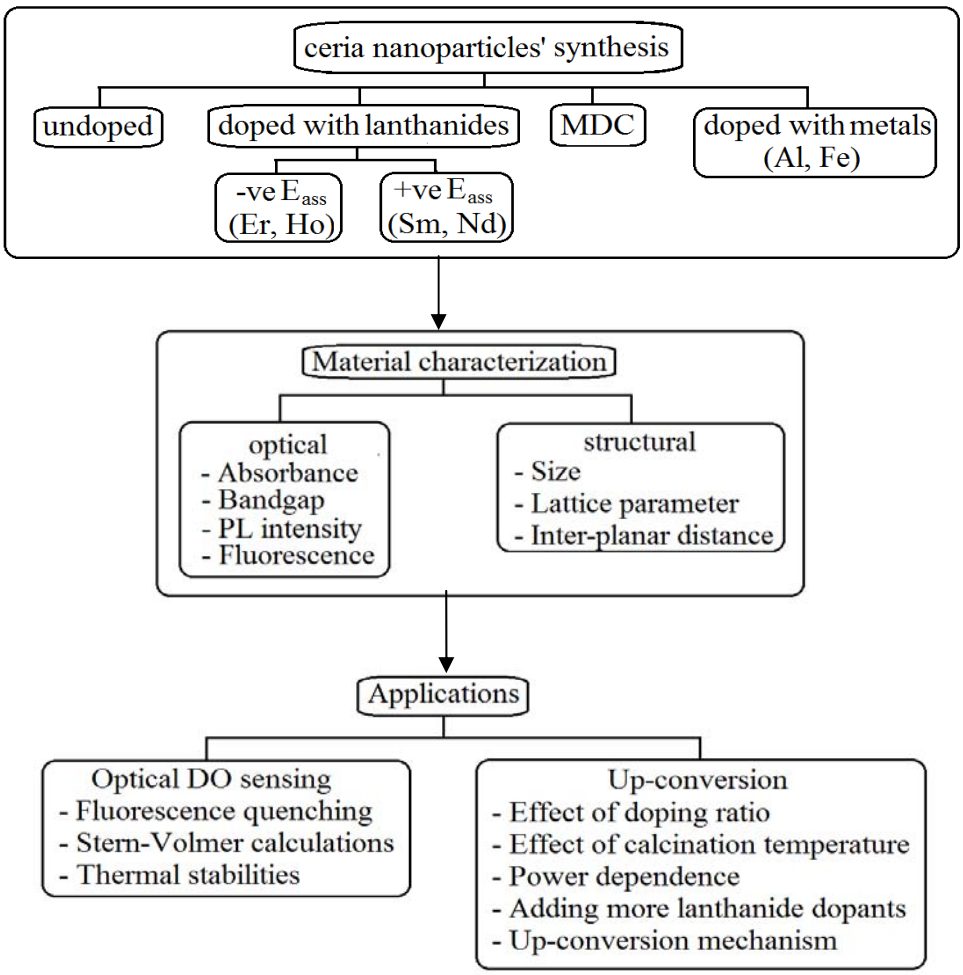

Fig. 1.1 Flowchart of the thesis' work plan

1.5 Thesis structure

- In Chapter 2, theoretical background is presented about the structure of ceria of both components; CeO_2 and Ce_2O_3. Also, the types of defects in ceria and the mechanism of O-vacancies mobility are discussed. The calculation of the direct bandgap from the absorbance dispersion is explained and the correlation between the bandgap and concentration of O-vacancies' concentration is justified. Then, the basics of fluorescence spectroscopy and the impact of the presence of O-vacancies on this phenomenon are reported. The size of the different compositions of doped and undoped nanoparticles calculated using measurements obtained from transmission electron microscopy (TEM) and X-ray diffractometer (XRD) are presented in this chapter, too. Also, the relation between the diameter of the synthesized nanoparticles and the concentration of O-vacancies is explained. A brief overview of XPS is introduced as a method used for quantitative analysis of the chemical composition of the doped ceria nanoparticles.
- In Chapter 3, the synthesis procedure of both undoped and doped ceria is presented. The details of the synthesis process are described in depth. The selected dopants are positive association energy lanthanides; neodymium and samarium, negative association energy lanthanides; holmium and erbium, and metal dopants; aluminum and iron. Also, mixed doped ceria (MDC) is synthesized containing two lanthanide dopants; one from the positive association category and another one from the negative association lanthanides. Then, the specifications of all instruments used in the characterization measurements to obtain the absorbance dispersion, the fluorescence spectrum, the images of the nanoparticles using TEM, the XRD patterns, and the XPS spectrum, are described.

- In Chapter 4, the impact of selected dopants on the optical and structural characteristics of ceria nanoparticles is presented. The curves of the measured absorbance dispersion and the corresponding direct bandgap calculations are presented. Then, the photoluminescence (PL) emission of the undoped ceria nanoparticles is shown to understand the nature of the material as a fluorescent media. Then, the fluorescence spectra due to UV excitation are presented for undoped ceria along with ceria doped with the previously mentioned elements. TEM images of undoped and doped ceria and its related diffraction rings are presented. From these images, some structural characteristics are determined such as the average diameters of the nanoparticles, the interplanar distances, and lattice parameters. XRD patterns are shown in this chapter to explain the orientation planes of nanoparticles' components. Also, XRD can offer another method to find the sizes of the nanoparticles, which is used to verify the measurements obtained from the TEM images. From all previous results, the relation between these results and the formation or scavenging of O-vacancies, along with the increase or decrease of the conversion from Ce^{+4} ions to Ce^{+3} ions, respectively, is described. XPS results of different lanthanide doped ceria nanoparticles are presented for chemical composition analysis of cerium and dopant elements.
- In Chapter 5, the first application; which is the dissolved oxygen optical sensing, is then introduced theoretically based on the optical fluorescence quenching concept. Based on the previous characteristics of chapter 4, undoped and doped ceria with selected lanthanides and metals are evaluated as fluorescence quenching DO sensing media. The experimental setup of optical DO sensing using fluorescence quenching is discussed in details, showing how to control and measure the DO concentration and how to detect the corresponding fluorescence spectrum. At room temperature, the fluorescence quenching spectrum is detected with

increasing DO concentration. Therefore, Stern-Volmer constants, which can be considered an indication for the sensitivity of DO sensing media, are calculated and compared with the constants values of some presently, used fluorescent dyes. The next measurement is to repeat the fluorescence quenching spectrum and Stern-Volmer graphs at different temperatures over the room temperature such as at 30, 40, and 50^{o}C, to study the temperature stability performance of DO sensing sensitivity of different doped ceria nanoparticles.

- The literature of the up-conversion process is discussed in Chapter 6, with explaining the importance of using ceria doped with erbium in IR to visible conversion, followed by presenting some details about different mechanisms of up-conversion. The used experimental procedure as fluorescence spectroscopy of Chapter 3 is discussed, in which ceria:Er nanoparticles are exposed to NIR excitation of 780 nm, instead of UV excitation, and the emitted visible spectrum is detected. The studied samples are doped ceria with erbium at different concentrations and with additional dopants, such as samarium and neodymium. In this part, there are some performed experiments to correlate the up-conversion efficiency with different parameters. Firstly, the emitted spectrum amplitude is correlated to the doping ratio of the erbium. Secondly, the effect of synthesis temperature of doped ceria nanoparticles on the up-conversion efficiency is discussed. In the next measurement, the relationship between the pumping power and the emitted power at the specific generated spectral regions; green and red, is studied to prove that the observed emission is a result of a two photons absorption process. Then, the relation between the obtained visible emissions and the up-conversion mechanisms is discussed and the available correlation with O-vacancies defects is checked.

- The conclusions generated from the results obtained from Chapters 4, 5, and 6, are summarized in Chapter 7; Conclusions and Future Work. Also, a proposal for research on some of the biomedical and industrial applications in the further research is presented briefly.

CHAPTER TWO

Theoretical Background: Doped Ceria Nanoparticles

2.1 The structure and defects of undoped and doped ceria

CeO_2 crystallizes in the fluorite structure, in which Ce^{+4} cation is surrounded by eight equivalent O^{-2} ions. There is a Ce^{+4} cation at each corner of a cube with each O^{-2} coordinated to four Ce^{+4}, as shown in Fig. 2.1a. If one considers the unit cell of ceria to be a face-centered cubic (FCC) structure composed of Ce^{+4} ions, the Ce^{+4} ions form a cubic close packing arrangement and all the tetrahedral sites around the Ce^{+4} ions are occupied by the oxygen ions whereas the octahedral sites remain vacant. The tetrahedral sites can be visualized by dividing the cube into eight smaller cubes. The body center positions of all the small cubes are occupied by oxygen ions and the alternate corners are occupied by Ce^{+4} ions [34].

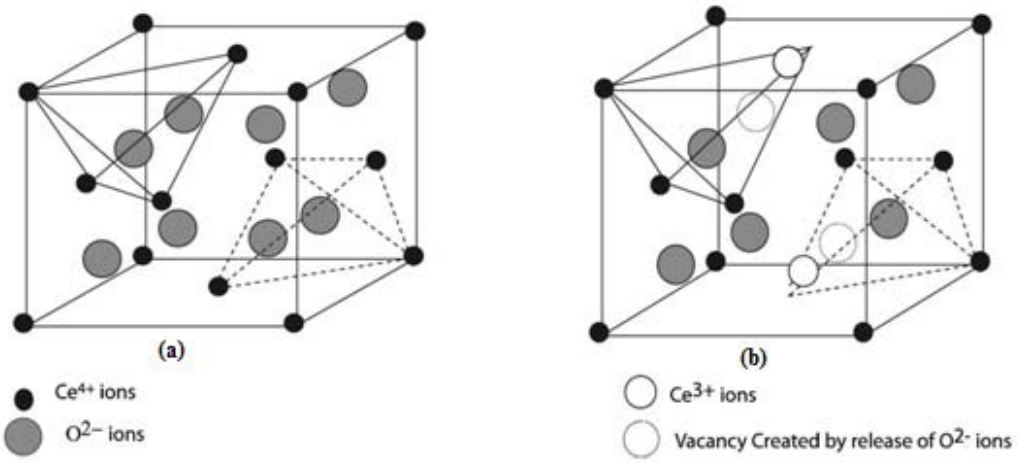

Fig. 2.1: Crystalline structure of CeO_2 a) without defects, b) with intrinsic defects [15].

Defects in ceria can be intrinsic or extrinsic. Intrinsic defects are presented due to thermal disorder or the surrounding atmosphere whereas the extrinsic defects are formed due to tri-valent impurities [35]. In the case of intrinsic defects, the coordination number of Ce^{+4} to O^{-2} reduces

from eight to seven at elevated temperatures, which introduces Ce^{+3} ions into the crystal lattice as two electrons from an oxygen atom are transferred to two cerium ions neighboring the oxygen ion, which leaves the unit cell and a vacancy site is formed (Fig. 2.1b). The cerium ions are reduced from the +4 state to the +3 state, which leads to form Ce^{+3} ions, with a Ce $4f^1$ configuration [36]. Formation of O-vacancies can be noticed from Kroger and Vink defect notation [37]

$$2Ce_{Ce} + O_O \rightarrow \frac{1}{2}O_2(gas) + V_{\ddot{o}} + 2Ce'_{Ce} \tag{2.1}$$

where Ce_{Ce} is a Ce^{+4} ion, Ce'_{ce} is the Ce^{+3} ion and $V_{\ddot{o}}$ is the doubly positively charged O-vacancies formed when O_2 gas is generated. Extrinsic defects are formed when a tri-valent dopant is substituted for a Ce^{+4} ion and the tri-valent oxide is instantaneously converted into the tri-valent ion and O-vacancy in the material with the oxygen atoms released from the crystal matrix. This process is shown in the following chemical reaction [38]

$$T_2O_3 \rightarrow 2T'_{Ce} + V_{\ddot{o}} + 3O_O^x \tag{2.2}$$

where T is the tri-valent element dopant atom, T'_{Ce} means electron-acceptor tri-valent ion formed in ceria, $V_{\ddot{O}}$ is doubly positively charged O-vacancy and O_O^x is the neutral oxygen atom.

However, Skala et al. reported that adding tri-valent atoms to ceria not only increases concentration of O-vacancies itself, but also increases the conversion rate from Ce^{+4} to Ce^{+3}[39]. This process leads to a higher concentration of O-vacancies than would be predicted solely from Equation (2.2).

The diffusion of oxygen through ceria materials occurs via a vacancy hopping mechanism [36]. Doping ceria with tri-valent atoms usually increases the ionic conductivity in

ceria compared to undoped ceria because ceria doped with most trivalent ions results in a lowering of the energy barrier for oxygen migration [40] which leads to higher mobility of oxygen vacancies as explained using Equation (2.3).

$$\sigma = \frac{\sigma_o}{T}\exp(-\frac{E_a}{K_B T}) \tag{2.3}$$

where the ionic conductivity (σ) can be expressed as an exponential function of the activation energy for oxygen vacancy diffusion (E_a). T stands for temperature, K_B for the Boltzman constant and σ_o for a temperature-independent conductivity prefactor. At low dopant content in the ceria system, most of the oxygen vacancies are free. While at high dopant content, the conductivity becomes lower because of the formation of defect associations (e.g., trivalent ion-oxygen vacancy complexes) due to Columbic attraction [38]. Activation energy (E_a) consists of migration energy (E_m), and association energy (E_{ass}), which prevents the O-vacancies of being mobile due to the binding energy between the dopant and the vacancy. E_{ass} becomes the dominant component of E_a within low and intermediate temperatures [27], which we are using in the synthesis procedure as will be discussed later in Chapter 3.

2.2 Optical characteristics of ceria

2.2.1 Absorption coefficient and direct bandgap calculations

The absorption coefficient α' is defined as the relative rate of decrease in light intensity $L(h\upsilon)$ along its propagation path [41]

$$\alpha' = \frac{1}{L(h\upsilon)}\frac{d[L(h\upsilon)]}{dx} \tag{2.4}$$

where α' is expressed in units of cm^{-1}. The absorption coefficient for a given photon energy $h\upsilon$ is proportional to the probability for the transition from the initial state to the final state of an atom,

ion, molecule, or crystal, where the difference in energy between the initial and final state is equal to the photon energy plus or minus the energy of any other particle (e.g., a phonon) that is involved in the transition, and also the density of available final states. This process must be summed for all possible transitions between states separated by an energy difference equal to hv plus or minus the energy of any other particles involved in the transition and also it is assumed that all lower states are filled and all upper states are empty. From Equation (2.4), it can be derived that the absorbance α, which is the logarithmic ratio between the light intensities in the absence and the presence of the material along the light path, with the allowed direct bandgap semiconductor can be shown as

$$\alpha(hv) = A^*(hv - E_g)^{1/2} \tag{2.5}$$

where A^* is a constant for any given material, which is defined as

$$A^* = \frac{q^2(2\frac{m_h^* m_e^*}{m_h^* + m_e^*})^{3/2}}{nch^2 m_e^*} \tag{2.6}$$

where q is the electron charge, m_e* is the effective electron mass, m_h* is the effective hole mass and n is the refractive index. From Equation (2.5), plotting α^2 with photon energy, the intersection with x-axis gives the value of direct allowed bandgap energy, E_g. The process of adding some doping elements or impurities in the semiconductor material is expected in many cases to reduce the effective bandgap energy because of band-to-impurity level transitions, when one consider the dopant to create a trap within the forbidden bandgap or due to local variations in the bandgap caused by the creation of the T_2O_3 and Ce_2O_3 molecules. The second effect gives rise to the Urbach tail in the absorption spectrum. The origin of this theory is that the impurities are distributed randomly within the crystal lattice; the local interaction will vary over the lattice as impurities cluster inhomogenously. That leads to local variances in the bandgap, caused by

impurities. The density of states (DOS) is associated with tails extending into the bandgap. If a photon is released during a transition from the final state to the initial state, the radiated energy can be significantly less than the incident photon energy used in the transition from the initial (or ground) to the final state [41-42]. This is shown schematically in Fig. 2.2.

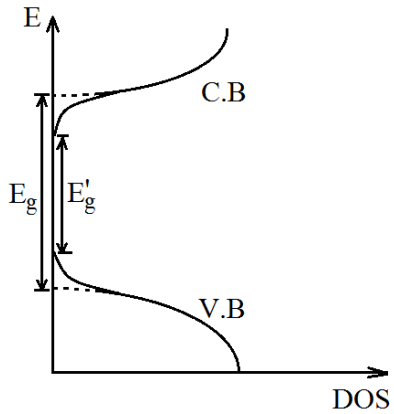

Fig. 2.2: Band tails due to impurities (C.B: Conduction band, V.B: Valence band, E_g: Bandgap, E_g': Reduced bandgap, and DOS: Density of states)

However, in ceria nanoparticles, there is another important factor that affects the energy of the bandgap, which is the number of O-vacancies or the conversion from Ce^{+4} to Ce^{+3} ions. The bandgap of CeO_2, which is a material where all of the cerium exists in the Ce^{+4} ionization state and there are no oxygen vacancies present, is roughly 4eV, but Ce^{+3} ions present in the crystal lattice, which could be considered a part of a Ce_2O_3 compound, they create a trap state 3eV above the CeO_2 valence band and correspond to the Ce5*d* - Ce4*f* transition [43]. The experimentally measured Ce_2O_3 bandgap ranges between 3.03 eV to 3.7 eV, depending on the synthesis method, growth and post-growth process temperatures, and the size of the particles [44].

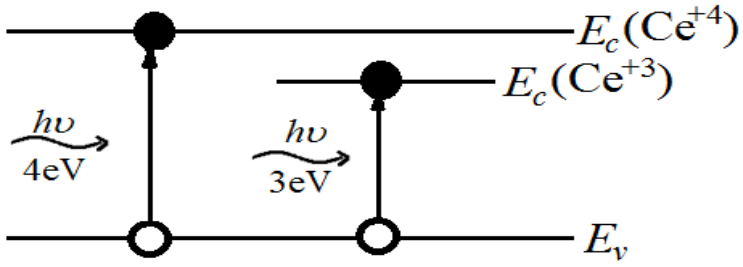

Fig. 2.3: Energy band for CeO_2, where cerium is in the Ce^{+4} state, and the trap level associated with cerium is in the Ce^{+3} state.

Given this analysis, the conclusions drawn after using the absorption data to calculate the bandgap E_g for undoped and doped ceria using Equation (2.5) is as follows: If E_g is close to 3 eV, the bandgap energy of Ce_2O_3, then the undoped ceria contains a high concentration of Ce^{+3} ions and the associated O-vacancies. If the ceria is doped, then the dopant incorporation has forced the formation of a high concentration of O-vacancies, which increases the concentration of Ce^{+3} ions. In the opposite case, if the measured E_g of doped ceria is not close to 3 eV and is nearer to 4 eV, then the dopant does not follow the reaction described in Equation (2.2). The dopant, instead, reduces some of the cerium present in the Ce^{+3} ionization state to Ce^{+4} or eliminates some of the O-vacancies, triggering a conversion of cerium from Ce^{+3} to Ce^{+4} (or forces the formation of CeO_2 from Ce_2O_3). As a summary, an indication of the excess conversion of Ce^{+3} and the presence of a high concentration of O-vacancies is a measured bandgap energy that is very close to 3 eV [45].

2.2.2 Theory of fluorescence

Luminescence is the emission of photons from a material where the emission spectrum is not directly determined by the sample's temperature as is the case for blackbody radiators [43]. This occurs when an electron from an excited state relaxes to a lower state, releasing a photon in the process. The excitation can take place in numerous forms. If the electron is excited by an

electrical current, it is called electroluminescence. Excitation by a chemical process is known as chemiluminescence. When the excitation takes place in mechanical form, it is mechanoluminescence.

Photoluminescence is the more general term, which describes the process in which a substance absorbs photons (electromagnetic radiation) and then re-radiates photons. In a simple absorption process that involved only excitation light and the absorber, as shown in Fig. 2.4, the incoming light with photon energy $h\nu$ will excite the electrons from a ground state E_1 to an upper energy level E_2, where the photon energy $h\nu$ must be at least equal to E_2-E_1. If the photon energy ($h\nu$) is larger than E_2-E_1, the excess energy will be released as heat.

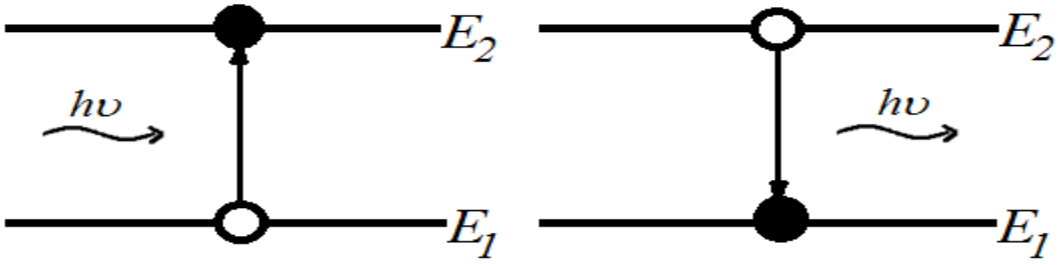

(a) (b)

Fig. 2.4: Schematic diagrams of a) absorption process and b) excitation process

The emission of photons in photoluminescence occurs in two forms: first one is phosphorescence, which occurs when photons continue to radiate in relatively long time after the excitation has stopped due to the fact that the excited state has an extremely long lifetime (typically, this is in the order of milliseconds). The second form is fluorescence, which the process when the excited electrons stay in the upper energy band for a very short time before dropping to the ground level. Thus, the excited state has a relatively short lifetime (in the order

of nanoseconds). Schematically, these two forms of photoluminescence are shown in a Jablonski diagram, as presented in Fig. 2.5 [46].

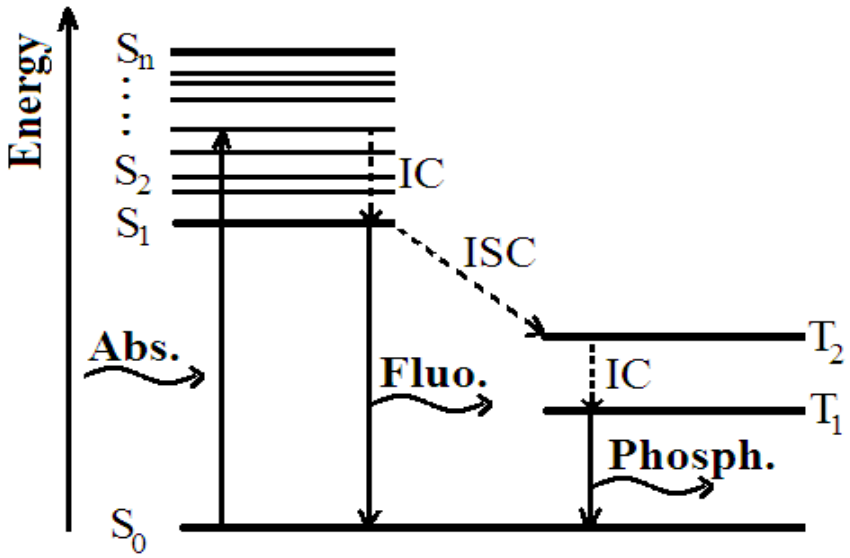

Fig. 2.5: Jablonski diagram showing processes involved in fluorescence, where "Abs." is the absorbed photon, "Fluo." is the fluorescence emission, "Phosph." is the phosphorescence emission, "S" is a singlet state, "S_0" is the ground state, T is a triplet state with long lifetime, IC is the internal conversion for excited vibrational states when the absorbed photon has more energy than the radiated photon, and ISC is the intersystem crossing.

The 4 eV bandgap of ceria, arising conceptually from either Ce^{+4} or CeO_2, is an indirect gap; therefore, there will be a very small probability that radiative recombination will occur when absorption takes place. However, the relaxation via the 5d-4f transition of the Ce^{+3} ions (or Ce_2O_3), which has a direct bandgap, results in photon emission when ceria is excited with around 400 nm light [43], causing the conduction band electrons to make a transition to the defect state within the bandgap. From the defect state, the electron undergoes multiple transitions in order to return to the ground state according to Shockley Reed Hall recombination [47]. The wavelengths of the emitted radiative photons, as will be shown later in Chapter 4, are centered around 520 nm. The remaining transitions as the system returns to the ground state are non-radiative. Thus, a

large amplitude for the fluorescent intensity peak is an indication that the material contains a high concentration of Ce^{+3} ions, which is associated with a high concentration of O-vacancies. Vice versa, materials that contain a high concentration of O-vacancies and Ce^{+3} ions should be good fluorophores.

2.3 Structural Characteristics of ceria

Measurement of the average particle size of the synthesized nanoparticles is done directly from the image obtained by transmission electron microscopy (TEM) or by calculations performed on the data obtained from X-ray diffraction (XRD) patterns. In TEM, a thin specimen is irradiated with an accelerated electron beam of uniform current density. Electrons interact strongly with atoms by elastic and inelastic scattering. The electron-intensity distribution behind the specimen is imaged with a lens system, composed of three to eight lenses, onto a fluorescent screen. The image, which contains the nanoparticles, can be recorded by direct exposure to a couple-charge device (CCD) camera. The average diameter of the nanoparticles can be found from the mean of a population with a Gaussian distribution that must include high number of measured diameters. Using diffraction mode in TEM, the diffraction rings can be imaged, which indicate the surface planes of the formed material. From the radius of the first ring, which is a result of the diffraction from the (111) planes of ceria [48], the interplanar-distance of the prepared samples is found from the following equation [49]

$$\lambda L = Rd \tag{2.7}$$

where λ is the wavelength associated to the accelerated electron, L is the camera length, R is the radius of the diffraction ring and d is the inter-planar distance of the material. Lattice parameter is calculated from the formula [50]

$$a = d\sqrt{h^2 + k^2 + l^2} \quad (2.8)$$

where *h*, *k* and *l* are the miller indices of the plane, which is (111) in ceria.

XRD is used to determine the crystalline structure of the material. The intensity peaks of the X-rays indicate the structural planes, which are responsible for the diffraction of X-rays. From the measurement of the width of individual intensity peaks, the average size (t_{XRD}) of nanoparticles, or diameter in case of spherical shape nanoparticles, can be calculated from Scherrer's equation [50]

$$t_{XRD} = \frac{0.9\lambda}{\beta cos\theta} \quad (2.9)$$

where λ is the wavelength of the incident X-rays (0.15406nm), β is full-width half-maximum (FWHM), and θ is the diffraction angle.

It is reported that the increase in the lattice parameter of ceria nanoparticles with decreasing particle size is attributed to the lattice strain induced by the creation of oxygen vacancies along with the formation of Ce^{+3} ions in the cerium oxide crystal structure [15]. Hence, the size of the synthesized ceria nanoparticles can give an indication of the conversion rate of cerium from Ce^{+4} to Ce^{+3} ions or the concentration of the associated O-vacancies.

2.4 XPS analysis

X-ray photoelectron spectroscopy (XPS) is concerned with a special form of photoemission in which an electron is ejected from a core level by X-ray photon exposure. The kinetic energy of the emitted photoelectrons (E_K) is analyzed by the electron spectrometer and

the data is presented as a graph of intensity versus the electron energy. Then, the binding energy of the electron (E_B) is the calculated intrinsic parameter as follows

$$E_B = h\nu - E_K - W \tag{2.10}$$

where hυ is the photon energy and W is the spectrometer work function. The photoelectron spectrum is producing the electronic structure of an element quite accurately for the electrons with a binding energy less than the photon energy presented in the spectrum. The energies of the extracted electrons interpret the chemical composition of the studied material [51].

In this work, the concentration of the dopant elements in the nanoparticles can be determined from the XPS data, though some assumptions have to be made about the yield of photoelectrons from various atoms. Given that there is some ambiguity over the accuracy of the calculated ionization state of cerium due to changes that can be induced during evacuation of the measurement chamber and as a result of high energy irradiation, this technique is not used to quantify the concentration of Ce^{+4} and Ce^{+3} in the nanoparticle samples [25]. However, it is used as a qualitative confirmation of the trends determined from an analysis of the data collected using the other characterization techniques.

CHAPTER THREE

Synthesis and Characterization: Experimental processes

3.1 Experimental procedure of the synthesis process

3.1.1 Synthesis of undoped and single doped ceria nanoparticles

Ceria nanoparticles are prepared using a chemical precipitation technique as described by Chen and Chang [52] with some modifications. Initially, 0.5 g of cerium (III) chloride (heptahydrate, 99.9%, Aldrich chemicals) is added to 40 mL de-ionized water as a solvent. The solution is stirred at rate of 500 rpm for 24 hours through two stages. In the first step, the solution heated to 50^{o}C in normal atmosphere while stirring; 1.6 mL of ammonia is then added after one minute to ensure that the solution becomes homogenous. The color of the product initially is purple and, over the period of approximately 30 – 60 minutes at 50℃, turned into yellowish color as the cerium chloride reacts with the ammonia to form cerium hydroxide. As the process is continued for a total of 1.5 hours, the colloid turns into white color, indicating the cerium hydroxide has reacted to form cerium oxide. The heating stage is important because it helps in the conversion of $Ce(OH)_3$ to CeO_2 (Ce^{+4} ions) and then to Ce_2O_3(Ce^{+3} ions) [53]. However, the selected temperature is not relatively high, compared to synthesis processes described in other research work [37], and is chosen to reduce agglomeration of the formed nanoparticles.

In the second stage of the synthesis procedure, the solution is stirred for an additional 22.5 hours in room temperature. The long period of stirring will fracture any nanorods that are formed during the initial reaction into nanoparticles. Then, the solution is centrifuged and washed with de-ionized water and ethanol twice to remove any unreacted cerium and ammonia. After each time that the colloidal solution is centrifuged and washed, the solution is sonicated in

DI water to break apart any agglomeration of the ceria nanoparticles. The synthesize procedure can be summarized in the flowchart drawn in Fig. 3.1.

Doped ceria with the various trivalent elements are synthesized using a similar procedure, but the amount of cerium chloride and the doping element-chloride reagents used in the synthesis reaction depend on the desired ratio of dopant atom to cerium atom in the nanoparticles that are formed. The doping weight ratios of cerium and lanthanide chlorides are shown in Table 3.1. The rare earth element-chloride salts used are neodymium chloride, samarium chloride, holmium chloride, and erbium chloride. Also, aluminum chloride and iron chloride are used in the doping process to compare the results of Al- and Fe-doped ceria nanoparticles with the ceria nanoparticles containing the low association energy rare earth doping elements, Nd and Sm.

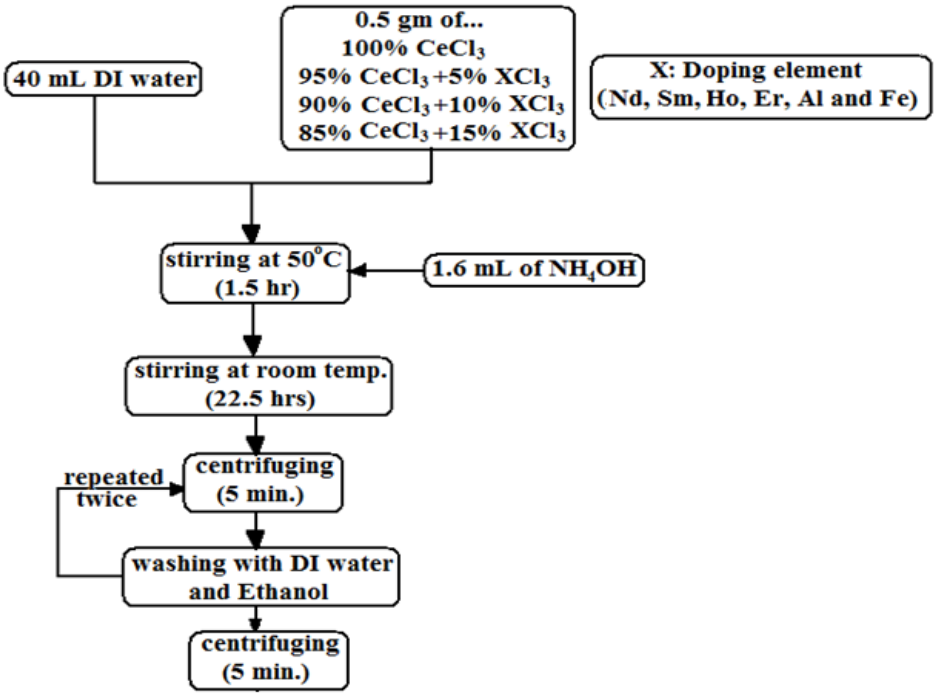

Fig. 3.1: Flowchart of the synthesis procedure for undoped and doped ceria nanoparticles

Doping reagent weight ratio	Cerium chloride weight (g)	Dopant chloride weight (g)
5%	0.475	0.025
10%	0.450	0.050
15%	0.425	0.075

Table 3.1: Doping weight ratios of the initial precursors for single doped ceria

3.1.2 Synthesis of mixed doped ceria

To provide additional data on the effect of the association energy of the dopant, mixed dopant ceria (MDC) nanoparticles are synthesized to incorporate two lanthanide elements in ceria nanoparticles, a positive association energy element, Nd or Sm, and a negative association energy element, Ho or Er. The synthesize procedure is the same but the initial salts' weights are as shown in Table 3.2.

MDC composition	Cerium chloride weight (g)	-ve E_{ass} lanthanide "Ho or Er" chloride weight (g)	+ve E_{ass} lanthanide "Sm or Nd" chloride weight (g)
Equal*	0.45	0.05	0.05
Double**	0.45	0.10	0.05

Table 3.2: Doping weight ratios of the initial precursors in MDC nanoparticles

* Equal means the –ve and +ve E_{ass} lanthanides weights are equal.

** Double means that –ve E_{ass} lanthanides weights are double the weight of –ve E_{ass} lanthanides.

3.2 Experimental procedure of optical and structure characterization

3.2.1 Experimental facilities for measuring the optical characteristics

To measure the absorbance dispersion, the solutions of concentration 1 mg/mL are inserted in a UV fluorometer methacrylate cuvette and exposed to the light signal of the UV-spectrometer; UV-3101PC Shimadzu. A reference light signal passes through a cuvette filled with water. The spectrometer software, UV Probe, compares the intensity of the light that passed through the solution of nanoparticles to the signal obtained from the reference and a calculation of the absorbance is performed using the Beer-Lambert Law. The absorption spectra are measured from 350 nm, which is well above the bandgap energy of Ce_2O_3, to 800 nm, which is usually beyond the extent of the Urbach tail. From the linear region of the absorbance dispersion curves that includes the Urbach tail, the allowed direct bandgap can be calculated, as discussed previously, using Equation (2.5).

The fluorescence intensity and spectrum of the samples are measured using a home-built fluorescence spectroscopy system, as described in Fig. 3.2. The setup consists of a UV lamp, 150 Watt Xenon UV Enhanced Arc lamp, Newport model no. 6254, where the emission is directed through the first monochromator, Newport Cornerstone 260 ¼ M Monochromator. The grating on the first monochromator is adjusted to allow light at a wavelength of 430 nm to leave the output port of the monochromator. This light is directed on to a cuvette containing a relatively concentrated solution of ceria nanoparticles, of concentration 2 mg/mL. This concentration, after some trials, is selected because it is high enough that a significant amount of photons to be produced but low enough that the photons can exit the cuvette with minimal scattering and minimum self-absorption. Then, a second monochromator, of a similar model to the first

monochromator, is positioned at 90° angle to the optical path of the light from the first monochromator so that the fluorescence emission can be measured with minimal scattered light from entering the second monochromator. The outlet of the second monochromator is connected to a photomultiplier tube (PMT), Newport PMT 77340, to amplify the fluorescence signal. Then, this amplified signal is detected using a power meter, Newport Power meter 2935C. The second monochromator is scanned from 500 nm to 700 nm to obtain the fluorescence spectrum.

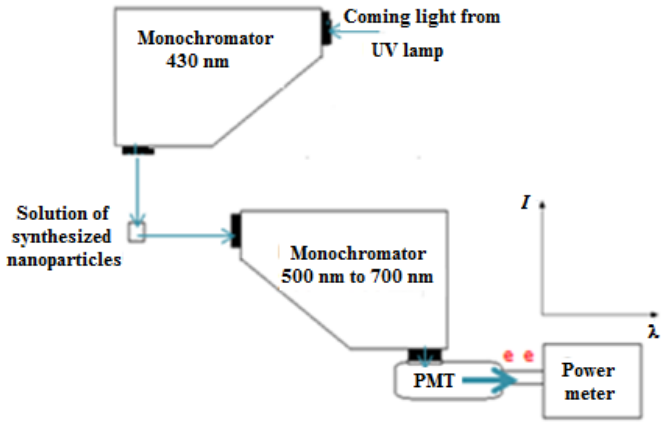

Fig. 3.2: Schematic diagram of the fluorescence spectroscopy setup.

3.2.2 Measurement facilities for Structural properties

Nanoparticles of different compositions are imaged using transmission electron microscope (TEM), Philips EM420, using accelerating potential of 120 KV. The TEM samples are prepared by immersing carbon-copper mesh grids in colloidal solutions containing the same concentration of nanoparticles that are used during the absorption measurements. The grids are then left to be dried for 30 minutes before imaging. From the TEM images, the average diameter of these nanoparticles can be found. Also, the interplanar distance and the lattice parameter of the undoped and doped ceria nanocrystals can be calculated from measurements taken on the

electron diffraction rings, which can be imaged using the TEM, where the camera length used is 600 mm. To determine the structure of the formed nanoparticles, the surface planes of different samples are measured using a PANalytical's X'Pert PRO X-ray diffractometer (XRD), at 45 KV and 40 A with Cu K_α radiation (λ=0.154 nm), to verify that the nanoparticles are composed of cerium oxide. Also, the average diameter of the nanoparticles can be calculated from the first diffraction peak; which is a result of constructive and destructive scattering off of the (111) plane of ceria, as mentioned in Section 2.3 of Chapter Two, which can be used as verification to the results calculated from TEM measurements.

The concentrations of the chemical components of the synthesized nanoparticles are measured using a PHI Quantera SXM scanning x-ray photoelectron spectroscopy (XPS). Samples are prepared by drying colloidal solutions on quartz slides. Quantitative analyses of the chemical elements and their chemical states found within the top few nanometers of a surface are performed.

CHAPTER FOUR

Optical and Structural Characterization: Results & Discussions

4.1 Characterization of undoped ceria nanoparticles

4.1.1 Absorbance dispersion and optical direct bandgap

The absorbance dispersions are determined for the undoped ceria nanoparticles sample synthesized during this project. Fig. 4.1a is the absorption dispersion curve for undoped ceria nanoparticles. Based on Equation (2.5), $(\alpha E)^2$ versus E is plotted, as shown in Fig. 4.1b. The intersection of the linear portion extrapolation of the $(\alpha E)^2$ curve with E-axis is equal to the allowed direct bandgap of undoped ceria nanoparticles. The bandgap calculated from the absorption data is 3.26 eV, which is an intermediate value between 3 eV, the defect bandgap of Ce_2O_3, and 4 eV, the bandgap of CeO_2. This provides evidence that our synthesized undoped ceria nanoparticles contain a significant number of cerium atoms in the Ce^{+3} ionization state as well as cerium in the Ce^{+4} states along with the associated O-vacancies, as explained theoretically in Chapter 2.

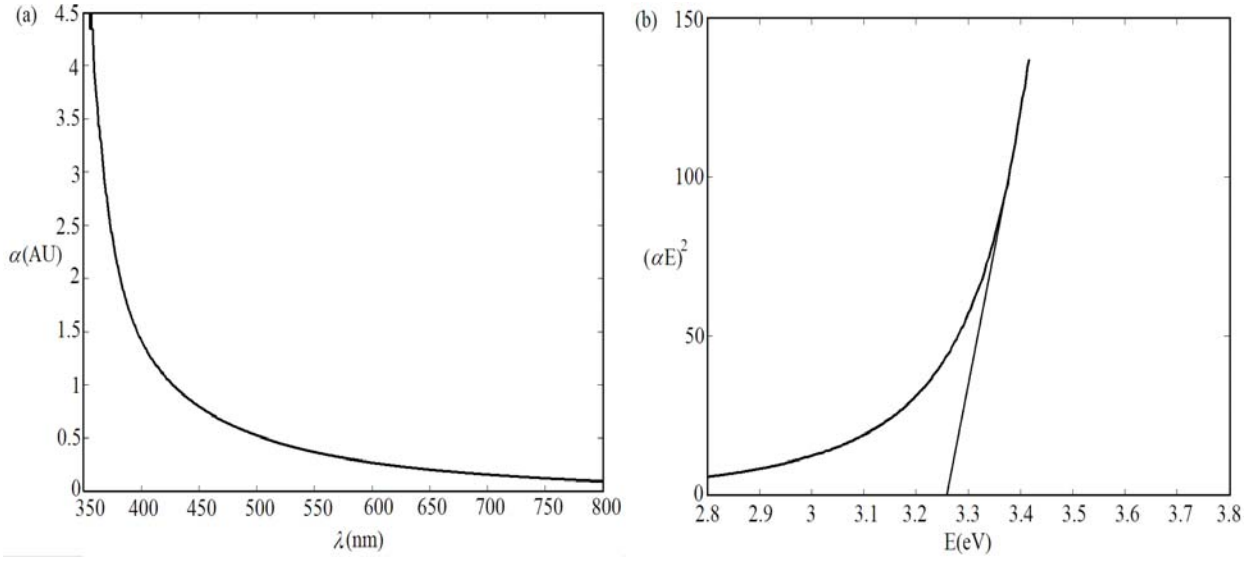

Fig. 4.1: a) Absorbance dispersion and b) $(\alpha E)^2$ versus E used to determine direct allowed bandgap energy of undoped ceria nanoparticles

4.1.2 PL intensity and fluorescence emission

Studies of the photoluminescence of the synthesized undoped ceria are important for understanding the fluorescence properties of the material. The same fluorescence setup, mentioned in Section 3.2.1, is used with the exception that the grating of the first monochromator is adjusted such that the light exciting the monochromator is at fixed wavelength of 370 nm, which is used as the excitation wavelength. The resulting emission spectrum from undoped ceria nanoparticles is presented in Fig. 4.2. The data shows that there is a very strong emission at 430 nm, which is related to the transfer of charges from oxygen ion to cerium ion [54]. This strong emission has been noted in published studies by other researchers [48-55]. Another small peak in the photoluminescence spectrum appears around 520 nm, which is associated with the oxygen vacancies defects or traps formed within the synthesized ceria and this emission wavelength is also consistent with other research work [56]. The amplitude of this emission can be correlated with the concentration of oxygen vacancies in the ceria nanoparticles. This PL analysis is essential to understand the origin of the optical emission of the nanoparticles studied.

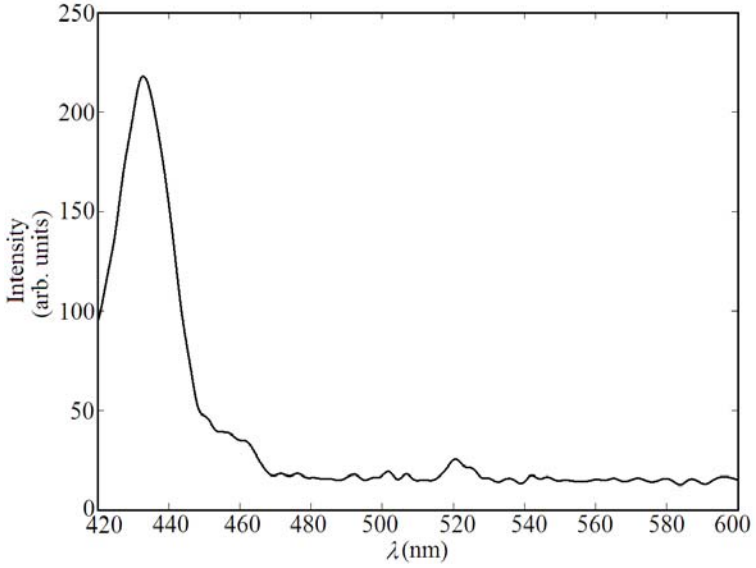

Fig. 4.2: PL intensity of undoped ceria, under 370 nm excitation

Fluorescence spectroscopy is performed using an excitation wavelength of 430 nm, obtained by adjusting the grating in the first monochromator to this wavelength value. Measurements are made from 500 nm to 600 nm. Visible emission is detected with a peak at 520 nm, as shown in Fig. 4.3. The emitted fluorescent signal demonstrates that the synthesized material includes cerium ions in the Ce^{+3} ionization state, which are associated with O-vacancies. To explain the fluorescence emission of Fig. 4.3, as explained in section 2.2.2, ceria is exposed with 430nm excitation, causing the conduction band electrons to make transitions to the defect state. From the defect state, the electron undergoes multiple transitions in order to return to the ground state and the peak radiative intensity is found to be green emission, existed at wavelength near 520 nm. Therefore, that indicates another piece of evidence that the formed ceria nanoparticles contain Ce^{+3} states with associated O-vacancies.

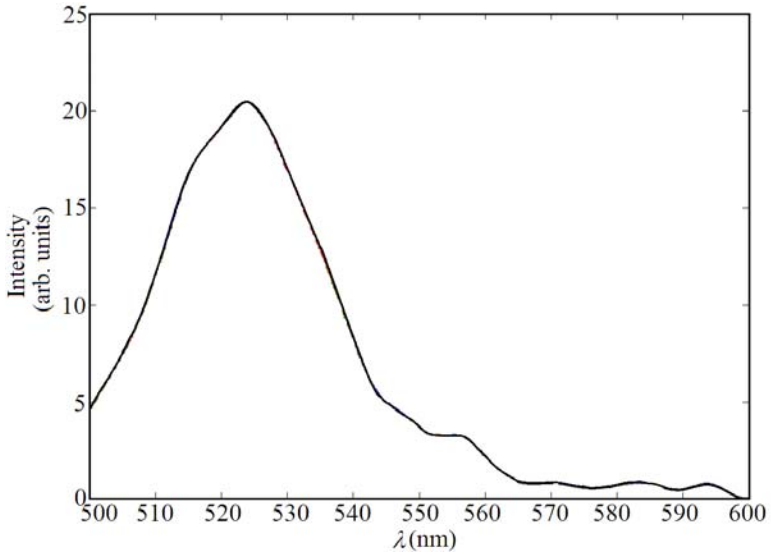

Fig. 4.3: Fluorescence emission of undoped ceria nanoparticles under 430 nm excitation

4.1.3. TEM and XRD analysis

TEM image of ceria nanoparticles, associated with diffraction rings "inset", is shown in Fig. 4.4a. The average size, interplanar distances, and lattice parameters of the nanoparticles are calculated to be 6.75 nm, 3.03 Å and 5.22 Å. X-ray diffraction (XRD) pattern of the synthesized nanoparticles is presented in Fig. 4.4b. The resulted pattern ensures that the crystalline structure of the formed nanoparticles belong to ceria [57]. The average particle size from XRD is found to be 6.83nm which is in a good agreement to the result obtained from the TEM images.

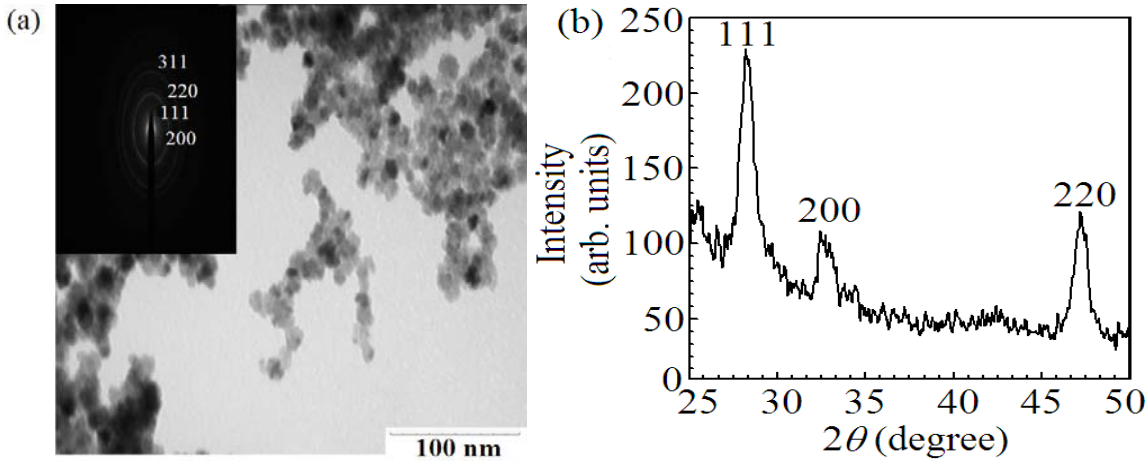

Fig. 4.4: Structural characterizations of ceria nanoparticles a) TEM image with diffraction rings and b) XRD pattern

4.2 Characterization of single lanthanide doped ceria

4.2.1 Absorbance dispersion and direct allowed bandgap

The studied lanthanide doped ceria samples are doped ceria with positive association energy lanthanides; neodymium and samarium, and doped ceria with negative association energy lanthanides; holmium and erbium. The absorbance dispersions of some examples of doped ceria samples are presented in Fig. 4.5. The absorbance curves versus the wavelength; the dispersions of absorbance, for the all doped ceria samples have the same behavior as the undoped ceria with

some differences in the linear regions. In positive association dopants, the absorbance is increased with increasing the doping weight ratio at the wavelength region between 350 nm to 400 nm while the opposite behavior is mostly existed when doping ceria within negative association lanthanides. The associated direct allowed bandgap calculations of some examples of doped ceria are shown in Fig. 4.6. The bandgap values of the whole undoped and doped ceria samples are summarized in Table 4.1. From this table, it can be observed that the direct allowed bandgap becomes lower than undoped ceria when doping with the positive association lanthanides; Nd and Sm, and it becomes much lower by increasing the doping weight ratio. That gives an indication that there are more formed O-vacancies associated to more formed Ce^{+3} ionization states when the concentration of Nd or Sm is increased in the ceria nanoparticles.

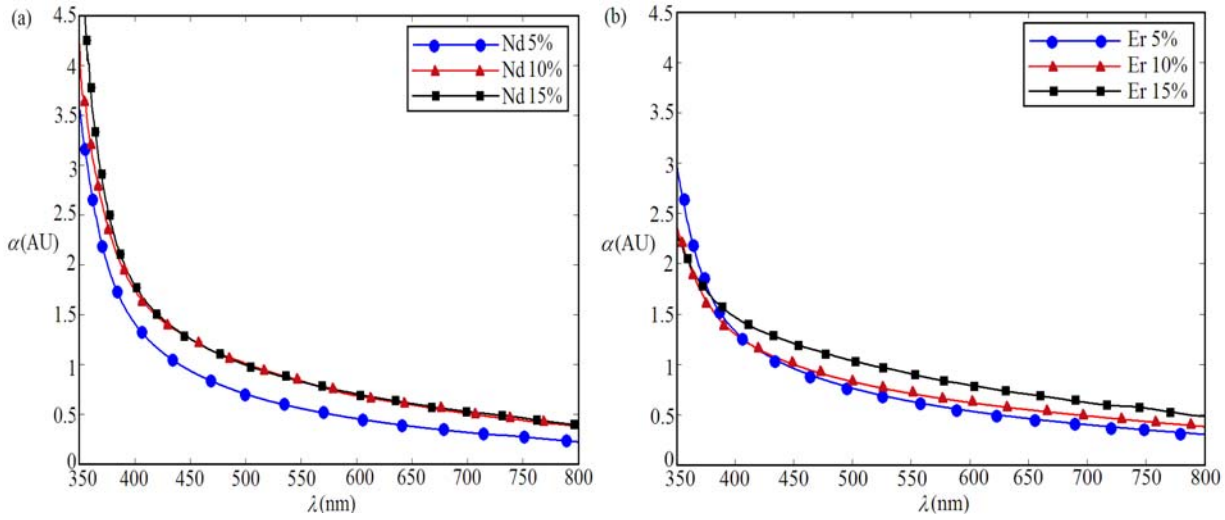

Fig. 4.5: Absorbance dispersion of doped ceria with (a) Nd and (b) Er, at different reagent weight ratios

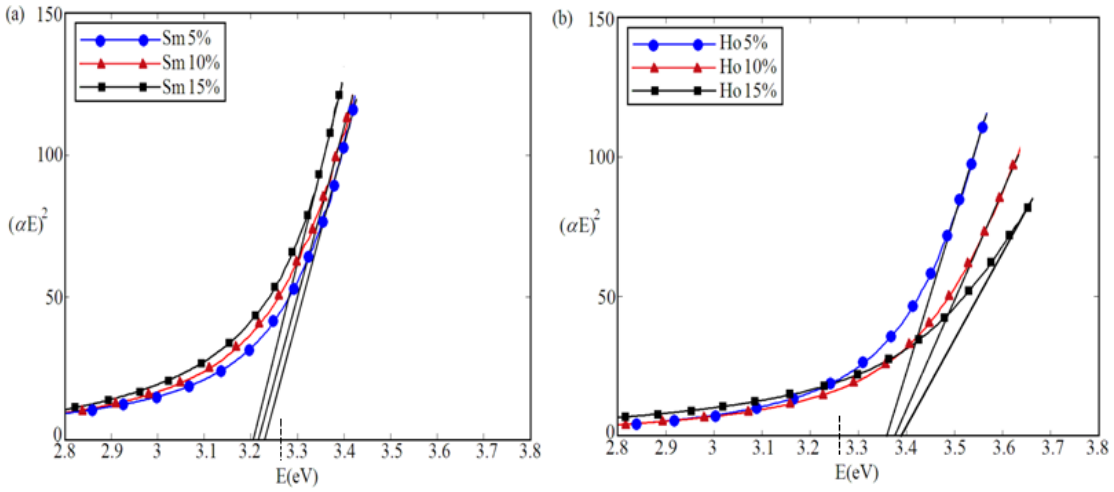

Fig. 4.6: Direct bandgap calculation of doped ceria with (a) Sm and (b) Ho, at different reagent weight ratios "dotted line is the bandgap of undoped ceria"

In opposite, doping with Ho and Er; the negative association lanthanides, causes an increase in the bandgap of synthesized doped ceria, compared to that of the undoped ceria. The bandgap energy becomes higher as the doping concentration is increased which indicates, as a novel approach, that there are lower O-vacancies in the nanoparticles associated to less conversion from Ce^{+4} ionization states to Ce^{+3} states. In other words, these negative association lanthanide dopants can act as O-vacancy scavengers while the positive association ones act as O-vacancy generators.

4.2.2 Fluorescence emission intensities

The fluorescent emissions of some doped ceria samples are shown in Fig. 4.7 and the complete peak emission values are reported in Table 4.1. Based on the obtained fluorescence results, the peak emission is higher in case of doping with the positive association energy elements; Nd and Sm, compared to the undoped ceria, which ensures that there are more Ce^{+3} ions and formed O-vacancies. Given that the number of photons that are emitted from the material via spontaneous emission, which is interpreted as the peak of the emitted intensity on

the power meter, is proportional to the number of excited electrons in the conduction band that relax via a radiative pathway. As the integration of the fluorescence intensity is proportional to the number of excited electrons and the shape of the fluorescence spectra is unchanged with doping. Therefore, the peak intensity is proportional to the electron concentration. In summary, the higher fluorescence intensity peak indicates that there is a higher concentration of Ce^{+3} states. The opposite behavior is found when doping with negative association energy dopants; Ho and Er, giving an indication to the reduction of O-vacancies; less conversion from Ce^{+4} to Ce^{+3}. These two conclusions are in a good agreement within the results obtained from the direct bandgap calculations.

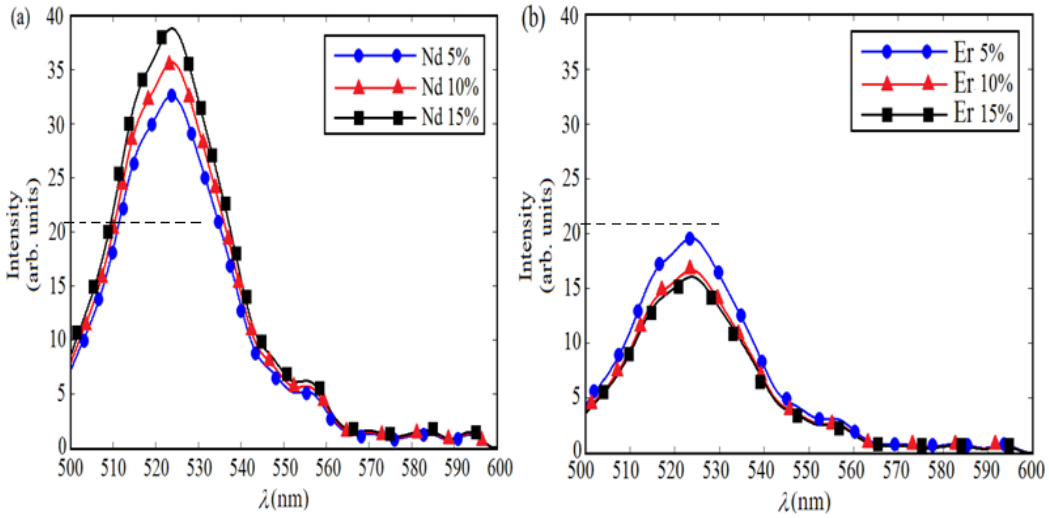

Fig. 4.7: Emitted fluorescent intensity of doped ceria with a) Nd and b) Er "dotted line is the fluorescence peak of undoped ceria"

4.2.3 Results of the structural parameters

TEM images of the doped ceria nanoparticles, associated with diffraction rings, are obtained experimentally. Some of TEM images of the formed nanoparticles and its associated diffraction rings are shown in Fig. 4.8, and the whole measured average nanoparticles' size, interplanar distances and lattice parameters for all samples are calculated and reported in Table 4.1. From these results, it can be observed that the particle size becomes smaller with the increase of both interplanar distance and lattice parameter when doping ceria with positive association energy elements. That supports the conclusion that the O-vacancies, associated to Ce^{+3} ions, are increased with this category of lanthanide dopants. The opposite result is found when doping ceria with negative association energy elements. This conclusion agrees with the conclusions verified from direct bandgap calculations and fluorescence measurements.

XRD patterns of some lanthanide doped ceria, as examples, are presented in Fig. 4.9. The peaks shown in this figure are associated with the different surface planes of the formed ceria nanoparticles. To determine the structure of the formed nanoparticles, the patterns of different samples are measured through x-ray diffractometer (XRD). From the first pattern peak, the average particles' diameter can be calculated through Scherrer's formula; Equation (2.9). The complete results of diameters obtained from XRD for all of lanthanide doped ceria samples are reported in Table 4.1. The mean diameter of the different doped ceria obtained by XRD show good agreement to the results obtained from TEM images.

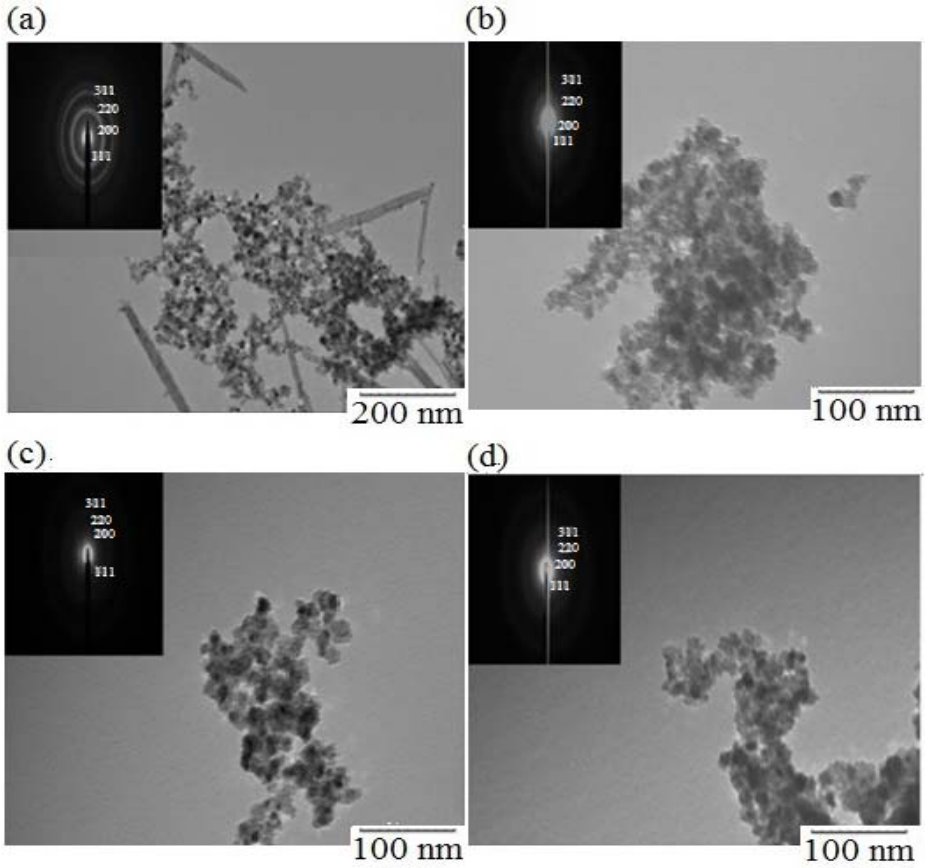

Fig. 4.8: TEM images and diffraction rings of ceria doped with 5% reagent weight of a) Ho, b) Er, c) Nd, and d) Sm

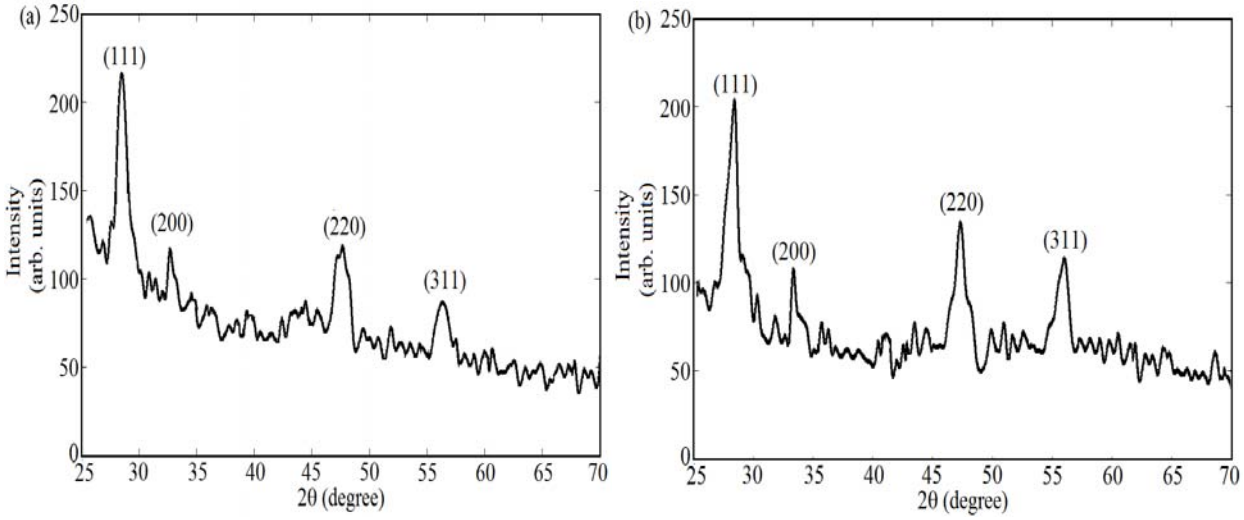

Fig. 4.9: XRD patterns of ceria doped with 5% reagent weight of a) Sm and b) Nd

Material		Direct Eg (eV)	Peak fluorescence (arb. units)	Lattice parameter (Å)	Inter-planar distance (Å)	Mean particle size using TEM (nm)	Mean particle size using XRD (nm)
Undoped ceria		3.26	20.63	5.22	3.03	6.75	6.83
Doping with Nd	5%	3.22	32.75	5.30	3.04	6.29	6.30
	10%	3.21	35.68	5.35	3.07	6.23	6.29
	15%	3.20	39.04	5.38	3.09	6.21	6.10
Doping with Sm	5%	3.23	25.81	5.27	3.06	6.48	6.55
	10%	3.22	28.15	5.31	3.09	6.39	6.45
	15%	3.21	30.97	5.35	3.11	6.24	6.30
Doping with Ho	5%	3.36	19.48	5.09	2.94	7.36	7.12
	10%	3.38	16.11	4.99	2.88	7.48	7.44
	15%	3.39	15.38	4.94	2.85	7.60	7.79
Doping with Er	5%	3.30	19.90	5.08	2.93	7.21	7.12
	10%	3.31	16.71	5.04	2.91	7.25	7.31
	15%	3.32	15.85	5.01	2.89	7.33	7.31

Table 4.1: Optical and structural data of the whole ceria samples, pure and doped with rare earth elements

Experimentally, there are some additional peaks found in XRD pattern related to $Ce(OH)_3$. However, these peaks are removed from the shown figures; 4.9a and b, because $Ce(OH)_3$ component is not originally found in the powder. Experimentally, the samples of undoped and doped ceria were found to be converted slowly to $Ce(OH)_3$ inside XRD cabinet over the measurement period, which is up to one hour. There are two pieces of evidence of this conversion reaction. Firstly, the color of the powder is changed from white, indicative of ceria, to yellow, which is an indication for $Ce(OH)_3$, after the end of XRD measurement as shown in Fig. 4.10. Second piece of evidence for that conversion process is that the peaks of $Ce(OH)_3$ are very narrow; very small FWHM. Therefore, the size of $Ce(OH)_3$ nanoparticles is calculated to be relatively large; around 25 nm based on our calculations. These relatively large nanoparticles are not observed in the TEM images. Then, it can be concluded that this additional material is formed in XRD cabinet only and it was not originally found in the synthesized powder.

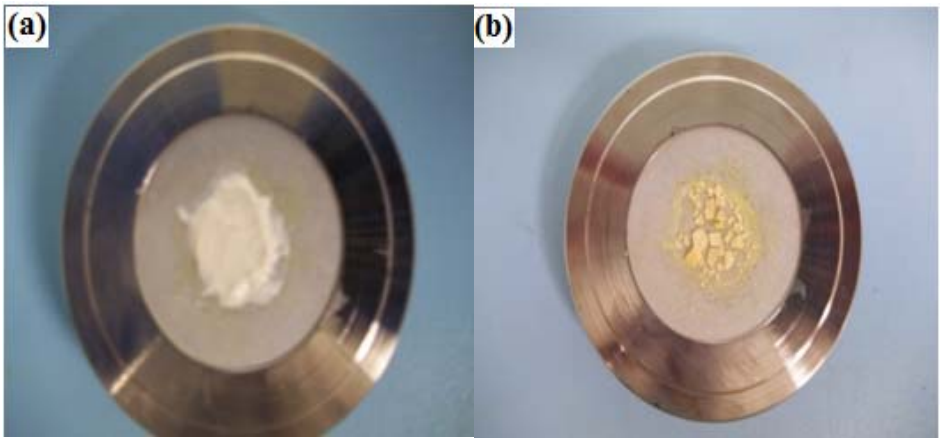

Fig. 4.10: Photos of the wet powder for undoped ceria a) before, and b) after the process of XRD measurement

4.2.4 XPS analysis

Table 4.2 lists the results obtained from the analysis of doped ceria nanoparticles using XPS and provides a quantitative overview of the chemical composition of each synthesized nanoparticles. As a summary, it is observed that the incorporation of dopant within ceria nanoparticles during synthesis was higher when the dopant has negative association energy. Several trends can be observed from the analysis of the data presented in the two tables; 4.1 and 4.2. Of the two oxygen vacancies generators, Nd causes a larger change in the oxygen vacancy concentration, compared to what obtained when an equal weight of Sm is added. In other words, there is a higher concentration of Ce^{+3} ions formed in the ceria doped with Nd more than the doped ceria with Sm. Ho is a much better vacancy scavenger than Er as there is more significant reduction of Ce^{+3} states in the Ho-doped ceria, based upon the increase in allowed direct bandgap and the decrease of peak fluorescence intensity with increasing dopant concentration. The relationship between conversion rate from Ce^{+4} to Ce^{+3} states, or the corresponding oxygen vacancy concentration, and the amount of dopant in the ceria nanoparticles appears to be

relatively linear when the dopant is either Nd or Sm, but is strongly nonlinear when the dopant is Ho or Er.

Weight ratios		O1s	Ce3d	Sm3d	Nd3d	Ho4d	Er4d	Molecular percentage of dopants
Undoped ceria		62.62	10.39	0	0	0	0	0
Doped with Nd	5%	65.31	11.86	0	0.29	0	0	2.45
	10%	66.03	10.70	0	0.44	0	0	4.11
	15%	65.45	10.97	0	0.96	0	0	8.75
Doped with Sm	5%	62.10	12.34	0.76	0	0	0	6.16
	10%	65.63	12.14	1.09	0	0	0	8.98
	15%	65.40	10.13	1.73	0	0	0	17.08
Doped with Ho	5%	66.68	12.03	0	0	0.38	0	3.16
	10%	67.02	8.01	0	0	1.02	0	12.6
	15%	68.30	10.99	0	0	1.44	0	13.10
Doped with Er	5%	69.77	10.61	0	0	0	0.46	4.34
	10%	60.02	14.31	0	0	0	1.34	10.68
	15%	69.36	8.17	0	0	0	1.85	22.64

Table 4.2: Chemical analysis of the atomic concentrations of synthesized nanoparticles

4.3 Mixed doped ceria (MDC) characterization

4.3.1 Absorbance dispersion and bandgap study

The direct allowed bandgap calculations, based on absorbance dispersion measurement, are done exactly as the previous procedure of single lanthanide doped ceria, but this time for mixed rare earth elements doped in ceria, which we called previously mixed doped ceria (MDC) nanoparticles. Fig. 4.11 shows the absorbance dispersions of some examples of ceria doped with two elements; one has positive association energy; Nd or Sm, and the other one has negative association energy; Ho or Er. The examined weight doping ratios are of two cases: first one is equal, which means that the reagent weight of negative association energy element used during

the synthesis procedure; *in situ*, is equal to the weight of positive association energy element, and the second doping case is double, which indicates that the weight of negative association energy element is twice the weight of positive association energy one, for more verification of the obtained results.

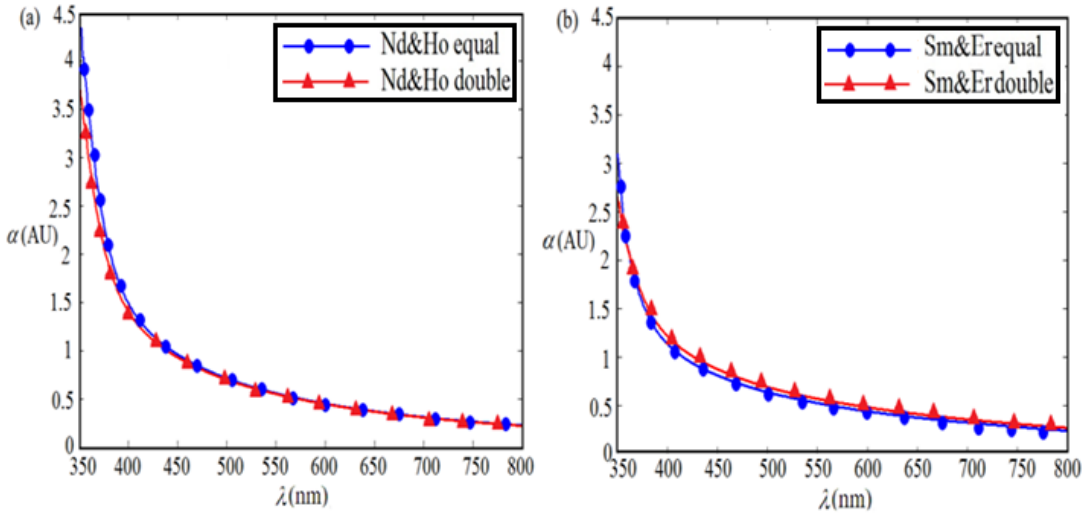

Fig. 4.11: Absorbance dispersion of ceria, doped with a) Ho and Nd and b) Sm and Er

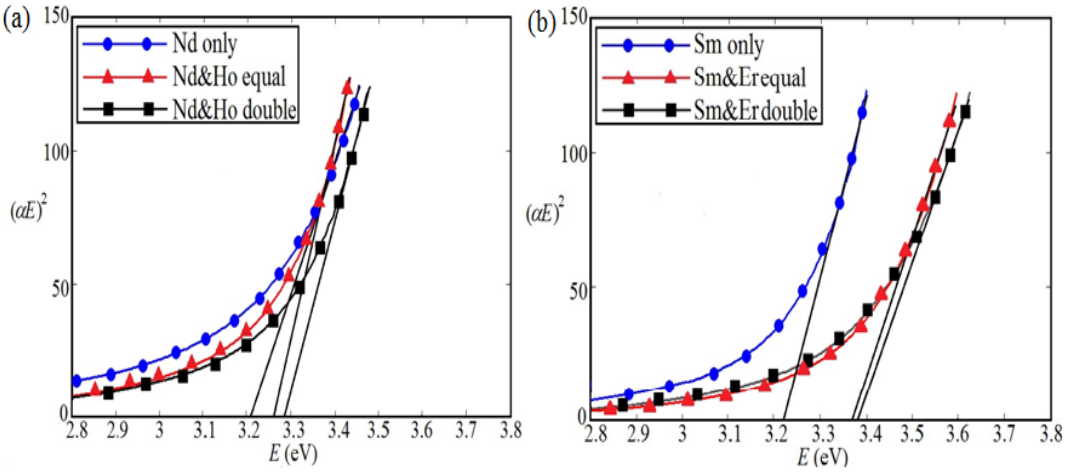

Fig. 4.12: Direct allowed bandgap calculations of ceria, doped with a) Ho and Nd and b) Sm and Er

Some examples of the direct bandgap calculation of MDC are shown in Fig. 4.12, and the results of all studied MDC samples are summarized in Table 4.3. From the direct bandgap

values, it can be noted that adding Ho or Er in addition to Nd or Sm, causes the direct bandgap to be larger than the doped ceria with only the same reagent weight ratio "10%" of Nd or Sm, respectively, which is reported in Table 4.1. This increase in the bandgap becomes higher with increasing the concentration of the negative association energy elements; Ho or Er. That gives an indication that there are less formed O-vacancies and, therefore, less Ce^{+4} ions are converted to Ce^{+3} ones. In other words, these doping materials; Ho and Er, are proved for the second time to act as O-vacancies scavengers.

4.3.2 Fluorescence emissions spectra

The fluorescent emissions of mixed doped ceria are shown in Fig. 4.13and the complete peak emission values are reported in Table 4.3. The peak emission is found to be lower within adding Ho or Er with Nd or Sm; compared to the doped ceria with only Nd or Sm, which ensures that there are less Ce^{+3} ions and O-vacancies. Given that the higher fluorescence indicates that there is a higher concentration of Ce^{+3} states associated to more formed O-vacancies and vice versa. Then, this is another proof that the negative association lanthanides act as O-vacancies scavengers in ceria. This conclusion is in a good agreement within the results obtained from the direct bandgap calculations.

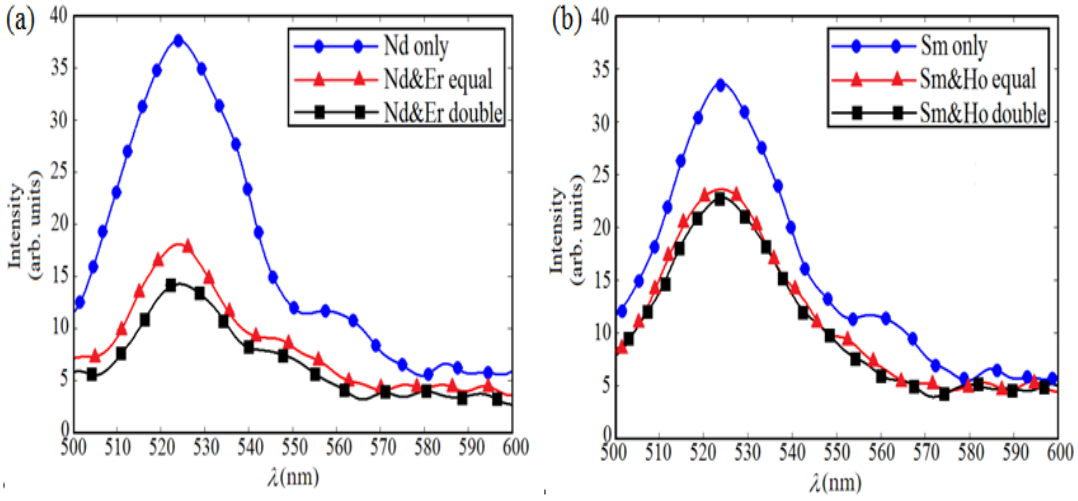

Fig. 4.13: Fluorescence emission of ceria, doped with a) Er and Nd and b) Ho and Sm

4.3.3 Results of structural analysis

To discuss the structural characteristics of the synthesized mixed doped ceria, TEM images of some MDC nanoparticles, associated with its diffraction rings, are shown in Fig. 4.14. The average nanoparticles' size, interplanar distances and lattice parameters of all MDC samples are calculated and reported in Table 4.3. From these results, it can be observed that the particle size becomes larger and the interplanar distance or lattice parameter are decreased within MDC, compared with ceria co-doped with only positive lanthanides. That interprets the fact that the O-vacancies associated to Ce^{+3} ions are decreased with adding negative E_{ass} lanthanides. That ensures the conclusion derived from both bandgap calculation and fluorescence spectroscopy.

XRD patterns of some MDC samples are presented in Fig. 4.15. Again, from the first pattern peak, the average particles' diameter can be calculated through Scherrer's formula shown in Equation (2.9) and summarized in Table 4.3. The results of XRD are in a good agreement with TEM measurements.

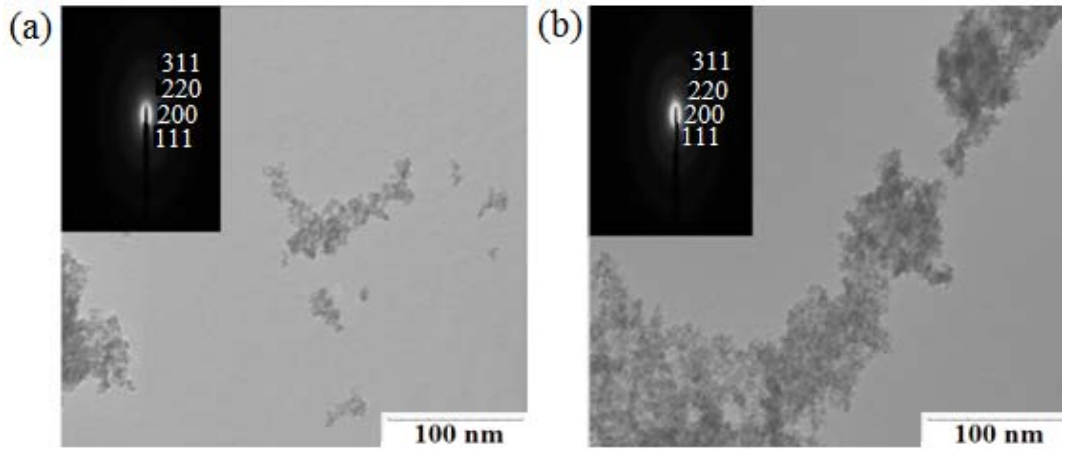

Fig. 4.14: TEM images of ceria nanoparticles doped with equal concentrations of a) Nd and Er and b) Sm and Ho

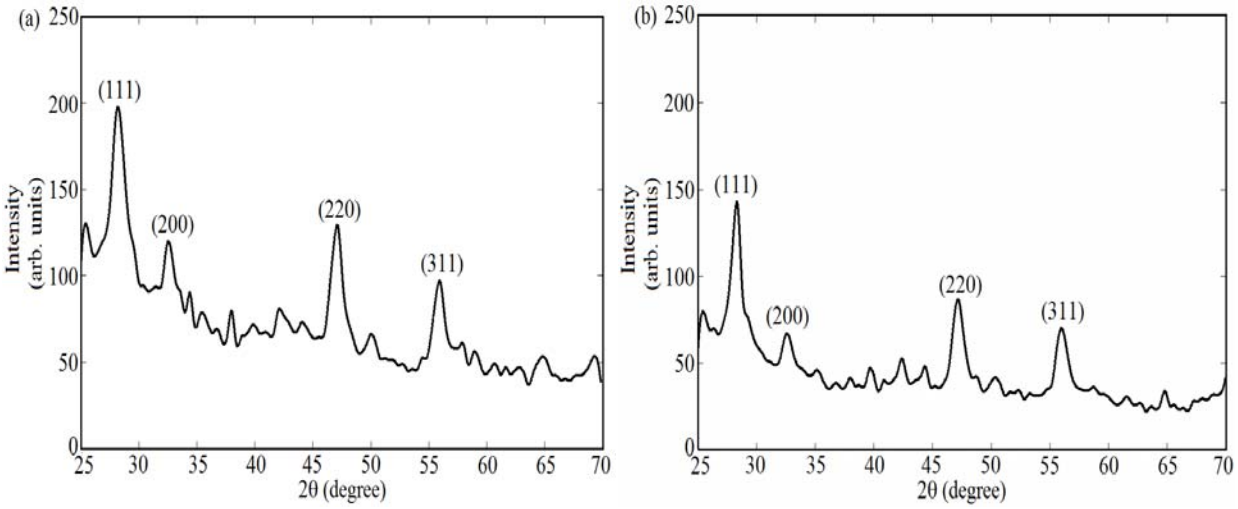

Fig. 4.15: XRD pattern of some ceria nanoparticles doped with equal concentrations of a) Nd and Ho, and b) Sm and Er

It can be concluded from the previous results, obtained from the previous optical and structural characteristics, that Ho and Er can act as O-vacancies scavengers in the doped ceria. This conclusion reaffirms the same conclusion drawn from the data presented within single dopant ceria. Also, this conclusion can be utilized in the search to control the concentration of O-vacancies formed in ceria. This study is important for two reasons: firstly, to verify the conclusions obtained from the study of the O-vacancies scavenging of the single negative association lanthanide dopant when added into ceria nanoparticles. Secondly, MDC offers a

technique to control the O-vacancies defects formed in ceria nanoparticles which can be helpful within some applications sensitive to the material's defects such as high K-dielectrics for high speed MOSFETs, in which ceria films are deposited on germanium [10-58]. This application will be presented briefly in the future work; Chapter 7.

The used dopants within ceria		Direct Eg (eV)	Peak fluorescent Intensity (arb. units)	Lattice parameter (Å)	Inter-planar distance (Å)	Mean particle size with TEM (nm)	Mean particle size with XRD (nm)
Nd	with no Ho or Er	3.21	35.68	5.35	3.07	6.39	6.45
	equal weight of Ho	3.27	19.25	5.14	2.97	6.48	6.56
	double weight of Ho	3.29	14.50	5.05	2.92	6.72	6.83
	equal weight of Er	3.28	15.95	5.32	3.07	6.60	6.55
	double weight of Er	3.29	12.00	5.28	3.05	6.69	6.83
Sm	with no Ho or Er	3.22	28.15	5.31	3.09	6.23	6.29
	equal weight of Ho	3.29	18.90	5.14	2.97	6.39	6.30
	double weight of Ho	3.31	18.05	5.11	2.95	6.60	6.55
	equal weight of Er	3.37	13.85	5.07	2.90	6.60	6.31
	double weight of Er	3.38	11.50	5.02	2.87	6.72	6.56

Table 4.3: The complete measured data for MDC nanoparticles

4.4 Doping ceria with some tri-valent metals

4.4.1 Absorbance dispersion and direct allowed bandgap

In this section, the absorbance dispersion and the direct bandgap calculations are operated for ceria initially doped with reagent weight ratios of 5%, 10% and 15% of aluminum and iron. These curves are shown in Figs. 4.16 and 4.17. It is found that the direct bandgap for both materials are less than that of the undoped ceria. This reduction in bandgap arises by increasing the doping ratio. For each doping ratio, aluminum gives lower bandgap than doping with iron.

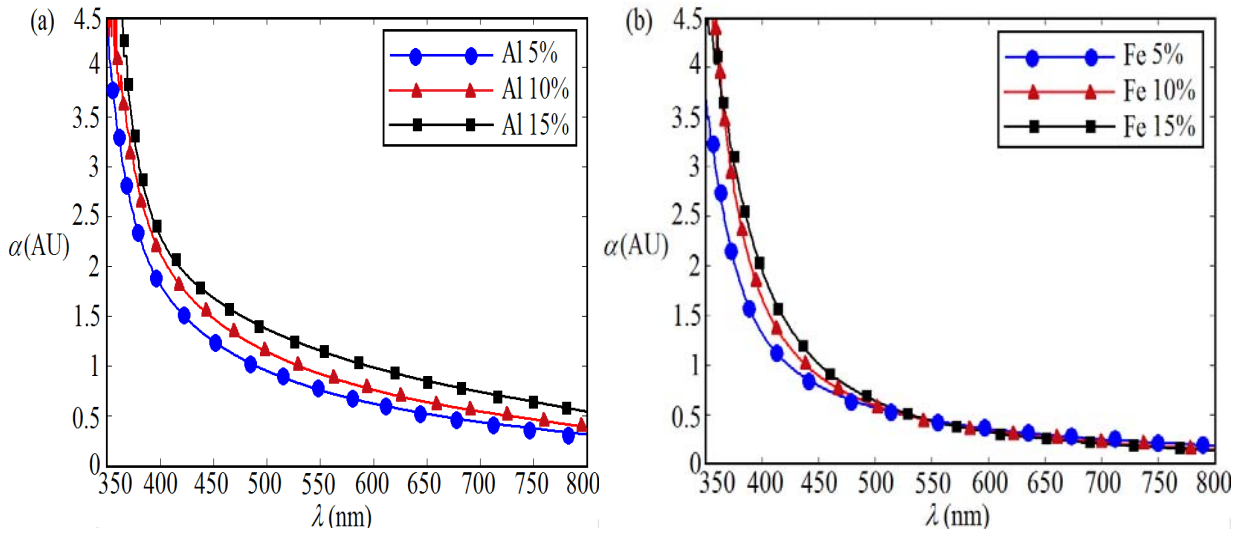

Fig. 4.16: Absorbance dispersion of ceria doped with a) Al and b) Fe

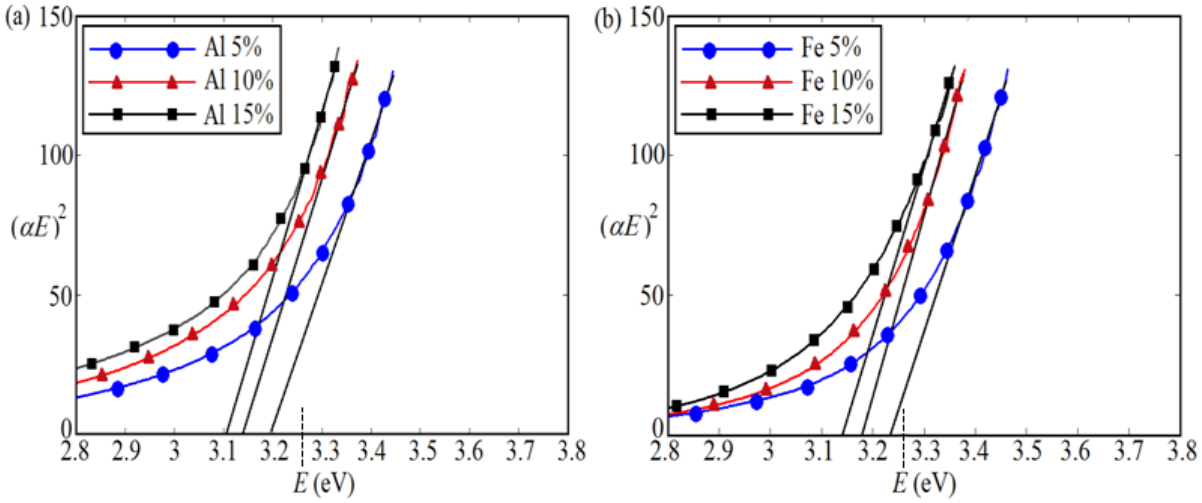

Fig. 4.17: Direct allowed bandgap calculations of ceria doped with a) Al and b) Fe "dotted line is the bandgap of undoped ceria"

4.4.2 Fluorescence emissions results

The measured emitted fluorescence spectra for both doping elements are shown in Fig. 4.18. The emitted intensity peak is increased with increasing the doping concentration and the results for aluminum are higher than that of iron.

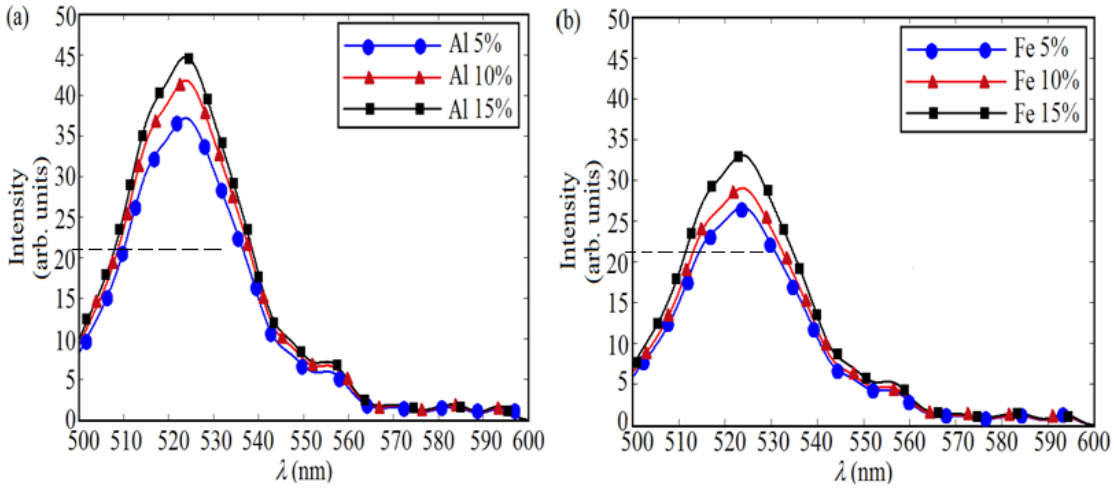

Fig. 4.18: Fluorescence emission of ceria doped with a) Al and b) Fe "dotted line is the fluorescence peak of undoped ceria"

4.4.3 Analysis of structural parameters

TEM images and XRD patterns of some ceria samples doped with both metals are shown in Figs. 4.19 and 4.20. The size of the nanoparticles is reduced with increasing the doping concentration within both dopants. The size within Al doping is smaller than Fe. The results of direct bandgap values, fluorescence intensities' peaks, particle size from TEM and XRD, lattice parameters, and interplanar distance for doped ceria with Al and Fe are summarized in Table 4.4.

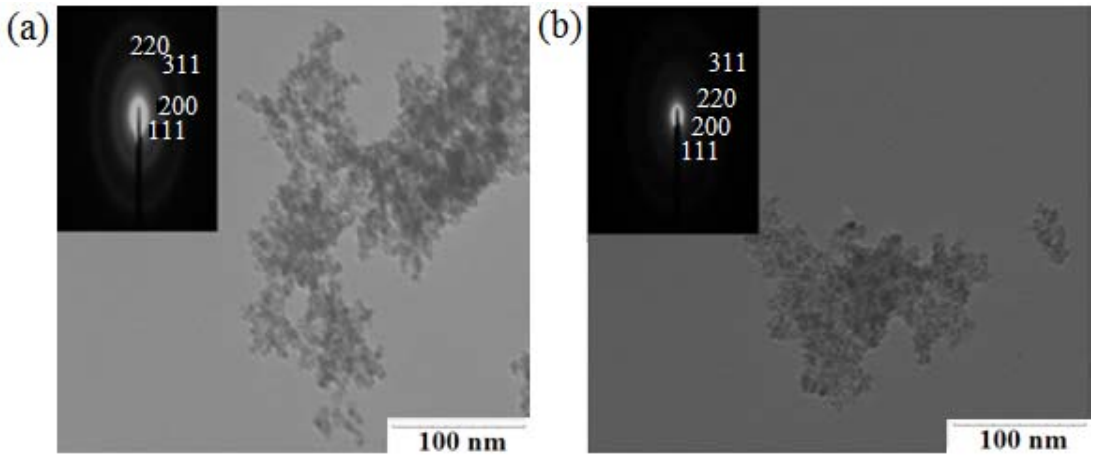

Fig. 4.19: TEM images of ceria nanoparticles doped with 5% reagent weight of a) Al and b) Fe

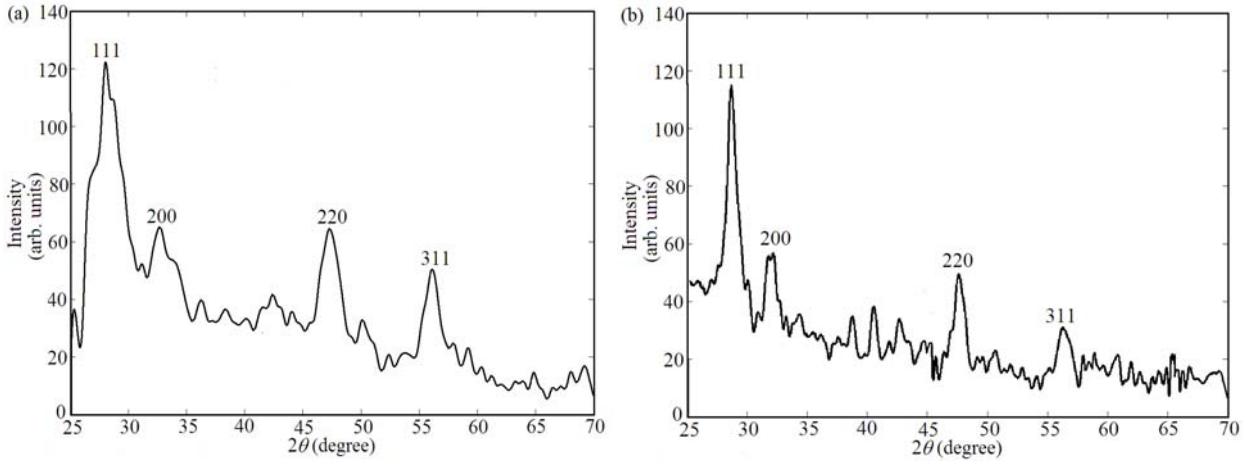

Fig. 4.20: XRD pattern of ceria doped with 5% reagent weight of a) Al and b) Fe

By comparing the results in Table 4.4 to the results of the doped ceria with Nd and Sm reported in Table 4.1, it can be concluded that doping with Al gives the highest concentration of O-vacancies formed in ceria nanoparticles or it gives the highest conversion from Ce^{+4} to Ce^{+3}. That is because the doped ceria with Al leads to the lowest direct bandgap, the highest emitted fluorescent intensity, the smallest average size of nanoparticles measured through TEM and XRD.

Material		Direct Eg (eV)	Peak fluorescence (arb. units)	Lattice parameter (Å)	Inter-planar distance (Å)	Mean particle size using TEM (nm)	Mean particle size using XRD (nm)
Doping with Al	5%	3.20	37.40	5.53	3.19	6.05	5.85
	10%	3.13	41.75	5.60	3.24	5.60	5.46
	15%	3.10	44.90	5.68	3.28	4.95	5.25
Doping with Fe	5%	3.23	26.68	5.47	3.17	6.10	6.26
	10%	3.18	29.13	5.59	3.23	5.77	5.90
	15%	3.14	33.00	5.67	3.27	5.36	5.65

Table 4.4: The complete data measured for doped ceria within Al and Fe

CHAPTER FIVE

Ceria Nanoparticles as Optical DO Sensing Material

5.1 Theory of DO sensing based on fluorescence quenching

The development of fluorescence oxygen sensing has had profound effects in the fields of medical science, bioengineering, environmental monitoring, and industrial process control, and in military applications [59]. Research to develop smaller and more accurate sensors that are robust in harsh or reactive environments continues. In biomedicine as an example, the development of a biomedically-compatible microscale dissolved oxygen (DO) sensing system, using nanotechnology methods, has been extensively pursued in recent research studies for applications that include *in vivo* and *in vitro* oxygen sensing especially prior to and during surgical procedures, such as during tumor removal operations [60]; probing the surfaces of transplant tissues and organs [61]; and monitoring blood gas levels in microdialysis units [62].

The bulk of the sensor technology falls under three classifications: fluorescence-dye optical sensing, amperometric electrochemical sensing, and thin film solid-state conductivity sensing. The last two types of sensors have severe limitations; for example, these sensors suffer from fouling by organic matter, which leads to catastrophic failure and short operational lifetimes [63]. Additionally, electrochemical sensors require a reference electrode, which had been proved to be difficult to miniaturize and the characteristic electrostatic charge of this electrode attracts charged particles and ions, causing the device to be extremely prone to contamination by organic matter [64]. It should be noted that ceria thin films are currently used as resistive oxygen sensors [65], but they have the same disadvantages as the electrochemical sensors.

The main optical phenomenon employed when sensing dissolved oxygen using fluorescent dyes is fluorescence quenching, caused by an energy transfer to the dissolved oxygen followed by the formation of non-radiative complexes, when oxygen interacts with the dye molecule. Fluorescence-quenching oxygen sensors have been adopted rapidly due to their inherent high sensitivity and stability [66]. A majority of fluorescent dyes, particularly the ones that are organometallic in nature, displays oxygen-quenching characteristics. However, a discrete set of fluorophores exhibits enhanced sensitivity to oxygen, as well as relatively long fluorescent lifetimes, thus reducing the requirements of the optical transducers [67]. Examples include some of the ruthenium-based dyes [68-69]; however, several of these dyes are sensitive to water, which negatively impacts the accuracy of the measurement of dissolved oxygen in aqueous solutions. To overcome this issue, polymers doped with fluorescent dyes have been formulated and these composites have been used as the active material in some fluorescence-based dissolved oxygen (DO) sensors [70].

Fluorescence emission decreases with increasing DO concentration in the fluorescent dye where the amplitude of the emitted fluorescence intensity is related to the DO concentration through Stern-Volmer equation, which is as follows [71]

$$\frac{I_o}{I} = 1 + K_{SV}[O_2] \tag{5.1}$$

I_o and I represent the steady-state fluorescence intensities in the absence and presence, respectively, of the quencher; oxygen; K_{SV} is the Stern–Volmer quenching constant, which is an indication for the sensitivity of the used nanoparticles to sense the dissolved oxygen [31]; and $[O_2]$ is the dissolved oxygen concentration.

The novel work introduced in this thesis is the study of ceria nanoparticles as molecular probes in the fluorescence quenching DO sensors. Based on our study of optical and structural characterization for undoped, lanthanides-doped, and metal-doped ceria nanoparticles, some selected ceria nanoparticles are evaluated as optical DO sensors. We expect that their relatively high concentration of the O-vacancies will make these particular nanoparticles efficient probes for DO sensing. The selected dopants that have been shown are previously to increase the concentration of the O-vacancies in doped ceria nanoparticles are the ones with positive association energies – two lanthanides elements, neodymium and samarium, and aluminum. Iron shows promising results in forming higher concentrations of O-vacancies in ceria based upon an analysis of the absorption spectra of the iron-doped ceria nanoparticles. However, the intensities of the fluorescence emission from the ceria nanoparticles doped with iron are found to be relatively low when compared to undoped ceria nanoparticles. So, this dopant is not selected in the study for this application.

5.2 Fluorescence quenching experimental setup

The setup designed to measure the optical fluorescence quenching in the dissolved oxygen sensing experiment is shown in Fig. 5.1. It is similar to the fluorescence setup with some modification. It consists of an ultraviolet (UV) lamp coupled to a monochromator. The light that exits the monochromator and excites the nanoparticles (λ_{exc} = 430 nm) is focused on a three-hole flask. In the flask, 0.2g of the dried powder of ceria nanoparticles, undoped or doped with one of the selected elements, is suspended in 200 mL of DI water and sonicated prior to the fluorescence measurement. This solution is stirred slowly during the experiment to prevent the photobleaching. The inlet oxygen and nitrogen gases, whose flow rates are controlled by mass flow rate controller (MKS 247-C), are flown separately through a double-hole cork placed in one

of the holes of the flask. The probe of DO meter, (Milwaukee MW600), which has a measurement range up to 19.9 mg/l, is inserted in the second hole of the flask. The third hole has a short hose attached to a cork, which acts as an outlet of the gases from the flask. The fluorescence signal is collected using a second monochromator positioned at a 90^{o} angle to the first monochromator. As the monochromator is scanned over the visible wavelength region, the fluorescence signal is detected by the photomultiplier tube, located at the exit port of the second monochromator, and is recorded using a power meter similar to what is used in the fluorescence setup.

At each change of the mass flow rate controller for both gases, we wait for the DO concentration to be stabilized, as determined as the time when a constant reading is obtained from the DO meter. Then, the UV lamp is turned on and the second monochromator is adjusted to start scanning the visible fluorescence emission spectrum. To study the temperature stability of the different ceria nanoparticles sensitivity, the 3-hole flask is immersed in a water bath on a hot stirrer and the temperature is raised up to 50^{o}C. At each temperature, the previous procedure of measuring the emitted fluorescence with changing the DO concentration is done exactly. Based on the fluorescence quenching, Stern-Volmer constants of the undoped and doped ceria are calculated at different temperatures and compared to the Stern-Volmer constants calculated at room temperatures. The percentage change of Stern-Volmer constants with the temperature can be considered a measure of the thermal stability of the sensitivities of the nanomaterials studied for DO detection.

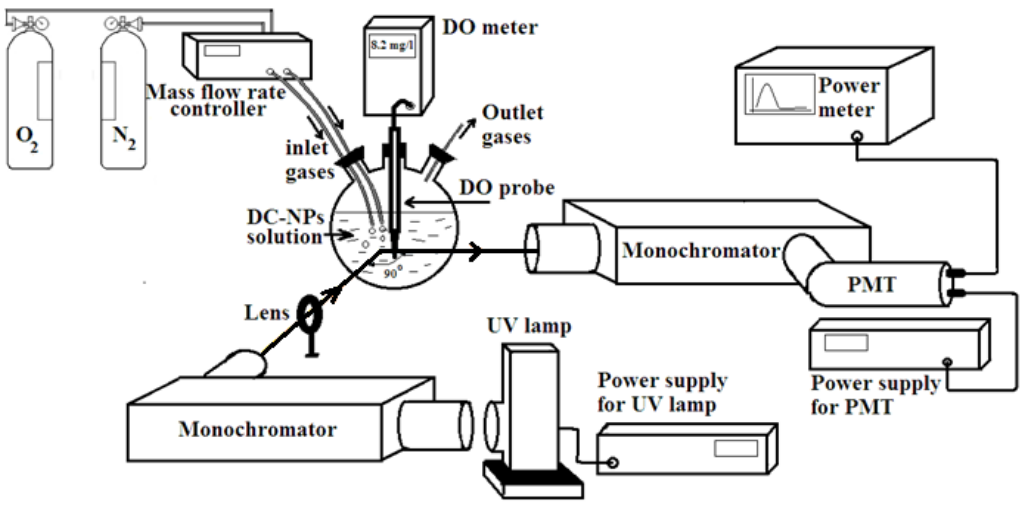

Fig. 5.1. Schematic Diagram of the fluorescence quenching DO sensing setup

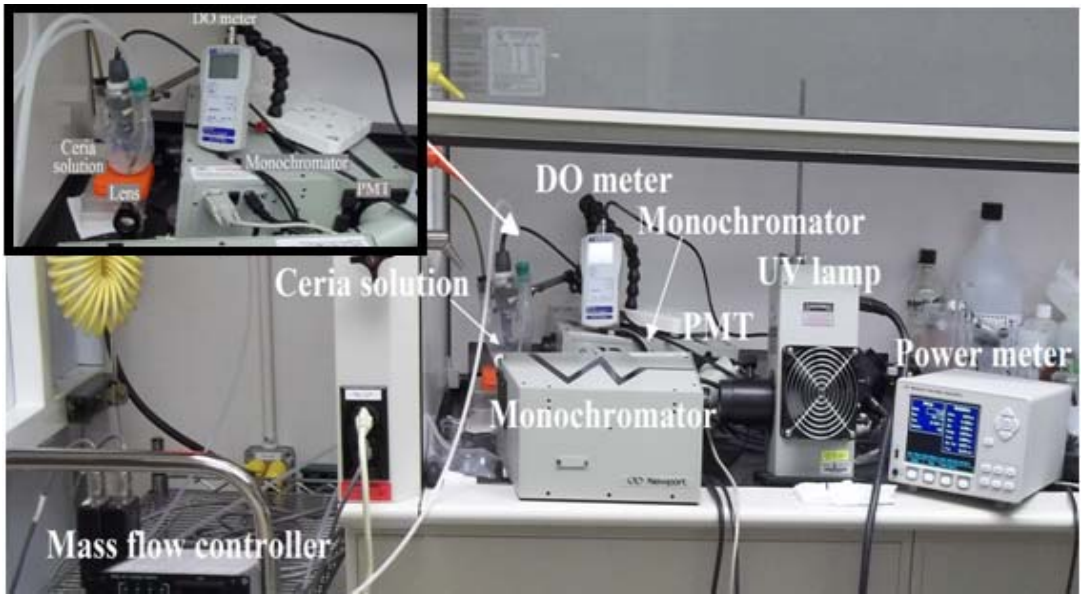

Fig. 5.2. A photo of the optical fluorescence quenching DO sensing setup

5.3 Fluorescence quenching and K_{SV} results

5.3.1 Fluorescence quenching at room temperature

Now, we introduce the results of undoped and doped ceria nanoparticles as the molecular probe in DO sensing through the fluorescence quenching technique. The fluorescence intensity

of the nanoparticles can be correlated to the ambient oxygen concentration as the radiative pathways in ceria are associated with the Ce^{+3} ions. Examples of visible fluorescence spectra at different DO concentrations are shown in Fig. 5.3. For all undoped and doped ceria nanoparticles, it can be observed that the amplitude of the emitted signal decreases as the DO concentration is increased, but the shape of the fluorescence spectra remains unchanged. In addition to the explanation described previously, in section 2.2.2, concerning the correlation between the emitted photons and the relaxation via the 5d-4f transition of an excited Ce^{+3} ions in Ce_2O_3, the Ce^{+4} ionization states have very small probability of the radiative recombination. Thus, we hypothesize that the interaction of the dissolved oxygen molecules with ceria nanoparticles suppresses the O-vacancy concentration and forces a conversion of some of the cerium from Ce^{+3} to Ce^{+4}.

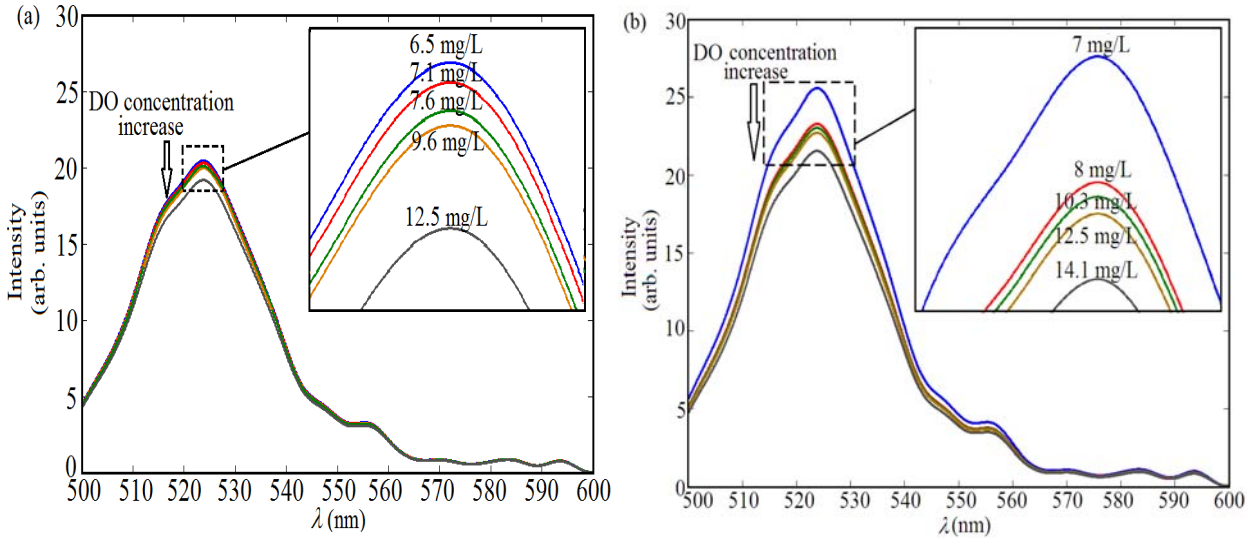

Fig. 5.3: Fluorescence quenching spectra at room temperature with different DO concentrations for a) undoped ceria and b) doped ceria with 5% reagent weight of Sm as an example.

The linear interpolation between I_o/I versus DO concentration for some of the doped ceria nanoparticles are presented in Fig. 5.4. There are two points about the graph that must be discussed, which are the error bars and the value of I_o. The origin of the error bars in the graph is as follows: during the detection of the emitted fluorescence at each stabilized DO concentration, the second monochromator is adjusted at the wavelength of peak intensity, 523 nm, and the power meter records the maximum amplitude for 5 seconds. Then, the mean value of the maximum amplitudes obtained during this time period is calculated and the error bars shown in Fig. 5.4 represents the minimum and maximum amplitudes of the peak fluorescence intensity around the mean value. Secondly, the value of I_o could not be found experimentally as the DO concentration never reached zero even when there was no inlet flow of oxygen or nitrogen. We speculate that this is due to a release of oxygen stored in the ceria lattice when the nanoparticles are introduced into the solution. Therefore, I_o is calculated by forcing the linear fit of the data to include a point for $I_o/I = 1$ when DO = 0 mg/L.

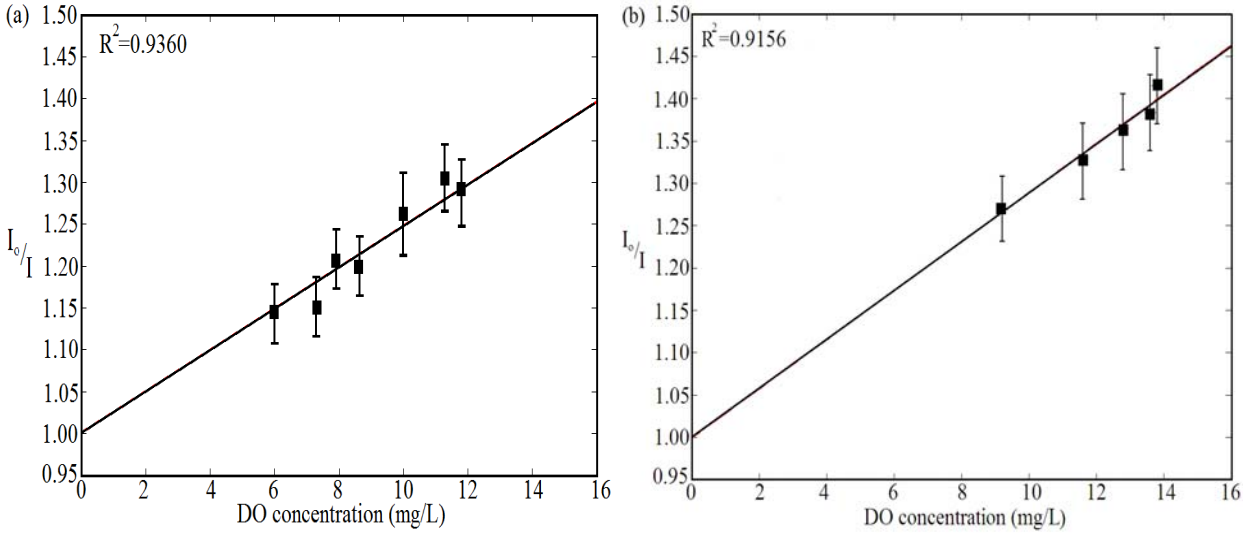

Fig. 5.4: Stern-Volmer relations at room temperature for ceria doped with 5% reagent weight ratio of a) Nd and b) Al

The complete values of K_{SV} for the different synthesized ceria nanoparticles at room temperature are summarized in Table 5.1. The dopants selected for this study are found to increase K_{SV} of the doped nanoparticles as compared to the K_{SV} of the undoped ceria. Aluminum-doped ceria shows a higher sensitivity than the lanthanide dopants studied. This result supports the hypothesis that the sensitivity of the ceria nanoparticles to DO is correlated to the initial O-vacancy concentration as the aluminum-doped ceria has the highest concentration of mobile O-vacancies, which is proven during the characterization of aluminum-doped ceria (ceria: Al) that is presented in Chapter 4. In the case of lanthanide dopants, K_{SV} of ceria nanoparticles doped with neodymium (ceria: Nd) is higher than samarium doped ceria (ceria: Sm). This can be explained through the conclusions derived from the optical and structural properties of both materials, as described in Chapter 4, that neodymium generates more active O-vacancies in the doped ceria nanoparticles than samarium.

Material	K_{SV} (M^{-1})
Undoped ceria	184.6
ceria:Sm	369.6
ceria:Nd	393.6
ceria:Al	454.4

Table 5.1: Stern-Volmer constants of undoped and doped ceria nanoparticles

Overall, the calculated values of Stern-Volmer constants show that our synthesized doped ceria nanoparticles are promising molecular probes in optical DO sensors as the K_{SV} for these nanoparticles are much higher than the same constant for undoped ceria, measured with the same procedure, and two fluorescent dyes that are used to detect dissolved oxygen: PtOEP, which has a K_{SV} in the range of 1.4 to 50 M^{-1} [72-73], and tris(2,2A-bipyridyl) dichlororuthenium(II) hexahydrate , which has a K_{SV} in the of range 115-283 M^{-1}[65-74].

It is also important to note that the size of our synthesized nanoparticles as DO sensing molecular probes are much smaller than the nanostructured fluorophores presently used in DO optical sensing by the fluorescence quenching technique, which is of interest for certain applications such as intracellular monitoring of oxygen. The undoped and doped ceria nanoparticles used in the present study on DO sensing have an average diameter between 5.05-6.75 nm, as measured from the TEM micrographs, and do not require an encapsulant when used in aqueous media. The diameters of the ceria nanoparticles are much smaller than most of the fluorescent dyes presently used in optical DO sensing. For example, Ru(II) tris(4,7 diphenyl-1,10-phenanthroline) dichloride/silica has a size ranging from 20 to 300nm and Pt(II) octaethylporphine embedded in xerogel is between 120-250 nm [75-76].

5.3.2 Thermal stability of K_{SV}

Due to its importance, the thermal stability of the Stern-Volmer constants of the synthesized undoped and doped ceria nanoparticles is studied at temperatures from room temperature up to 50^{o}C. Firstly, the fluorescence spectrum of undoped and doped ceria nanoparticles (ceria: Nd, ceria: Sm and ceria: Al) are measured at different temperatures with the same DO concentration in the solution; the spectra from the ceria doped with Nd and Sm as examples are shown in Fig. 5.5. At constant DO concentration, all of the undoped and doped ceria nanoparticles show a decrease in the amplitude of emitted spectrum peaks with increasing the temperature. This is due to the impact of the temperature rise on conversion of cerium from Ce^{+3} ionization state to Ce^{+4} state with a corresponding elimination of some of the O-vacancies [53]. The impact of temperature on the Stern-Volmer graphs for the some of the doped ceria nanoparticles are shown in Fig. 5.6. The values for K_{SV} calculated using the spectra collected at

different temperatures for all of undoped and doped ceria nanoparticles studied during this experiment are summarized in Table 5.2.

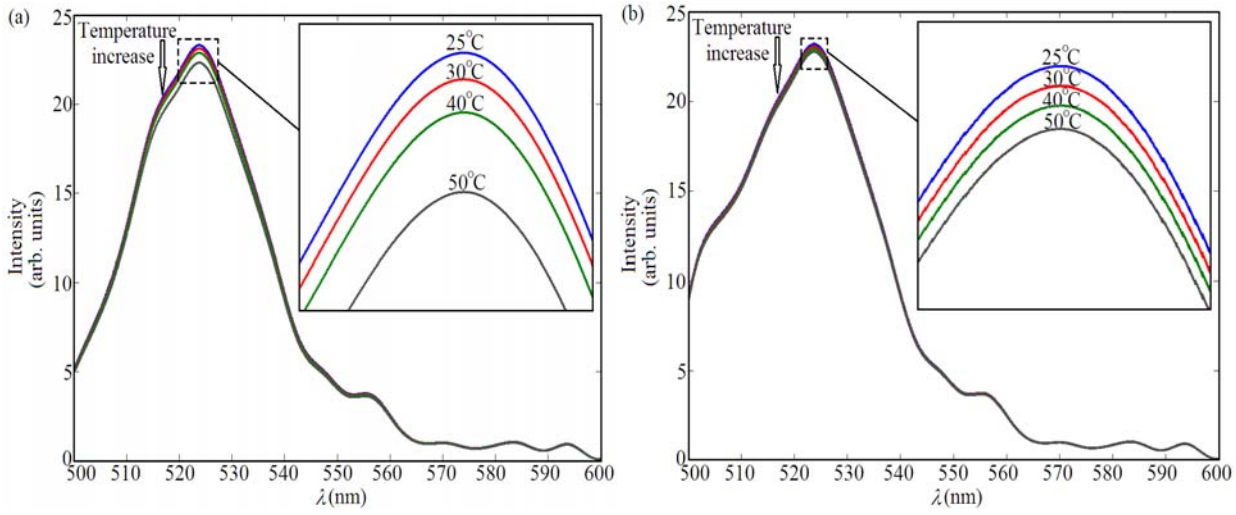

Fig. 5.5: Fluorescence spectra, demonstrating fluorescence quenching, at a constant dissolved oxygen concentration, DO = 10.3 mg/L, for ceria doped with a) Sm, and b) Nd at 25, 30, 40, and 50°C

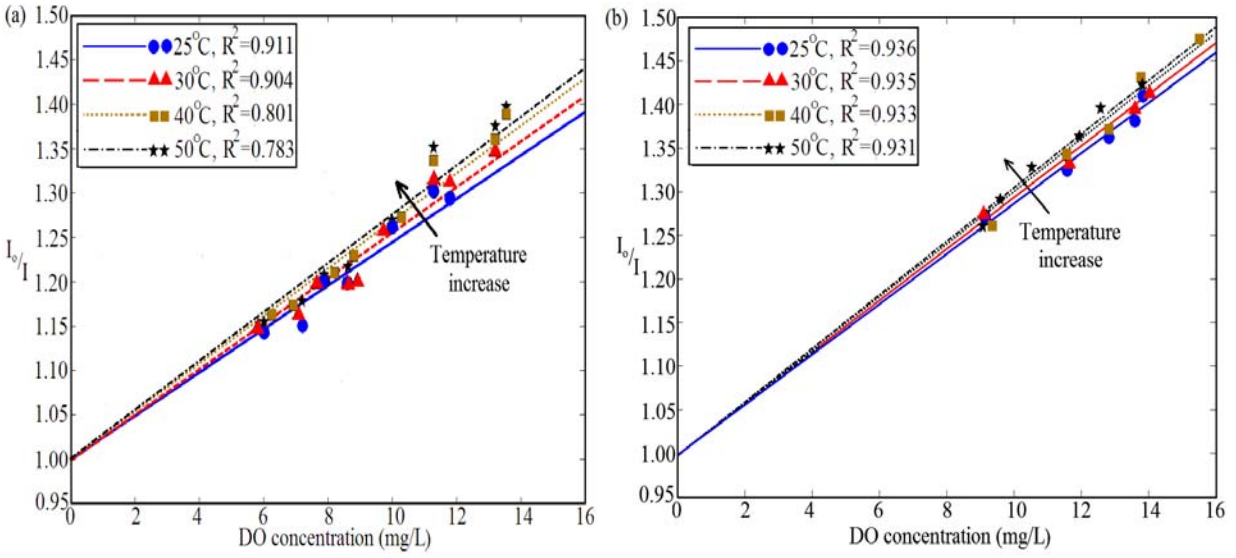

Fig. 5.6: The linear relationship between I_o/I versus DO concentration at 25, 30, 40, and 50°C, for doped ceria with a) Sm and b) Al

Material		K_{SV} (M^{-1})						
		25°C	30°C	% Change	40°C	% Change	50°C	% Change
Undoped ceria		184.6	190.0	2.93	201.6	9.21	208.0	12.68
Doped ceria with	Sm	369.6	385.6	4.33	422.4	14.29	465.6	25.95
	Nd	393.6	409.6	4.07	430.4	9.35	440.1	11.81
	Al	454.6	468.0	2.95	481.0	5.81	489.6	7.69

Table 5.2: K_{SV} values for undoped and doped ceria nanoparticles at different temperatures

It can be observed that the sensitivity to DO for all the studied ceria nanoparticles increases with increasing temperature. Stokes-Einstein relation states that there is a direct relation between temperature and Browning motion of the nanoparticles in the colloidal solution, which also contributed to an increase in Stern-Volmer constant because of an increase in the number of collisions between the nanoparticles and the dissolved oxygen molecules as a function of time [77]. However, the effect should be relatively independent on whether the ceria is undoped or doped since the both cases have approximately the same diameter. Therefore, we propose that this trend is due to the increase of the O-vacancies mobility and, consequently, the ionic conductivity [78] rather than an increase in the concentration of O-vacancies. To prove that, the lanthanide dopants are discussed as examples. Neodymium dopant is proved, in Chapter 4, to form more O-vacancies than samarium dopant. However, the percentage change of the sensitivity, relative to the room temperature value, is found to be increased more rapidly for the ceria doped with samarium as compared with that of ceria-doped with neodymium. The activation energy of the O-vacancies in ceria doped with samarium, 0.76 eV, is lower than the neodymium doped ceria nanoparticles, 0.79 eV [27]. Therefore, the mobility and ionic conductivity of O-vacancies in Sm-doped ceria are higher in the Nd-doped nanoparticles, which lead to larger change in K_{SV} with temperature when the dopant is samarium dopant more than the

neodymium dopant. Then, the ionic conductivity is the dominant factor over than O-vacancies concentration to explain the variation in Stern-Volmer constants with temperature increase. From Table 5.2, the percentage change of the sensitivity, relative to the room temperature value, is reasonably small, with the smallest change found for ceria doped with aluminum compared to undoped ceria and either Sm- or Nd-doped ceria. This means that aluminum dopant offers the best thermal stability of the DO sensitivity for ceria nanoparticles compared to the undoped ceria and the lanthanide-doped ceria studied. Within lanthanide dopants, K_{SV} of ceria doped with neodymium is more stable with respect to temperature than the samarium-doped ceria nanoparticles.

Generally, all of the ceria nanoparticles studied in this work, the undoped ceria, ceria:Sm, ceria: Nd, and ceria: Al, shows much better thermal stability of DO sensitivity than other presently used fluorescent dyes For example, PtTFPP-doped TEOS/Octyl-triEOS has relative change of K_{SV} at 46^{o}C by 73% compared to the value of the constant at room temperature and Alq3/PtOEP has a relative change in K_{SV} of 54% when the temperature is increased from room temperature to 60^{o}C [79-80].

As a summary, the ceria nanoparticles doped with positive association energy lanthanides, samarium and neodymium, or with aluminum, can be considered robust molecular probes for DO sensing using the optical fluorescence quenching technique. Aluminum-doped ceria shows the highest sensitivity and has the best thermal stability of K_{SV} compared to the ceria doped with either of the lanthanide elements. We expect that the use of these nanoparticles as the molecular probes can lead to a significant improvement in DO sensors for industrial and environmental monitoring applications. However, aluminum-doped ceria nanoparticles may not be the best choice in biomedical applications due to the cytotoxicity behavior of aluminum [81]

although this may be offset by the free radical scavenging of ceria [7]. Toxicology studies must be performed with Al-doped ceria to determine whether this is a concern. In the meantime, the results obtained on the undoped and ceria doped with samarium or neodymium show that these nanoparticles hold significant promise as multi-function nanomaterials for biomedical applications that include DO sensing. Finally, all of the undoped and doped ceria nanoparticles studied in this work have higher Stern-Volmer constants and better thermal stability of the sensitivity for DO sensing when compared to the properties of many fluorescent dyes presently used in the field of optical DO sensing and the ceria nanoparticles have a much smaller size than most of the fluorescent molecular probes.

CHAPTER SIX

Doped Ceria Nanoparticles as Up-conversion Media

6.1 Theory of up-conversion

In an up-conversion (UC) process, two (or more) low-energy photons, depending on the material, from excitation source are converted into one photon with higher energy that, ideally, equals the sum of the low-energy photons. The integrated up-converted luminescence intensity (I) is a function of the pumping power (P), as follows [82]

$$I \propto P^n \tag{5.1}$$

where n is the number of pump photons absorbed per up-converted photon emitted. The exponent n can be approximately 2 or 3, which indicates two-photon or three-photon absorption processes, respectively. The up-conversion process is used in a variety of research fields. In lasers, one of the applications of up-conversion materials is in the area of solid-state compact lasers, such as Er^{+3} doped fluoride crystals which emits bright green emission at room temperature when illuminated with near-infrared (NIR) photons [83-84]. In bioimaging, up-conversion of photons from the infrared (IR) to visible wavelength range is preferred to down-conversion from UV to visible light because of the transparency of tissue in large regions of the infrared wavelength range and the strong absorption by proteins and waters in the UV wavelength region along with reasonably efficient fluorescence in the blue-to-green wavelengths by the protein molecules optically excited by UV light [85]. Furthermore, the excitation of traditional biolabels with UV or short -wavelength radiation results in serious possible damage or even death of biomolecules caused by long-term irradiation [86]. In solar cells, the use of up-converting materials is important in the photovoltaic industry for the development of high-

efficiency solar cells [87]. As the largest losses in the traditional silicon solar cells are the non-absorbed photons at energies below the bandgap of the silicon semiconductor, which do not contribute to energy conversion and the high energy photons that create electron-hole pairs in silicon near the surface, where surface recombination and low mobility reduce the likelihood that the carriers will contributed to the optically-generated current. So, the efficiency of solar cells can be improved by combining luminescent up-conversion and down-conversion layers [88].

Before we discuss the different mechanisms of up-conversion, we will give a brief review about the electronic structure of lanthanides and energy levels, which are important in understanding the up-conversion energy mechanisms of our doped ceria nanoparticles. The neutral lanthanide atoms mostly have three outer electrons ($6s^2 5d^1$) and a number of 4*f* electrons varying from 0 to 14. Lanthanides are commonly found in their ionized trivalent state, having lost their loosely bound 5*d* and 6*s* electrons. The electrons of the partially filled 4*f* shell are shielded from interactions with external forces by the overlying $5s^2$ and $5p^6$ shells; therefore, the transitions involved in the up-conversion processes in the trivalent lanthanides are 4*f*-4*f* transitions [89].

When the lanthanide ions are doped in a solid matrix, the 4f electrons levels become non-degenerate because of Coulombic, spin-orbit and crystal-field interactions, as shown in Fig. 6.1. Coulombic (or electrostatic) interactions arise from the existence of repulsions between the 4*f* electrons of the lanthanide ion considered. This results in a splitting of the free-ion levels into ^{2S+1}L energy levels, which are each $(2L + 1)(2S + 1)$-fold degenerate, where L and S are the quantum numbers associated with the total orbital angular momentum and the total spin momentum, respectively. The electrostatic energy splitting of the ^{2S+1}L terms is typically around 10^4 cm^{-1}. Spin-orbit interactions, which is caused by the interaction between the electron spin and

the magnetic field created by the electron's motion, split each ^{2S+1}L term into $(2J + 1)$ states denoted $^{2S+1}L_J$, where J is the quantum number associated with the total angular momentum, of range $(|L - S| \leq J \leq |L + S|)$. The splitting of $^{2S+1}L_J$ terms is on the order of 10^3 cm^{-1}. Finally, the interaction of the 4*f* electrons with the crystal field results in a Stark splitting of the $^{2S+1}L_J$ terms into $(2J + 1)$ terms which are called $^{2S+1}L_{J,\mu}$. This type of splitting is relatively small, on the order of 10^2 cm^{-1}, due to the shielded property of the electrons in the 4*f* shell. Then, the 4*f*-4*f* transition energies are relatively invariant for a given ion in different host lattices because of the shielding from the matrix provided by the $5s^2$ and $5p^6$ shells [90-91].

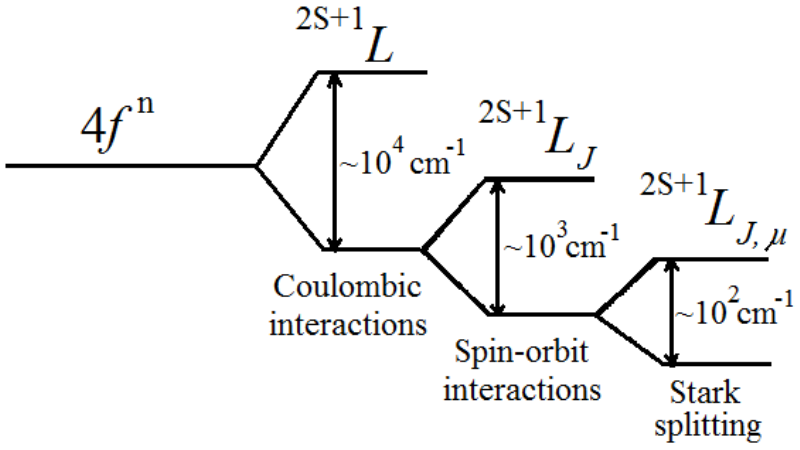

Fig. 6.1: 4f free-ion degeneracy of the lanthanides

The characteristic $^{2S+1}L_J$ energy levels of lanthanide ions led to Dieke diagram [92], as shown in Fig. 6.2. The transitions between the $^{2S+1}L_J$ energy levels becomes the basic principle of the up-conversion process through optical excitations and emissions over a wide band of spectrum from visible to far IR region and can extend to VUV region [93-94].

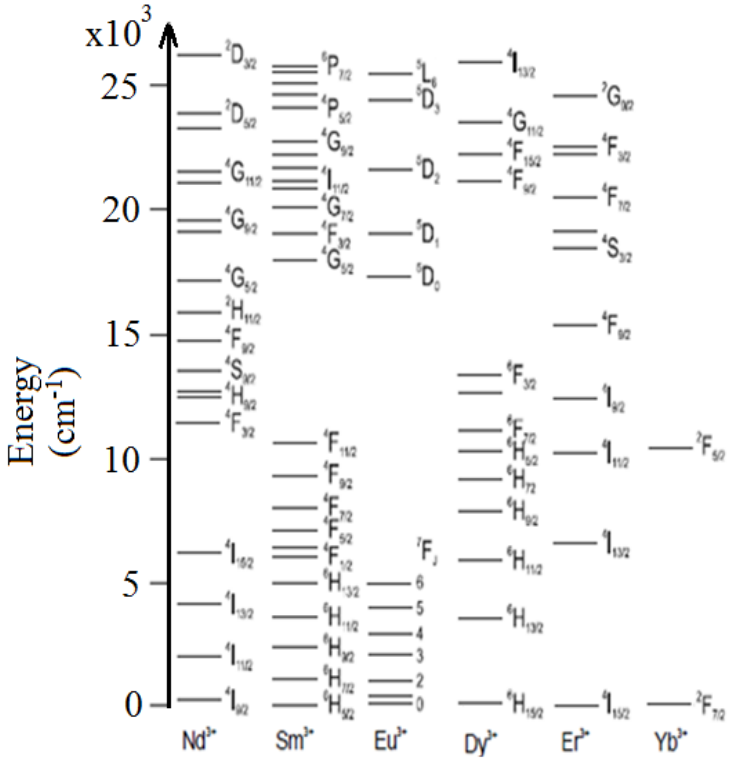

Fig. 6.2: Dieke diagram: energy levels of the $^{2S+1}L_J$ of some trivalent lanthanide ions

The dominant mechanisms of the up-conversion property are excited state absorption (ESA) and energy transfer (ET). ESA mechanism, also known as sequential two-photon absorption or ground state absorption (GSA), involves the successive absorption of photons via a single ion. The general energy scheme of ESA is shown in Fig. 6.3.a, in which the first photon causes an ion from the ground state (state 1) to enter a long-lived intermediate excited state (state 2). Then, a second photon promotes this ion from state 2 to the higher excited state (state 3), which relaxes radiatively and results in UC emission. In ET mechanism (shown in Fig. 6.3b), UC between excited ions proceeds from a sequential absorption of two photons that transfer energy from an excited ion (donor) to another neighboring ion (acceptor). The excited acceptor relaxes radiatively, to release the UC photon. ET is observed in materials with high dopant ion concentrations [95].

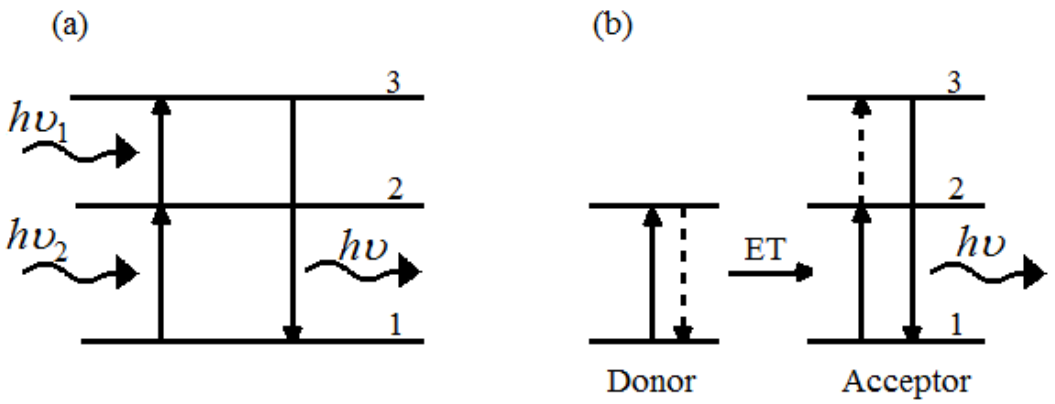

Fig. 6.3: Schematic diagrams of a) ESA and b) ET processes ($h\upsilon$ is the photon energy)

Rare earth ions can be considered famous luminescent centers due to their metastable energy levels and relatively long emission lifetimes [86]. Trivalent rare earth ions such as Er^{+3}, Tm^{+3}, Ho^{+3} and Yb^{+3} are examples of the used rare earth luminescent materials. Among these rare earth ions, the Er^{+3} ion is one of the most efficient ions for up-conversion because of the metastable levels $4I_{9/2}$ and $4I_{11/2}$ of Er^{+3} which can be easily populated by commercial low cost high-power light emitting diodes or laser diodes operating in IR region around 800 and 980 nm [33]. Ceria is a promising host material for up-conversion because of its good thermal stability and relatively low phonon cutoff energy [96]. This second property decreases the possibility of non-radiative transitions, which can reduce the quantum yield for the up-conversion process. Therefore, our work concentrates on ceria nanoparticles doped with erbium as the up-conversion media. Also, this work introduces the results from a study of how to improve the up-conversion process with adding other lanthanide dopants to ceria:Er nanoparticles, such as neodymium and samarium (Nd-ceria:Er and Sm-ceria:Er). This study is the first work, to the best of our knowledge, on the up-conversion process for ceria:Er, synthesized by chemical precipitation, where additional lanthanide dopants, Nd or Sm, are used to improve the up-converted efficiency by altering the concentration of a defect, the O-vacancy, in the host matrix.

6.2 Experimental procedure to measure up-converted emissions

For the up-conversion process, an experiment that has been conducted to detect the existence of up-conversion in ceria doped with erbium only and erbium mixed with some positive association lanthanide elements, such as samarium and neodymium, to determine the impact of the concentration of O-vacancies on the up-conversion emission. These doped ceria nanoparticles are synthesized exactly as the procedure mentioned in Chapter 3. After the 24 hours synthesis process, these samples are calcinated at temperatures up to 900^{o}C for one hour in an oxidation furnace in which the inlet gas is nitrogen and no oxygen is allowed to be entered. The up-converted emission from the calcinated nanoparticles are compared to the as-synthesized samples, i.e., that have not gone through calcination. The absorbance spectrum of one calcinated ceria:Er sample is measured using a Hach DR/4000V spectrophotometer to determine the energy levels that can be used as excitation wavelengths. To detect the up-conversion spectrum, the experimental set-up is as follows: an IR laser module with a central wavelength of 780 nm is focused on to a cuvette containing a colloidal sample of ceria nanoparticles. The upconversion signal is collected from the cuvette and directed into a monochromator that is positioned at a 90^{o} to the IR laser. As with the fluorescence setup described in Chapter 3 and shown in Fig. 3.2, a photomultiplier tube connected to a Newport power meter is used to detect the upconverted optical signal from the monochromater which is scanning between 500 nm and 700nm.

6.3 Experimental results of up-conversion

6.3.1 Absorbance spectrum of ceria:Er

Firstly, the absorbance spectra of ceria doped with erbium, for both non-calcinated and calcinated conditions, are shown in Fig. 6.4. For the non-calcinated samples, there is no

absorbance peak over the spectrum range. However, it can be observed that there are different absorbance peaks related to the energy levels of erbium, shown previously in Dieke diagram, for the ceria:Er sample that was calcinated at 900°C for one hour. Thus, Fig. 6.4 shows the importance of the calcination, or annealing step, to form the energy levels of erbium required for up-conversion process. This conclusion is in a good agreement with other research work, which show that the calcination step is required to form the energy levels for up-conversion process [97].

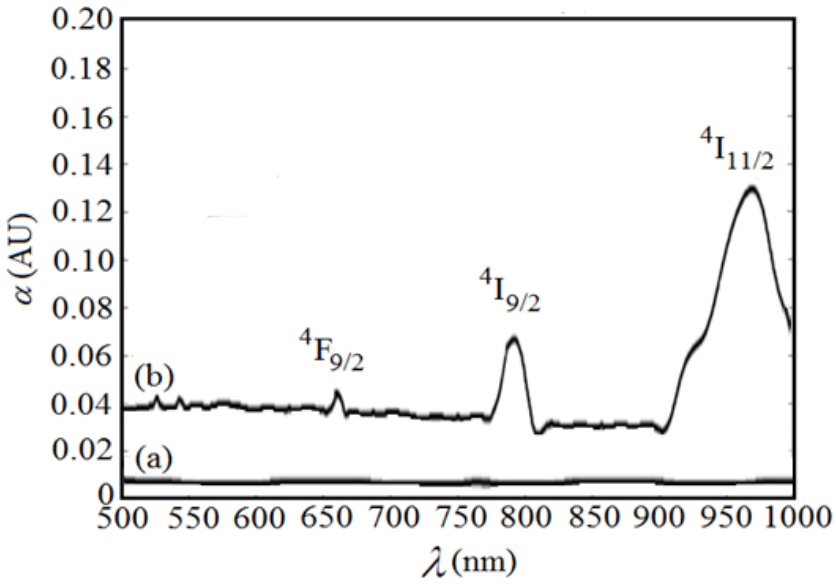

Fig. 6.4: Absorbance spectrum of ceria:Er synthesized with a doping reagent weight ratio of 5% with a) no calcination and b) calcinated at 900°C

6.3.2 Effect of calcination temperature and Er doping ratio

Firstly, the effect of the calcination temperature on the up-converted emission is discussed. Under 780 nm IR laser excitation, the visible emission of ceria doped with erbium, with a reagent weight ratio of 5%, at different annealing temperatures are shown in Fig. 6.5. It can be observed that the non-calcinated nanoparticles do not emit photons, under IR excitation,

which is expected given the spectrum for the non-calcinated sample shown in Fig. 6.4 where there is no absorption at 780 nm by the non-calcinated nanoparticles. The amplitudes of the emission of green (~ 555 nm) and red (~ 680 nm) lights, when the ceria:Er is illuminated with 780 nm light, increase with increasing the annealing temperature.

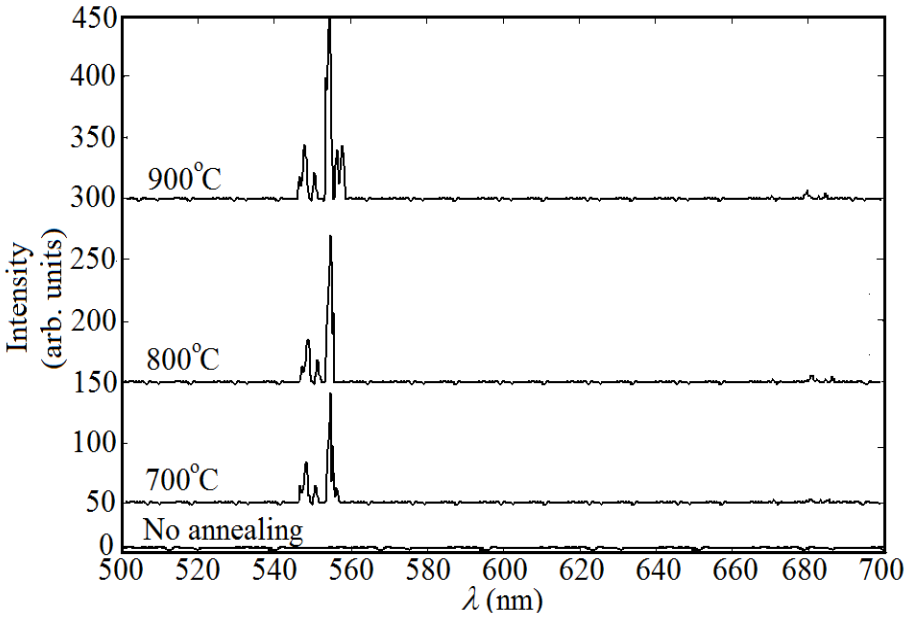

Fig. 6.5: Up-conversion emission of ceria:Er, 5% reagent weight ratio, at different calcinations temperatures

By increasing the calcination or the annealing temperature, erbium ions are crystallized and its energy levels become more stable with the formation of a complex with oxygen, so that the Er^{+3} ions act as centers for up-conversion process [98]. This can give an indication that the energy levels concept is the dominant factor as compared with the concentration of O-vacancies in up-conversion process. To prove this conclusion, the absorbance dispersion for the calcinated ceria doped erbium nanoparticles is shown in Fig. 6.6a, which shows a blue shift in the absorbance dispersion in the linear region, as compared to the absorbance dispersion of ceria doped with Er without annealing, which is shown in Fig. 4.5b. The direct allowed bandgap of the calcinated ceria:Er is calculated, as shown in Fig. 6.6b, to be 3.93 eV, much closer to 4 eV than any of the undoped or doped ceria nanparticles studied previously. Thus, the ceria nanoparticles

after calcination are mostly composed of CeO_2 with Ce in the Ce^{+4} state and contain a much reduced concentration of O-vacancies. In other words, Ce^{+3} ionization states are converted to Ce^{+4} states through the calcination process with the elimination of the O-vacancies, which were associated to Ce^{+3} ionization states. This explanation is in a perfect agreement with other research work [78-99]. So, as a conclusion, the results from the up-conversion process using ceria nanoparticles cannot be explained by invoking the O-vacancies defects. It will be shown later, in Section 6.4, that the mechanism used to explain the up-conversion emission depends only on the energy levels of the optical centers of the emission, erbium, in the ceria host.

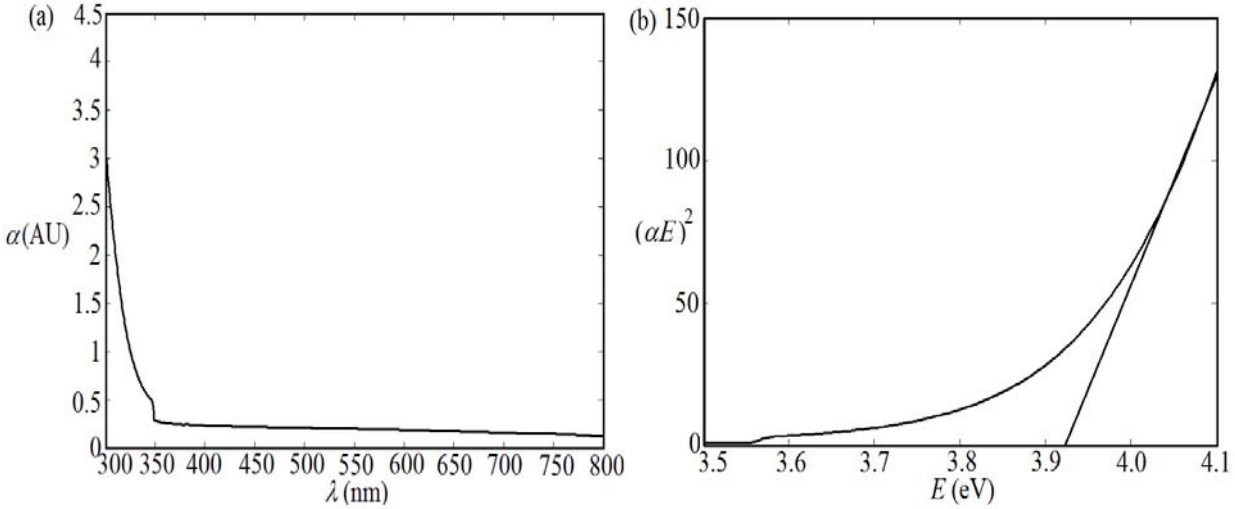

Fig. 6.6: a) Absorbance dispersion and b) direct bandgap calculation of ceria:Er nanoparticles, with a 5% reagent weight ratio and calcinated at 900°C

The impact of the weight ratio of erbium on the up-conversion emission is also studied. The emission spectra of ceria:Er at different reagent weight ratios, at fixed calcination temperature of 900°C, are shown in Fig. 6.7. It can be observed that the amplitudes of the green and red emissions are increased by increasing the weight ratio of Er, up to a weight percent of 5%. However, when the erbium reagent weight ratio is increased to 10%, the visible emissions are reduced compared to the lower reagent ratios due to the quenching effect of erbium complexes on the up-conversion emission. At lower concentrations of erbium, the ions are

randomly distributed in the host ceria and the distances between the ions, on average, are farther apart. Therefore, the concentration of erbium in a ceria host, at which the quenching effect is observed, is larger than 5% reagent weight ratio, which is nearly the same molecular doping ratio as stated in Table 4.2 at ratios up to 10%. This ratio is much higher than the molar concentrations at which quenching is observed in other hosts, such as a concentration of 0.25% in the case of $BaTiO_3:Er^{+3}$ powders or a concentration of 0.5% in $TiO_2:Er^{+3}$ powders [100]. This comparison is of great importance as it shows the role of ceria as a relatively low phonon host material, on our efforts to increase the up-conversion emission efficiency.

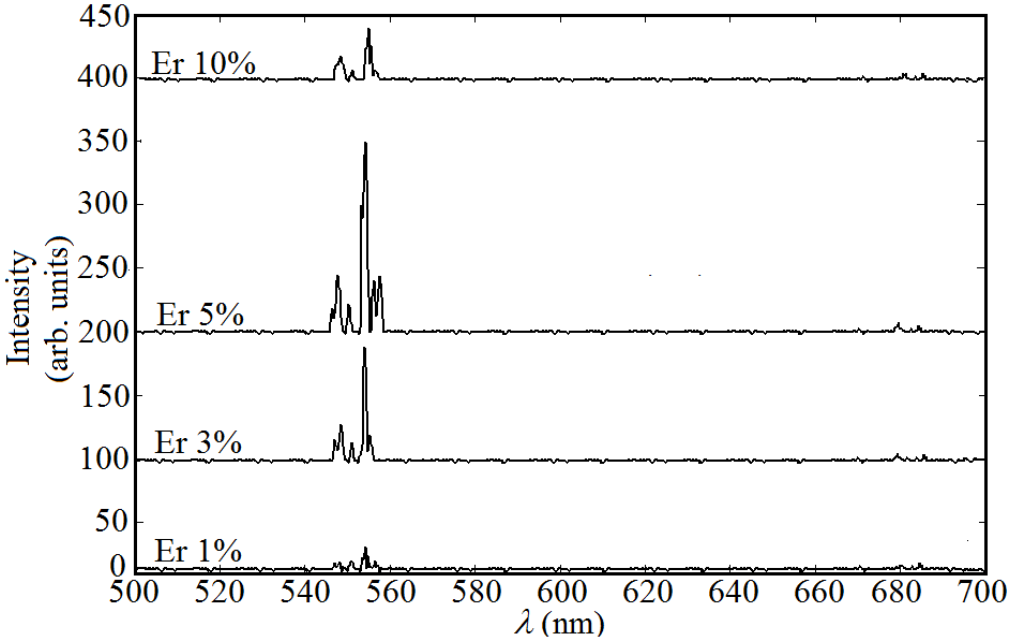

Fig. 6.7: Up-conversion emission of ceria:Er, within 900°C calcination, at different erbium reagent weight ratios

6.3.3 Power dependence

The logarithmic incidence power (P) and up-converted emission intensity (I) are shown in Fig. 6.8 for both the green and red emissions. A plot of log I versus log P yields a straight line with slope of power exponent n, which is the number of pump photons absorbed per up-converted photon emitted From Fig. 6.8, it can be observed that the value of n is 2.04 for the

green emission and is 1.60 for the red emission. Rounding, this is approximately 2, which means that both wavelength emissions obey the two-photon absorption process in up-conversion. However, the green emission shows a perfect up-conversion power exponent value compared to the red emission. This would imply a very efficient process, but the overall power of the red emission is much lower than the power measured for the green emission. We conclude that these nanoparticles, using our synthesis and calcination procedure, are promising material for green emission under IR excitation.

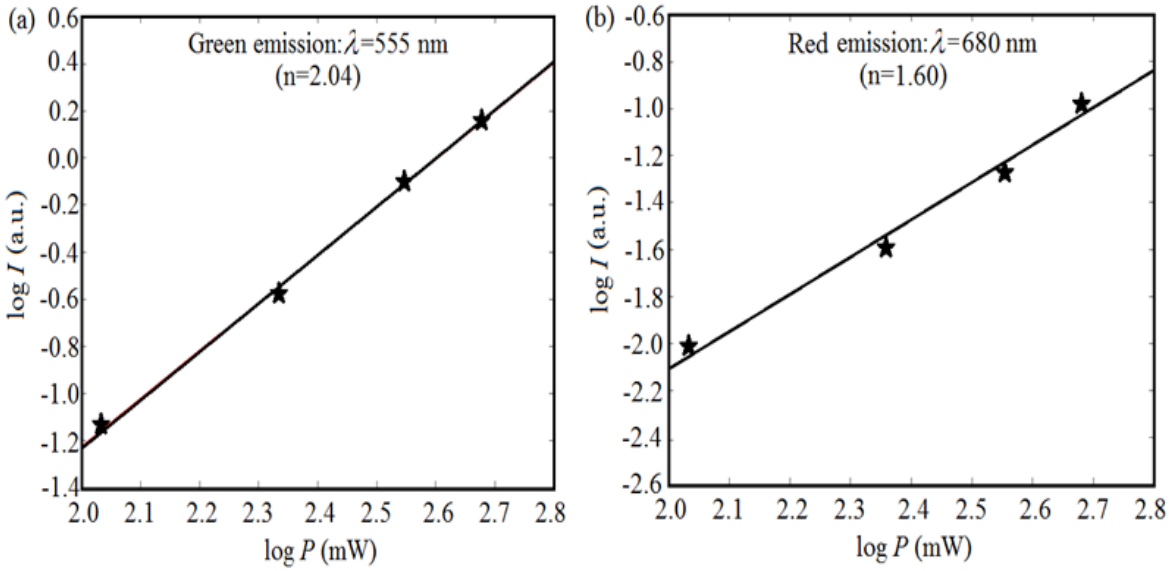

Fig. 6.8: Up-conversion power dependence on the input power of the 780 nm pump source for ceria:Er 5% reagent weight ratio calcinated at 900°C for a) green (~ 555 nm) and b) red (~ 680 nm) emission wavelengths.

6.3.4 UC emission for ceria:Er with additional lanathanide doapnts

In this section, we document the results of the up-conversion process when additional lanthanide dopants are incorporated in the ceria:Er nanoparticles. The weight percentage of Er in ceria is kept constant at 5% and the reagent weight ratios of the lanthanide dopants, neodymium and samarium, are 5% and 10%. In each case, the lanthanide-doped ceria:Er sample is calcinated

at 900°C. The emission spectra of Nd-ceria:Er and Sm-ceria:Er nanoparticles, pumped at 780 nm, are shown in Figs. 6.9 and 6.10, respectively.

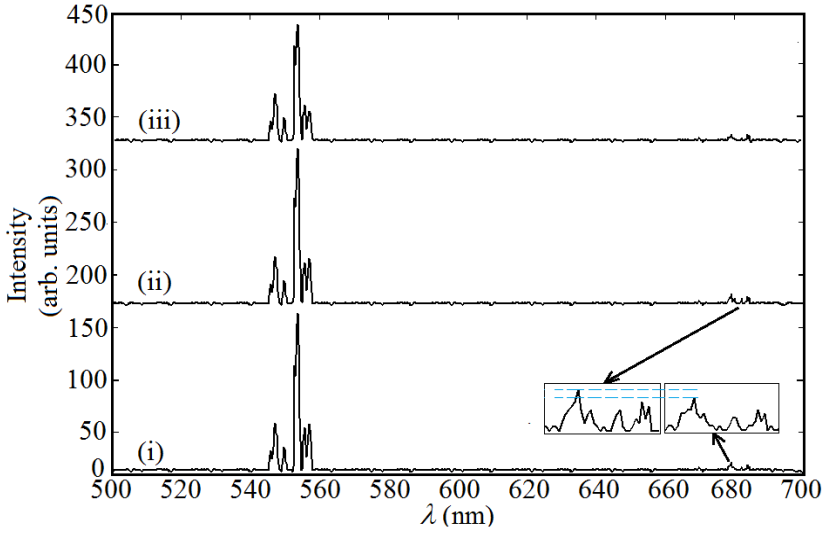

Fig. 6.9: Up-conversion emission of 900°C calcinated ceria:Er nanoparticles of 5% reagent weight of erbium with i) no added Nd, ii) added 5% reagent weight of Nd and iii) added 10% reagent weight of Nd (The insets show the slight improvement of red emissions within adding 5% reagent weight ratio of Nd)

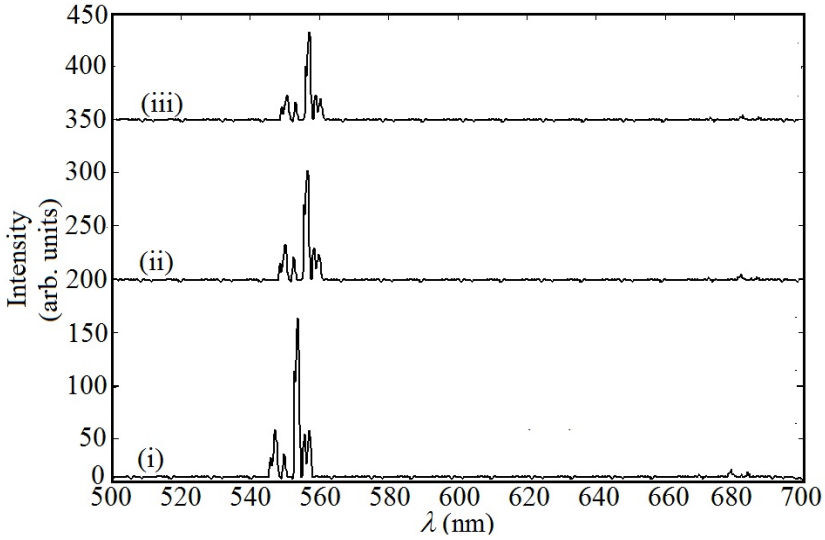

Fig. 6.10: Up-conversion emission of 900°C calcinated ceria:Er nanoparticles of 5% reagent weight of erbium with i) no added Sm, ii) added 5% reagent weight of Sm and iii) added 10% reagent weight of Sm.

For additional neodymium dopant, it can be shown that the red emission is slightly improved by 5%, compared to the ceria:Er system without neodymium, while the green emission for Nd-ceria:Er is approximately the same as the ceria:Er samples. The improvement in the red emission can be attributed to the alignment of $^4H_{9/2}$ energy level of neodymium with the $^4I_{9/2}$ energy level of erbium, as shown previously in Dieke diagram (Fig. 6.2). This alignment enables better pumping efficiency of the 780 nm excitation because of the energy transfer from excited Nd ions to Er ions. This mechanism is the same one applied multi-dopants system in some types of glasses hosts [101]. Also, the obtained results of green and red emissions in Nd-ceria:Er is in agreement with the results obtained by the up-conversion process in ceria:Er doped with ytterbium within another research work. As it is found that increasing the concentration of Yb in ceria:Er, the ratio of amplitudes of the red to green emission increased, compared to ceria:Er nanoparticles when pumped with IR excitation [102].

On the other hand, the green and red emissions for Sm-ceria:Er, for 5% reagent weight doping, are found to be lower than the same visible emissions of ceria:Er system without samarium dopant. Since none of the energy levels in samarium align with the erbium energy level of $^4I_{9/2}$, there is no energy transfer between Sm and Er to enhance the emission at ~ 680 nm. The reduction of visible amplitudes is resulted from the quenching effect of samarium. Generally, for higher reagent weight ratios of both dopants, neodymium and samarium, the quenching effect becomes dominant. The amplitudes of both the green emission at ~ 555 nm and the red emission at ~ 680 nm are lower for the ceria:Er doped with 10% of reagent weight ratios of neodymium or samarium than the amplitudes of the same up conversion emissions obtained from ceria:Er doped with 5% reagent weight ratio of the same lanthanide dopants.

Also, the results obtained from Sm-doped ceria:Er nanoparticles provide evidence that that the presence of O-vacancies defects do not enhance the up-conversion process and may in fact decrease the efficiency of the process. This evidence supports our conclusion that the impact of the co-doping technique in ceria nanoparticles through up-conversion application is related to an energy transfer mechanism that is permitted because of the alignment of energy levels of certain dopants with the energy levels of Er.

6.4 Suggested up-conversion mechanisms

The following discussion is an expansion on the conclusions drawn from the he results obtained during this study and presented in Section 6.3 using the information about the energy levels in Sm, Nd, and Er that are shown on Dieke diagram (Fig. 6.2). We suggest the following up-conversion mechanisms for ceria:Er and lanthanide-doped ceria:Er systems. Firstly, for ceria:Er system, Fig. 6.11 shows the energy level diagram of Er^{+3} ions in ceria, which can be considered a part of Dieke diagram shown in Fig. 6.2. Based on the emitted emission spectrum under 780nm excitation, it can be seen from Fig. 6.11 that there is a possible Excited State Absorption (ESA) or Ground State Absorption (GSA) route as follows [97]. The erbium ion is excited from $^4I_{15/2}$ level to $^4I_{9/2}$. Then, there is a non-radiative relaxation to $^4I_{11/2}$. While at this level, another ESA event occurs, exciting the Er ion to the level of $^4F_{7/2}$. A series of non-radiative relaxations are transpire, where the energy of the Er ion is reduced to lower levels such as $^2H_{11/2}$ and $^4F_{9/2}$. The radiative visible emissions result during the relaxation from these energy levels to $^4I_{15/2}$ level, green photons are emitted during the $^2H_{11/2}$ to $^4I_{15/2}$ transition and red photons are emitted during the $^4F_{9/2}$ to $^4I_{15/2}$ transition. The minor differences in the wavelengths shown in Fig. 6.11 and the wavelengths measured in the study on up-conversion can be attributed to small

errors in the position of the grating in the monochromator and/or a slight perturbation of the Er energy levels caused by the ceria host.

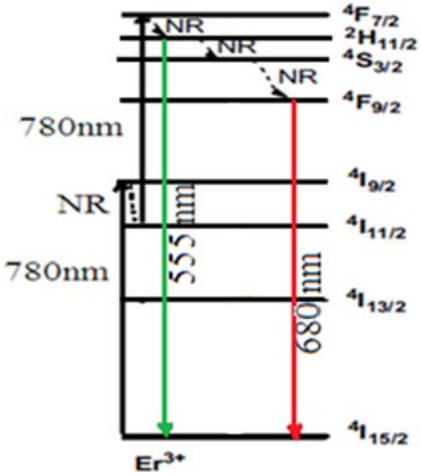

Fig. 6.11: Up-conversion mechanisms with suggested pathways for ceria:Er nanoparticles where the heavy black lines show the excitation of Er, the green and red lines are the transitions from the excited to ground state that produce green and red emission, respectively, and NR means that the transition is non-radiative

In case of Nd-ceria:Er, as shown in Fig. 6.12, there is an alignment between $^4H_{9/2}$ level of Nd with $^4I_{9/2}$ level of Er. The difference in energy between the levels $^4I_{9/2}$ and $^4H_{9/2}$ in Nd is approximately 780 nm. Then, we hypothesize that the dominant up-conversion mechanism is Energy Transfer (ET), in which the energy is transferred from a donor excited ion; Nd, to the neighboring acceptor ion; Er. That can explain the slight improvement of the red emissions in Nd-ceria:Er with relatively small doping weight ratio of neodymium. We expect that similar quenching mechanisms to those in ceria:Er are involved at high doping weight ratios of Nd.

There is no energy level available in Sm to which a 780 nm photon can excite a Sm ion from the ground state and consequently there is no energy transfer from samarium to erbium. The only observed impact of Sm in the Sm-ceria:Er system is a quenching of the up-conversion emission. It is possible that there is energy transfer from excited Er to Sm, which would explain the reduction in visible emissions from the Sm-ceria:Er as compared to the ceria:Er. Another

possibility is that the O-vacancies present in the Sm-doped ceria:Er modify the lifetimes of the excited states, which can reduce the time at which the excited Er ions exist at the $^4I_{11/2}$ before the second ESA event can occur or the O-vacancies reduce the lifetimes of some of the non-radiative relaxation pathways that compete with the radiative relaxation pathways.

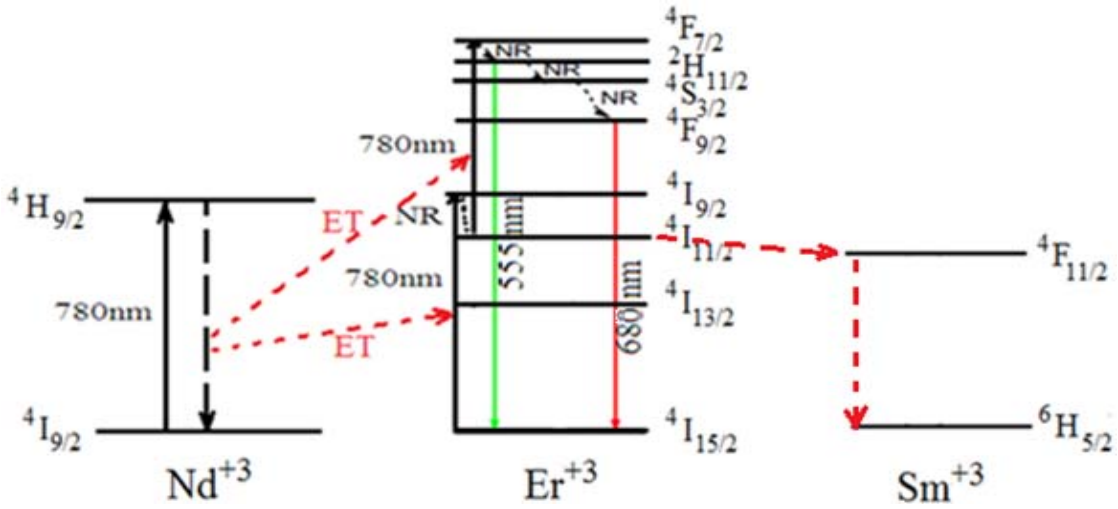

Fig. 6.12: Up-conversion mechanisms with suggested pathways for ceria:Er nanoparticles doped with neodymium or samarium, where ET indicates an energy transfer mechanism and NR indicates a non-radiative transition.

CHAPTER SEVEN

Conclusions & Future Work

7.1. Summary of research contributions

This thesis presents the impact of doping ceria with several tri-valent atoms on the optical and structural characteristics of ceria nanoparticles. The elements are selected from some of the most commonly used lanthanide and metal atoms. The lanthanide dopants are samarium and neodymium, which have positive association energies with respect to O-vacancies, and holmium and erbium, which are negative association energy lanthanides. The metal dopants that were studied are aluminum and, to a much lesser extent, iron.

The research contributions that have been made during this thesis project related to nanoparticle design and characterization are as follows.

1. We demonstrated that the association energy of the dopant atom determines the shift in allowed direct bandgap energy of ceria. When compared to undoped ceria, the direct bandgap of the ceria doped with a negative association element is increased, the peak emitted fluorescent intensity is reduced, and there is an increase of the average diameter of nanoparticles along with a decrease in lattice parameter and interplanar distance. The opposite results are obtained within the positive association lanthanides and metal dopants, compared to undoped ceria. We conclude that:
    - The negative association energy elements, holmium and erbium, act as O-vacancies scavengers when doped in ceria.

- The positive association energy lanthanide dopants, samarium and neodymium, increase the O-vacancies.

2. We conclude that the change in bandgap energy can be correlated to a change in the ratio of cerium in the Ce^{+4} to Ce^{+3} ionization states and a corresponding change in the concentration of O-vacancies. The correlation between the optical characteristics of ceria and the concentrations of Ce^{+4}, Ce^{+3}, and O-vacancies demonstrates a new method for qualitative measurement for Ce^{+4}, Ce^{+3}, and O-vacancies, which are important in determining a number of optical and chemical properties of ceria. A nondestructive and inexpensive optical measurement technique can be of a great importance to overcome the problems of other techniques currently employed, such X-ray photoelectron spectroscopy (XPS) and Raman spectroscopy.
3. The results obtained from the mixed doped ceria nanoparticles (MDC NPs) provide another verification that the negative association energy lanthanide dopants reduce the O-vacancies formed in ceria nanoparticles. For ceria doped with positive association energy elements, Sm and Nd, the addition of negative association dopants, such as Ho and Er, reduce the concentration of O-vacancies formed in the ceria NPs. MDC NPs have larger bandgap, lower fluorescent peak intensity, and larger diameter, compared to ceria doped with only positive association dopants. This conclusion can open a new window to control the concentration of O-vacancies in ceria by co-doping with positive association energy lanthanides and negative association energy lanthanide elements.

4. The study of two tri-valent metal atoms, aluminum and iron, as dopants, which are reported to improve the ionic conductivity of oxygen in ceria, show that Al-doped and Fe-doped ceria contains a higher concentration of O-vacancies than ceria doped with an equivalent weight percent of Nd or Sm, the two lanthanide elements that are shown in this study to increase the concentration of O-vacancies. This was concluded from the reduced bandgap and smaller average size of the Al-doped and Fe-doped nanoparticles. Al-doped ceria nanoparticles exhibited an enhanced fluorescence; much higher than Undoped and iron doped ceria. The origin of the fluorescence quenching in Fe-doped ceria was not studied. However, optical absorption by the Fe atoms likely reduces the pumping efficiency of the ceria and can absorb the visible emission from the Ce^{+3}. Aluminum is the most promising dopant in ceria in terms of defect engineering as it forces, based on our measured optical and structural characteristics, the largest increase in the concentration of O-vacancies.

The research contributions that have been made during this thesis project related to the characterization of ceria nanoparticle in two applications are as follows:

1. We demonstrate for the first time that ceria nanoparticles with a high concentration of O-vacancies can be used as molecular probes for dissolved oxygen in aqueous solutions. This is work build on our research conducted on doped ceria nanoparticles. The novel work is the use of ceria nanoparticles, both undoped and doped, to sense DO using an optical fluorescence quenching technique instead of the traditional ceria resistive sensing technique.

a. The emitted fluorescence from the ceria NPs shows a clear inverse relation with DO concentration for all of the nanoparticles studied. Stern-Volmer constants, which indicate the sensitivity of the sensing material for the oxygen quencher, are calculated for the undoped and doped ceria nanoparticles. Generally, all of our studied ceria nanoparticles samples show higher sensitivity than some of the fluorescent dyes currently used in optical DO sensing. The value of Stern-Volmer constant for the doped ceria NPs is up to 2.5 times larger than that of undoped ceria. Aluminum-doped ceria exhibits the best sensitivity to DO. For the lanthanide dopants, neodymium-doped ceria shows better sensitivity than ceria nanoparticles doped with samarium.
b. The size of our undoped and doped ceria nanoparticles of range 5-7 nm is the smallest, to the best of our knowledge, fluorophores for DO sensing that can be used directly in aqueous solutions.
c. Our synthesized undoped and doped ceria nanoparticles show relatively excellent thermal stability of these' sensitivities when compared to the thermal stability of other fluorescent dyes currently used in optical DO sensing. Aluminum-doped ceria has the best thermal stability as compared to undoped or lanthanide doped ceria. In the lanthanide dopants category, neodymium dopant shows much better thermal stability of K_{SV} than the samarium dopant.

2. The doping technique in ceria is applied to obtain high optical up-conversion efficiency. The up-conversion material is ceria doped with erbium due to properties of erbium that permit two-photon absorption coupled with radiative emission in the visible from its high

energy states and the fact that ceria is a low phonon host. Ceria doped with erbium (ceria:Er) nanoparticles are excited within 780 nm laser and found to emit green and red emissions only after a calcination procedure where 900^{o}C for one hour was found to be the most optimum of the thermal anneals studied. However, the calcination step increases the allowed direct bandgap of ceria, which indicates the that the calcination step also converted cerium from the Ce^{+3} to Ce^{+4} ionization states and diminished the concentration of O-vacancies. The addition of neodymium at a weight ratio of 5% during the synthesis of ceria:Er nanoparticles improves slightly the visible emissions due to the alignment of 780 nm pumping energy levels between neodymium and erbium. However, the addition of samarium to ceria:Er quenches visible emissions due to the inability to transfer energy from Sm to Er. This provides evidence that the alignment of energy levels of the dopant with Er is the dominant factor in the modification of the up-conversion process and that there is O-vacancy play no (or may play a slightly negative) role on the up-conversion process.

As a summary, doping ceria with tri-valent dopants has measurable impact on the optical and structural characteristics of the nanoparticles by controlling the concentrations of Ce^{+3} and the O-vacancies. The first demonstration of ceria as a molecular probe for dissolved oxygen was shown, where the concentration of O-vacancies as well as the mobility of the vacancies has a significant impact on the performance of the molecular probe between room temperature and 50^{o}C. The selection of the dopant in ceria affects the up-conversion efficiency. However, our study indicates that it is the alignment of the energy levels of the dopant with respect to Er that impacts the up-conversion process and the O-vacancy concentration does not.

Aluminum-doped ceria can be considered a very promising nanostructure to be used as the molecular probe in optical DO sensor due to its relatively high sensitivity with near perfect thermal stability. This nanomaterial can be used in industrial or environmental applications, but we can not recommend its use in biomedical applications without a study on the toxicity of the Al-doped nanoparticles. Without this study, we consider ceria doped with neodymium to be promising for usage as a molecular probe for Do in biomedical engineering applications.

7.2 Suggested future work

There are many applications can be explored as future work. The following paragraphs describe briefly some examples to explain that our conclusions can help in different applications in wide range of fields. Firstly, ceria doped with the positive association lanthanides can be used as free radical scavengers. Studies have already demonstrated that undoped ceria have preventative and therapeutic effects on cells exposed to high concentrations of free radicals as a result of physical trauma, exposure to toxins, etc. A study of the biological effect of the doped ceria nanoparticles on cells and organism should be conducted. The ability to adjust the O-vacancy concentration in the nanoparticles via doping will likely enable researchers to finely tune the free radial scavenging of the nanoparticles to precisely determine the level of the biochemical protection provided by the nanoparticles.

There are applications where trapping the nanoparticles in a flexible matrix, such as electrospun fibers, may be required to address concerns about releasing nanoparticles in the environment. Nanofibers can offer suitable host for ceria nanoparticles for a number of applications where control of the location of the nanoparticles during and after the measurement

is important. These nanofibers can be used in different applications such as free radical filters and water waste treatment.

The scavenging of O-vacancies by ceria doping with negative association lanthanides, can be helpful in field effect transistor (FET) in which high-k films are currently deposited on germanium substrates. Among the oxides films used, CeO_2 is studied extensively because it reduces the density of interface states, however it suffers from leakage current since it has a relatively low bandgap and exhibits charge trapping [103]. Charge trapping is a common phenomenon observed in most high-k dielectric materials during device operation as some charge may be trapped in the insulator as it passes through the gate stack, causing device instabilities such as threshold voltage (V_{th}) shifts and drive current degradation [104]. Charge trapping is a result of the oxygen vacancies present in ceria [58]. Then, ceria doped with high association energy elements may be useful because these dopants reduce the oxygen vacancies and increase the bandgap of ceria. This can likely lead to a reduction in charge trapping and the current degradation.

The improvement of both the down-conversion (fluorescence) and up-conversion processes can be used in sustainable energy applications. Currently, we have initiated a trial to improve the efficiency of Si-wafer solar cells using doped ceria films. This layer, above the cell, will contain ceria doped with neodymium or aluminum, which has been shown in this thesis to increase the visible emission under UV emission.

A suggested improvement to the experimental setups used during this thesis is the addition of optical parametric oscillator (OPO) to the fluorescence and up-conversion setups. This will allow the measurement of the the emission lifetime in both optical conversion

processes, which will assist in a more comprehensive study on the role of O-vacancies on the up-conversion process in Nd-doped and Sm-doped ceria:Er and the evaluation of other doped ceria materials

An alternative to the measurement of fluorescence quenching of the doped ceria for DO sensing of is a measurement based upon the up-conversion process. It is known that calcination at extremely high temperatures initiates the formation of O-vacancies in ceria [34]. Thus, ceria:Er nanoparticles should be annealed in a special furnace at temperatures around 1125^{o}C to convert some Ce^{+4} ionization states into Ce^{+3} states, with forming associated O-vacancies which are the probe for the dissolved oxygen. Since the excitation wavelength for up-conversion is at 780 nm, the transmission of the pump through water, particularly water containing organic materials, will be improved.

References

[1] M. G. Pirovano, A. Hofmann and J. Sauer, "Oxygen vacancies in transition metal and rare earth oxides: Current state of understanding and remaining challenges," *Surf. Sci. Rep.*, vol. 62, pp. 219–270, 2007.

[2] E. J. Park, J. Choi, Y. K. Park and K. Park, "Oxidative stress induced by cerium oxide nanoparticles in cultured BEAS-2B cells," *Toxicology*, vol. 245, no. 1-2, pp. 90–100, 2007.

[3] J. L. Lu, H. J. Gao, S. Shaikhutdinov and H. J. Freund, "Morphology and defect structure of the CeO_2(111) films grown on Ru(001) as studied by scanning tunneling microscopy," *Surf. Sci.*, vol. 600, pp. 5004–5010, 2006.

[4] V. V. Kharton, F. M. Figueiredo, L. Navarro, E. N. Naumovich, A. V. Kovalevsky, A. A. Yaremchenko, A. P. Viskup, A. Carneiro, F. Marques and J. R. Frade, "Ceria-based materials for solid oxide fuel cells," *J. Mater. Sci*., vol. 36, pp. 1105–1117, 2001.

[5] D. Schubert, R. Dargusch, J. Raitano and S. W. Chan, "Cerium and yttrium oxide nanoparticles are neuroprotective," *Biochem. Biophys. Res. Comm.*, vol. 342, pp. 86–91, 2006.

[6] A. Y. Estevez, S. Pritchard, K. Harper, J. W. Aston, A. Lynch, J. J. Lucky, J. S. Ludington, P. Chatani, W. P. Mosenthal, J. C. Leiter, S. Andreescu and J. S. Erlichman, "Neuroprotective mechanisms of cerium oxide nanoparticles in a mouse hippocam brain slice model of ischemia," *Free Rad. Bio. Med.*, vol. 51, pp. 1155–1163, 2011.

[7] B. A. Rzigalinski, K. Meehan, R. M. Davis, Y. Xu and C. A. Cohen, "Radical nanomedicine," *Nanomedicine*, vol. 1, no. 4 , pp. 399-412, 2006

[8] S. Tsunekawa, T. Fukuda and A. Kasuya, "Blue shift in ultraviolet absorption spectra of monodisperse CeO_{2-x} nanoparticles," *J. Appl. Phys.*, vol. 87, no. 3, pp. 1318-1321, 2000.

[9] X. J. Yu, P. B. Xie and Q. D. Su, "Size-dependent optical properties of nanocrystalline CeO_2: Er obtained by combustion synthesis," *Phys. Chem. Chem. Phys.,* vol.3, pp. 5266-5269, 2001.

[10] M. S. Rahman, E. K. Evangelou, A. Dimoulas, G. Mavrou and S. Galata, "Anomalous charge trapping dynamics in cerium oxide grown on germanium substrate," *J. Appl. Phys.*, vol. 103, pp. 064514, 2008.

[11] B. Steel and A. Heinzel, "Materials for fuel-cell technologies," *Nature*, vol. 414, pp. 345-352, 2001.

[12] G. Dantelle, M. Mortier and D. Vivien, "Infrared emission enhancement in Yb/Er/Ce-codoped glass-ceramics," *Phys. Chem. Glasses: Eur. J. Glass Sci. Technol. B*, vol. 47, no.2, pp. 150–153, 2006

[13] S. Shen, B. Richards and A. Jha, "Enhancement in pump inversion efficiency at 980 nm in Er^{+3}, Er^{+3}/Eu^{+3} and Er^{+3}/Ce^{+3} doped tellurite glass fibers," *Opt. Exp.*, vol. 14, no. 12, pp. 5050-5054, 2006.

[14] P. Jasinski, T. Suzuki and H. U. Anderson, "Nanocrystalline undoped ceria oxygen sensor," *Sens. Act. B*, vol. 95, no. 1–3, pp. 73-77, Oct. 2003.

[15] S. Deshpande, S. Patil, S. Kuchibhatla and S. Seal, "Size dependency variation in lattice parameter and valency states in nanocrystalline cerium oxide," *Appl. Phys. Lett.*, vol. 87, pp. 133113, 2005.

[16] A. Gayen, K. R. Priolkar, A. K. Shukla, N. Ravishankar and M. S. Hegde, "Oxide-ion conductivity in $Cu_xCe_{1-x}O_2$ ($0 \leq x \leq 0.10$)," *Mat. Res. Bull.*, vol. 40, pp. 421–431, 2005.

[17] T. Dhannia, S. Jayalekshmi, M. C. S Kumar, T. P. Rao and A. C. Bose, "Effect of iron doping and annealing on structural and optical properties of cerium oxide nanocrystals," *J. Phys. Chem. Solids*, vol. 71, pp. 1020–1025, 2010.

[18] R. Gerhardt, W. K. Lee and A. S. Nowick, "Anelastic and dielectric relaxation of Scandia-doped-ceria," *J. Phys. Chem. Solids*, vol. 48, no. 6, pp. 565-569, 1987.

[19] E. Suda, B. Pacaud and M. Mori, "Sintering characteristics, electrical conductivity and thermal properties of La-doped ceria powders," *J. Alloys Compd.*, vol. 408, no. 412, pp. 1161–1164, 2006.

[20] S. Dikmen, P. Shuk and M. Greenblatt, "Hydrothermal synthesis and properties of $Ce_{1-x}La_xO_2$ solid solutions," *Solid State Ion.*, vol. 126, pp. 89–95, 1999.

[21] H. Yamamura, S. Takeda and K. Kakinuma, "Dielectric relaxations in the $Ce_{1-x}Nd_xO_2$," *Solid State Ion.*, vol. 178, pp. 1059–1064, 2007.

[22] T. Dhannia, S. Jayalekshmi, M. C. S. Kumar, T. P. Rao and A. C. Bose, "Effect of aluminum doping and annealing on structural and optical properties of cerium oxide nanocrystals," *J. Phys. Chem. Solids*, vol. 70, pp. 1443–1447, 2009.

[23] F. Zhang, P. Wang, J. Koberstein, S. Khalid and S. W. Chan, "Cerium oxidation state in ceria nanoparticles studied with X-ray photoelectron spectroscopy and absorption near edge spectroscopy," *Surf. Sci.*, vol. 563, pp. 74-82, 2004.

[24] D. R. Mullins, S. H. Overbury and D.R. Huntley, "Electron spectroscopy of single crystal and polycrystalline cerium oxide surfaces", *Surf. Sci.*, vol. 409, pp. 307-319, 1998.

[25] L. Qiu, F. Liu, L. Zhao, Y. Ma and J. Ya, "Comparative XPS study of surface reduction for nanocrystalline and microcrystalline ceria powder," *App. Surf. Sci.*, vol. 25, pp. 4931–4935, 2006.

[26] F. El-Diasty, "Coherent anti-Stokes Raman scattering: Spectroscopy and microscopy," *Vib. Spect.*, vol. 55, pp. 1–37, 2011.

[27] D. A. Andersson, S. I. Simak, N. V. Skorodumova, 1. A. Abrikosov and B. Johansson, "Optimization of ionic conductivity in doped ceria," *PNAS*, vol. 83, pp. 1–4, 2006.

[28] M. Nakayama and M. Martin, "First-principles study on defect chemistry and migration of oxide ions in ceria doped with rare-earth cations," *Phys. Chem. Chem. Phys.*, vol. 11, pp. 3241–3249, 2009.

[29] X. Wei, W. Pan, L. Cheng and B. Li, "Atomistic calculation of association energy in doped ceria," *Solid State Ion.*, vol. 180, pp. 13-17, 2009.

[30] H. Lv, H. Tu, B. Zhao, Y. Wu and K. Hu, "Synthesis and electrochemical behavior of $Ce_{1-x}Fe_xO_2$ as a possible SOFC anode materials," *Solid State Ion.*, vol. 177, pp. 3467–3472, 2007.

[31] M. Iosin, V. Canpean and S. Astilean, "Spectroscopic studies on pH and thermally induced conformational changes of Bovine Serum Albumin adsorbed onto gold nanoparticles," *J. Photochem. Photobio. A*, vol. 217, no. 2, pp. 395-401, 2011.

[32] G. Dantelle, M. Mortier, D. Vivien and G. Patriarche, "Influence of Ce^{+3} doping on the structure and luminescence of Er^{+3}-doped transparent glass-ceramics," *Opt. Mat.*, vol. 28, pp. 638–642, 2006.

[33] D. Matsuura, "Red, green and blue up-conversion luminescence of trivalent rare earth ion-doped Y_2O_3 nanocrystals," *Appl. Phys. Lett.*, vol. 81, no. 24, pp. 4526-4528, 2002.

[34] G. R. Rao and B. G. Mishra, "Structural, redox and catalytic chemistry of ceria based materials," *Bull. Cat. Soc. India*, vol. 2, pp. 122-134, 2003.

[35] A. Trovarelli, *Catalysis by ceria and related materials*, Imperial College Press, London, 2005.

[36] M. Nolan, J. E. Fearon and G. W. Watson, "Oxygen vacancy formation and migration in ceria," *Solid State Ion.*, vol. 177, pp. 3069–3074, 2006.

[37] S. Basu, P. S. Devi and H. S. Maiti, "Synthesis and properties of nanocrystalline ceria powders," *J. Mat. Res.*, vol. 19, no. 11, pp. 3162-3171, Nov 2004.

[38] N. Cioatera, V. Parvulescu, A. Rolle and R. N. Vannier, "Effect of dopant on the thermal electrical behaviour of nanostructured ceria materials," *Int. Semicond. Conf.*, pp. 317 – 320, 2010.

[39] T. Skala, N. Tsud, K. C. Prince and V. Matolin, "Formation of alumina–ceria mixed oxide in model systems," *App. Surf. Sci.*, vol. 257, pp. 3682–3687, 2011.

[40] B. Matovic, Z. Dohcevic-Mitrovic, M. Radovic, Z. Brankovic, G. Brankovic, S. Boskovic and Z. V. Popovic, "Synthesis and characterization of ceria based nanometric powders," *J. Power Sources*, vol. 193, pp. 146–149, 2009.

[41] J. Pankove, *Optical processes in semiconductors*, Dover Publications Inc., New York, 1971, pp. 34-36.

[42] P. V. Mieghem, "Theory of band tails in heavily doped semiconductors," *Rev. Mod. Phys.*, vol. 64, no. 3, pp. 755-793, July 1992.

[43] P. Patsalas, S. Logothetidis, L. Sygellou and S. Kennou, "Structure-dependent electronic properties of nanocrystalline cerium oxide films," *Phys. Rev. B*, vol. 68, pp. 035104, 2003.

[44] L. Yin, Y. Wang, G. Pang, Y. Koltypin and A. Gedanken, "Sonochemical synthesis of cerium oxide nanoparticles-effect of additives and quantum size effect," *J. Coll. Int. Sci.*, vol. 246, no. 1, pp. 78-84, 2002.

[45] A. N. Shmyreva, A. V. Borisov and N. V. Maksimchuk, "Electronic sensors built on nanostructured cerium oxide films," *Nanotech. Russia*, vol. 5, no. 5–6, pp. 382–389, 2010.

[46] D. Frackowiak, "The Jablonski Diagram," *J. Photochem. Photobio. B*, vol. 2, no. 3, pp. 399-408, 1988.

[47] J. Chu and A. Sher, *Device Physics of Narrow Gap Semiconductors*, Springer, New York, 2010, pp. 125-132.

[48] S. Sathyamurthy, K. J. Leonard, R. T. Dabestani and M. P. Paranthaman, "Reverse micellar synthesis of cerium oxide nanoparticles," *Nanotech.*, vol. 16, pp. 1960-1964, 2005.

[49] L. Reimer and H. Kohl, *Tansmission Electron Microscope: Physics of Image Formation*, 5th ed., Springer, New York, 2008.

[50] B. D. Cullity, *Elements of X-ray Diffraction*, Addison-Wesley publishing company Inc., Massachusetts, 1956.

[51] J. F. Watts and J. Wolstenholme, *Introduction to Surface Analysis by XPS and AES*, Wiley, Chichester, 2003.

[52] H. Chen and H. Chang, "Homogeneous precipitation of cerium dioxide nanoparticles in alcohol/water mixed solvents," *Coll. Surf. A*, vol. 242, pp. 61–69, 2004.

[53] N. J. Lawrence, K. Jiang and C. L. Cheung, "Formation of a porous cerium oxide membrane by anodization," *Chem. Comm.*, vol. 47, pp. 2703-2705, 2011.

[54] M. K. Rath, S. K. Acharya, B. H. Kim, K. T. Lee and B. G. Ahn, "Photoluminescence properties of sesquioxide doped ceria synthesized by modified sol–gel route," *Mat. Lett.*, vol. 65, pp. 955–958, 2011.

[55] S. H. Yu, H. Colfen and A. Fischer, "High quality CeO_2 nanocrystals stabilized by a double hydrophilic block copolymer," *Coll. Surf. A*, vol. 243, pp. 49-52, 2004.

[56] M. G. Sujana, K. K. Chattopadyay and S. Anand, "Characterization and optical properties of nano-ceria synthesized by surfactant-mediated precipitation technique in mixed solvent system," *Appl. Surf. Sci.*, vol. 254, pp. 7405-7409, 2008.

[57] P. Nachimuthu, W. C. Shih, R. S. Liu, L. Y. Jang and J. M. Chen, "The study of nanocrystalline cerium oxide by X-ray absorption spectroscopy," *J. Solid State Chem.*, vol. 149, pp. 408-413, 2000.

[58] E. K. Evangelou, M. S. Rahman and A. Dimoulas, "Correlation of charge buildup and stress-induced leakage current in cerium oxide films grown on Ge (100) substrates," *IEEE Trans. Elec. Dev.*, vol. 56, no. 3, pp. 399-407, 2009.

[59] O. S. Wolfbeis, *Fiber Optic Chemical Sensors and Biosensors,* CRC Press, Boca Raton, 1991, pp. 13-17.

[60] N. Masson and P. J. Ratcliffe, "Analysis of von Hippel–Lindau Tumor Suppressor as a Mediator of Cellular Oxygen Sensing," *Meth. Enzym.*, vol. 381, pp. 305-320, 2004.

[61] A. Dittmar, S. Mangin, C. Ruban, W. H. Newman, H. F. Bowman, V. Dupuis, G. Delhomme, N. F. Shram, R. Cespuglio, N. Jaffrezic-Renault, P. Roussel, D. Barbier and C. Martelet, "In vivo and in vitro evaluation of specially designed gold and carbon fiber oxygen microelectrodes for living tissues," *Sens. Act. B*, vol. 44, pp. 316-320, 1997.

[62] C. G. Cooney, B. C. Towe, and C. R. Eyster, "Optical pH, oxygen and carbon dioxide monitoring using a microdialysis approach," *Sens. Act. B*, vol. 69, pp. 183-188, 2000.

[63] P. R. Warburton, R. S. Sawtell, A. Watson, and A. Q. Wang, "Failure prediction for a galvanic oxygen sensor," *Sens. Act. B*, vol. 72, pp. 197-203, 2001.

[64] H. Suzuki, T. Hirakawa, T. Hoshi and H. Toyooka, "Micromachined sensing module for pO_2, pCO_2, and pH and its design optimization for practical use," *Sens. Act. B*, vol. 76, pp. 565-572, 2001.

[65] R. Sanghavi, M. Nandasiri, S. Kuchibhatla, W. Jiang, T. Varga, P. Nachimuthu, M. H. Engelhard, V. Shutthanandan, S. Thevuthasan, A. Kayani and S. Prasad, "Thickness dependency of thin-film samaria-doped ceria for oxygen sensing," *IEEE Sens. J.*, vol. 11, no. 1, pp. 217-224, 2011.

[66] D. A. Chang-Yen and B. K. Gale, "An integrated optical oxygen sensor fabricated using rapid-prototyping techniques," *Lab Chip*, vol. 3, pp. 297–301, 2003.

[67] G. A. Crosby and R. J. Watts, "Spectroscopic characterization of complexes of ruthenium(II) and iridium(III) with 4,4'-diphenyl-2,2'-bipyidine and 4,7-diphenyl-a,10-phenanthroline," *J. Am. Chem. Soc.*, vol. 93, no. 13, pp. 3184-3188, 1971.

[68] C. T. Lin, W. Bottcher, M. Chou, C. Creutz and N. Sutin, "Mechanism of the quenching of the emission of the substituted polypyridineruthenium(II) complexes by iron(III), chromium(III), and europium(III) ions," *J. Am. Chem. Soc.*, vol. 98, no. 21, pp. 6536-6544, 1976.

[69] P. Hartmann, W. Ziegler, G. Holst and D. W. Lubbers, "Oxygen flux fluorescence lifetime imaging," *Sens. Act. B*, vol. 38, pp. 110-115, 1997.

[70] P. Douglas and K. Eaton, "Response characteristics of thin film oxygen sensors, Pt and Pd octaethylporphyrins in polymer films," *Sens. Act. B*, vol. 82, no. 2-3, pp. 200-209, 2002.

[71] C. S. Chu and Y. L. Lo, "A plastic optical fiber sensor for the dual sensing of temperature and oxygen," *IEEE Photo. Tech. Lett.*, vol. 20, no.1, pp. 63-65, 2008.

[72] E. Kraker, A. Haase, B. Lamprecht, G. Jakopic, C. Konrad, and S. Köstler, "Integrated organic electronic based optochemical sensors using polarization filters," *Appl. Phys. Lett.*, vol. 92, no. 3, pp. 033302, 2008.

[73] L. Shen, M. Ratterman, D. Klotzkin, and I. Papautsky, "Use of a low-cost CMOS detector and cross-polarization signal isolation for oxygen sensing," *IEEE Sens. J.*, vol. 11, no. 6, pp. 1359-1360, 2011.

[74] B. R. Eggins, *Biosensors: An Introduction*, John Wiley and Sons Ltd., New York, 1997.

[75] Y. E. K. Lee and R. Kopelman, "Optical nanoparticles sensors for quantitative intracellular imaging," *WIREs Nanomed. Nanobiotech.*, vol. 1, no. 1, pp. 98-110, 2009.

[76] C. S. Chu and Y. L. Lo, "Optical fiber dissolved oxygen sensor based on Pt(II) complex and core-shell silica nanoparticles incorporated with sol–gel matrix," *Sens. Act. B*, vol. 151, no.1, pp. 83-89, 2010.

[77] M. Cappelezzo, C. A. Capellari, S. H. Pezzin and L. A. F. Coelho, "Stokes-Einstein relation for pure simple fluids," *J. Chem. Phys.*, vol. 126, pp. 224516/1-5, 2007.

[78] S. Damyanova, B. Pawelec, K. Arishtirova, M. V. Huerta and J. G. Fierro, "Study of the surface and redox properties of ceria-zirconia oxides," *Appl. Cat. A*, vol. 337, pp. 86-96, 2008.

[79] Y. L. Lo, C. S. Chu, J. P. Yur and Y. C. Chang, "Temperature compensation of fluorescence intensity-based fiber-optic oxygen sensors using modified Stern-Volmer model," *Sens. Act. B*, vol. 131, pp. 479–488, 2008.

[80] R. Shinar, Z. Zhou, B. Choudhury and J. Shinar, "Structurally integrated organic light emitting device-based sensors for gas phase and dissolved oxygen," *Anal. Chim. Acta.*, vol. 568, pp. 190-199, 2006.

[81] P. Sharma and K. P. Mishra, "Aluminum-induced maternal and developmental toxicity and oxidative stress in rat brain: Response to combined administration of Tiron and glutathione," *Reprod.Toxicology*, vol. 21, no. 3, pp. 313-321, 2006.

[82] H. Guo, "Two- and three-photon upconversion of LaOBr:Er^{+3}," *Optical Mat.*, vol. 29, pp. 1840–1843, 2007.

[83] E. Heumann, S. Bär, K. Rademaker, G. Huber, S. Butterworth, A. Diening and W. Seelert, "Semiconductor-laser-pumped high-power upconversion laser," *Appl. Phys. Lett.*, vol. 88, pp. 061108, 2006.

[84] D. S. Funk, S. B. Stevens, S. S. Wu and J. G. Eden, "Tuning, temporal, and spectral characteristics of the green (λ~549 nm), holmium-doped fluorozirconate glass fiber laser," IEEE J. Quant. Elect., vol. 32, pp. 638-645, 1996.

[85] A. Shukla, S. Mukherjee, S. Sharma, V. Agrawal, K. V. Kishan and P. Guptasarma, "A novel UV laser-induced visible blue radiation from protein crystals and aggregates: scattering artifacts or fluorescence transitions of peptide electrons delocalized through hydrogen bonding," *Arch. Biochem. Biophys.*, vol. 428, no. 2, pp. 144-153, August 2004.

[86] Z. Chao, S. Lingdong, Z. Yawen and Y. Chunhua, "Rare earth upconversion nanophosphors: synthesis, functionalization and application as biolabels and energy transfer donors," *J. Rare Earth*, vol. 28, no. 6, pp. 807-819, 2010.

[87] T. Trupke, M. A. Green and P. Würfel, "Improving solar cell efficiencies by up-conversion of sub-band-gap light," *J. Appl. Phys.*, vol. 92, pp. 4117, 2002.

[88] T. Trupke, A. Shalav, B. S. Richards, P. Wurfel, and M. A. Green, "Efficiency enhancement of solar cells by luminescent up-conversion of sunlight," *Sol. Energy Mater. Sol. Cells*, vol. 90, no. 18-19, pp. 3327–3338, 2006.

[89] A. Braud, "Excitation Mechanisms of RE Ions in Semiconductors," in Rare Earth Doped III-Nitrides for Optoelectronic and Spintronic Applications, K. O'Donnell and V. Dierolf, The Netherlands: Springer, 2010, pp. 269-272.

[90] M. Pollnau, "Dynamics of solid-state coherent light sources," in Frontiers of Optical Spectroscopy, B. Di Bartolo and O. Forte, The Netherlands: Springer, 2005, pp. 571-589.

[91] J. G. Bunzli and S. V. Eliseeva, "Basics of Lanthanide Photophysics," in *Lanthanide Luminescence: Photophysical, Analytical and Biological Aspects*, P. Hanninen and H. Harma, Berlin: Springer, 2011.

[92] G. H. Dieke and H. M. Crosswhite, "The Spectra of the Doubly and Triply Ionized Rare Earths," *Appl. Opt.*, vol. 2, pp. 675-686, 1963.

[93] R. T. Wegh, A. Meijerink, R. J. Lamminmaki and J. Holsa, "Extending Dieke's diagram," *J. Lumines.*, vol. 87, pp. 1002-1004, 2000.

[94] P. S. Peijzel, A. Meijerink, R. T. Weigh, M. F. Reid and G. W. Burdick, "A complete $4f^n$ energy level diagram for all trivalent lanthanide ions," *J. Solid State Chem.*, vol. 178, pp. 448–453, 2005.

[95] F. Auzel, "Upconversion and anti-Stokes processes with f and d ions in solids," *Chem. Rev.*, vol. 104, no. 1, pp. 104-139, 2004.

[96] W. H. Weber, K. C. Hass and J. R. McBride, "Raman study of CeO_2 Second-order scattering, lattice dynamics, and particle-size effects," *Phys. Rev. B*, vol. 48, pp. 178-185, 1993.

[97] H. Guo, "Green and red upconversion luminescence in CeO_2:Er^{+3} powders produced by 785nm laser," *J. Solid State Chem.*, vol. 180, pp. 127–131, 2007.

[98] R. Balda, S. Garcia-Revilla, J. Fernandez, V. Seznec, V. Nazabal, X. H. Zhang, J. L. Adam, M. Allix and G. Matzen, "Upconversion luminescence of transparent Er^{3+}-doped chalcohalide glass-ceramics," *Opt. Mater.*, vol. 31, pp. 760–764, 2009.

[99] A. M. G. Pedrosa, J. E. C. Silva, P. M. Pimentel, D. M. A. Melo and F. R. G. Silva, "Synthesis and optical investigation of systems involving mixed Ce and Er oxides," *J. Alloys Comp.*, vol. 374, pp. 223–225, 2004.

[100] A. Patra, C. S. Friend, R. Kapoor and P. N. Prasad, "Fluorescence upconversion properties of Er^{+3} doped TiO_2 and $BaTiO_3$ nanocrystals," *Chem. Mater.*, vol. 15, no. 19, pp. 3650-3655, 2003.

[101] G. F. Ansari, S. K. Mahajan and J. Parashar, "Intense Upconversion Luminescence of Yb^{3+}-Er^{3+} in Li_2O Content Tungsten-tellurite Glasses", *J. Fluoresc.*, vol. 21, pp. 1337–1342, 2011.

[102] J. H. Cho, M. Bass, S. Babu, J. M. Dowding, W. T. Self and S. Seal, "Up conversion luminescence of Yb^{+3}–Er^{+3} codoped CeO_2 nanocrystals with imaging applications," *J. Luminescence*, vol. 132, pp. 743–749, 2012.

[103] C. O. Chui, H. Kim, P. C. McIntyre and K. C. Saraswat, "Atomic layer deposition of high-k dielectric for germanium MOS applications—Substrate surface preparation," *IEEE Elect. Device Lett.*, vol. 25, no. 5, pp. 274– 276, 2004.

[104] E. P. Gusev and C. P. D Emic, "Charge detrapping in HfO_2 high-k gate dielectric stacks," *Appl. Phys. Lett.*, vol. 83, no. 25, pp. 5223–5225, 2003.